

---

LUMINOSITY DISTRIBUTIONS AND  
ABUNDANCE TOMOGRAPHY  
MODELLING OF TYPE IA SUPERNOVAE

---

**Christopher John Ashall**

A thesis submitted in partial fulfillment of the requirements  
of Liverpool John Moores University for the degree of  
Doctor of Philosophy

23<sup>rd</sup> January 2017

---

# Abstract

I present an investigation into Type Ia Supernovae (SNe Ia). The aim of this investigation is to explain the physics and diversity of SNe Ia, motivated by the fact that, although SNe Ia are known to come from a thermonuclear explosion of a C+O Chandrasekhar mass (Ch-mass) White Dwarf (WD), their exact explosion scenario is one of debate, and their full diversity is not fully understood. As SNe Ia are used as cosmological distance probes, understanding their explosions and progenitors systems in more detail could have important consequences.

To examine the diversity of SNe Ia, I first present a large sample analysis of their  $B$  and  $V$ - band light curves, separated by host galaxy type. A new method for calculating host galaxy extinction is implemented and the width luminosity relation (WLR) is examined. After correction for host galaxy extinction, ‘normal’ SNe Ia ( $\Delta m_{15}(B) < 1.6$  mag) fill a larger parameter space in the WLR than previously suggested. Even excluding fast declining SNe, ‘normal’ ( $M_B < -18$  mag) SNe Ia from Star forming (S-F) and passive galaxies are distinct. This may indicate that various progenitor channels are prevalent in different galaxy types. Furthermore, it was also confirmed that sub-luminous SNe Ia tend to favour passive galaxies, which implies that this subset of SNe Ia come from an older progenitor system. There was a lack of transition SNe Ia in the dataset used in this project. These are SNe Ia with a luminosity between normal and sub-luminous SNe Ia. Understanding transitional SNe Ia is important in determining

whether sub-luminous SNe Ia are a totally different population.

With the aim of understanding how normal SNe explode, I first turn my attention to SN 2014J. SN 2014J was the closest type Ia in the last 410 years, and it was a once in a life time opportunity to study. Therefore, a detailed spectroscopic and photometric analysis and abundance stratification modelling of SN 2014J is presented. SN 2014J is a spectroscopically normal type Ia SN with a  $B$  band decline rate of 0.95 mag, before correction for extinction. It was located in the dusty starburst galaxy M82, and does not follow the average Galactic extinction law of  $R_v = 3.1$ .

With the knowledge about the diversity of SNe Ia and the ability to carry out detailed modelling, SN 1986G was next chosen to be modelled. SN 1986G sits in an interesting area of parameter space in the WLR. It is located in the ‘gap’ between normal and sub-luminous SNe Ia. It has been theorised that sub-luminous SNe Ia come from a different progenitor system than standard SNe Ia. Therefore, understanding SN properties in this ‘gap’ is important for determining at which point SNe Ia properties begin to diverge from the normal scenario. A full abundance tomography modelling of SN 1986G was carried out. It was found that this SN is a low energy Chandrasekhar mass explosion. It had 70% of the energy of a standard W7 model. These findings raise the possibility that only SNe Ia with very large decline rates deviate from a Chandrasekhar mass.

*It's the little things that people do which makes the difference. My little thing is understanding the Universe. - C. Ashall 2016*

*There is no passion in playing small, in settling for a life that is less than the one you are capable of living. - C. Ashall 2016*

*I always wonder why birds stay in the same place when they can fly anywhere on the earth. Then I ask my self the same thing. - Harun Yahya*

# Acknowledgements

First of all I would like to thank my supervisor Paolo Mazzali, without his great guidance and help I would not have been able to complete this thesis. I would also like to thank my parents, without their help in life I would not be where I am today. They have always been supportive and helped me with my studies. I am also giving a big thank you to my girlfriend Sophia, she has helped me throughout the whole of my PhD, and she was a good listener I needed some one. Thank you to my second supervisor Phil James who has helped me with my work, and helped me improve my poor english. Finally I would like to thank all of my PhD friends who helped me get through this process. I thoroughly enjoyed all of our political and philosophical debates.

# List of Publications

Luminosity distributions of Type Ia supernovae, **Ashall, C.**; Mazzali, P.; Sasdelli, M.; Prentice, S. J., MNRAS, 460, 3529A - 08, 2016

Photometric and spectroscopic observations, and abundance tomography modelling of the Type Ia supernova SN 2014J located in M82, **Ashall, C.**; Mazzali, P.; Bersier, D.; Hachinger, S.; Phillips, M.; Percival, S.; James, P.; Maguire, K., MNRAS, 445, 4427A - 12, 2014

Abundance stratification in Type Ia supernovae - V. SN 1986G bridging the gap between normal and subluminous SNe Ia, **Ashall, C.**; Mazzali, P.; Pian, E.; James, P.; MNRAS, 463, 1891A, 2016

A very luminous magnetar-powered supernova associated with an ultra-long -ray burst, Greiner, Jochen; Mazzali, Paolo A.; Kann, D. Alexander; Krhler, Thomas; Pian, Elena; Prentice, Simon; Olivares E., Felipe; Rossi, Andrea; Klose, Sylvio; Taubenberger, Stefan; Knust, Fabian; Afonso, Paulo M. J.; **Ashall, Chris**; et al., Nature, 523, 189G 07, 2015- Contribution: Magnetar light curve modelling.

Breaking the colour-reddening degeneracy in Type Ia supernovae, Sasdelli, Michele; Ishida, E. E. O.; Hillebrandt, W.; **Ashall, C.**; Mazzali, P. A.; Prentice, S. J., MNRAS, 460, 373S-07, 2016 - Contribution: Advising on how to deal with photometry and providing data for k-corrections of SN 2011fe.

The Superluminous Transient ASASSN-15lh as a Tidal Disruption Event from a Kerr Black Hole, Leloudas, G.; Fraser, M.; Stone, N. C.; van Velzen, S.; Jonker, P. G.; Arcavi, I.; Fremling, C.; Maund, J. R.; Smartt, S. J.; Kruhler, T.; Miller-Jones, J. C. A.; Vreeswijk, P. M.; Gal-Yam, A.; Mazzali, P. A.; De Cia, A.; Howell, D. A.; Inserra, C.; Patat, F.; de Ugarte Postigo, A.; Yaron, O.; **Ashall, C.**; et al., arXiv:1609.02927, in press with Nature astronomy-Contribution: Providing data and taking observations.

Cartier, R.; Sullivan, M.; Firth, R.; Pignata, G.; Mazzali, P.; Maguire, K.; Childress, M. J.; Arcavi, I.; Ashall, C.; et al., Early observations of the nearby type Ia supernova SN 2015F, In press with MNRAS, 464, 4476V, 2017- Contribution: Providing data, taking observations and giving advice on the science of spectral formation.

SN 2009ip at late times - an interacting transient at +2 years, Fraser, Morgan; Kotak, Rubina; Pastorello, Andrea; Jerkstrand, Anders; Smartt, Stephen J.; Chen, Ting-Wan; Childress, Michael; Gilmore, Gerard; Inserra, Cosimo; Kankare, Erkki; Margheim, Steve; Mattila, Seppo; Valenti, Stefano; **Ashall, Christopher**; et al., MNRAS, 453, 3886F-11, 2015 -Contribution: Providing data and taking observations.

Supernova 2013fc in a circumnuclear ring of a luminous infrared galaxy: the big brother of SN 1998S, Kangas, T.; Mattila, S.; Kankare, E.; Lundqvist, P.; Visnen, P.; Childress, M.; Pignata, G.; McCully, C.; Valenti, S.; Vink, J.; Pastorello, A.; Elias-

Rosa, N.; Fraser, M.; Gal-Yam, A.; Kotak, R.; Kotilainen, J. K.; Smartt, S. J.; Galbany, L.; Harmanen, J.; Howell, D. A.; Inserra, C.; Marion, G. H.; Quimby, R. M.; Silverman, J. M.; Szalai, T.; Wheeler, J. C.; **Ashall, C.**; et al., MNRAS, 456, 323K- 02, 2016 -Contribution: Providing data and taking observations.

PESSTO: survey description and products from the first data release by the Public ESO Spectroscopic Survey of Transient Object, Smartt, S. J.; Valenti, S.; Fraser, M.; Inserra, C.; Young, D. R.; Sullivan, M.; Pastorello, A.; Benetti, S.; Gal-Yam, A.; Knapic, C.; Molinaro, M.; Smareglia, R.; Smith, K. W.; Taubenberger, S.; Yaron, O.; Anderson, J. P.; **Ashall, C.**; et al., , MNRAS, 579, 40S- 07, 2015 -Contribution: Providing comments on science.

# Contents

<b>Abstract</b>	<b>1</b>
<b>Acknowledgements</b>	<b>4</b>
<b>List of Publications</b>	<b>5</b>
<b>1 Introduction</b>	<b>23</b>
1.1 SN classification . . . . .	24
1.2 SN Ia light curves . . . . .	27
1.3 SN Ia progenitors . . . . .	29
1.3.1 Single Degenerate scenario . . . . .	31
1.3.2 Double Degenerate (DD) scenario . . . . .	34
1.3.3 Triple system collision . . . . .	34
1.4 Nucleosynthesis . . . . .	35
1.5 SN Ia by host type . . . . .	36
1.6 SN Ia by sub types . . . . .	38
1.7 SN Ia spectra . . . . .	39
1.7.1 Photospheric phase . . . . .	39
1.7.2 Nebular phase . . . . .	41
1.8 SN Ia UV data . . . . .	43

<i>CONTENTS</i>	9
1.9 Outline of thesis . . . . .	44
<b>2 Luminosity Distributions of SNe Ia</b>	<b>45</b>
2.1 Preface . . . . .	45
2.2 Previous studies . . . . .	46
2.3 Data & Method . . . . .	48
2.4 Quality of LC spline fit . . . . .	54
2.5 Luminosity Distribution . . . . .	56
2.5.1 <i>B</i> and <i>V</i> luminosity distributions . . . . .	56
2.5.2 Width Luminosity Relation . . . . .	59
2.6 Correction for host galaxy extinction . . . . .	62
2.6.1 Luminosity Distribution . . . . .	65
2.6.2 Host galaxy extinction . . . . .	65
2.6.3 LD by host galaxy type . . . . .	68
2.6.4 WLR after extinction correction . . . . .	70
2.7 Full luminosity distribution . . . . .	72
2.8 SNe Ia from young and old stellar populations . . . . .	76
2.9 Discussion . . . . .	80
2.9.1 Errors and significance of results. . . . .	85
2.10 Conclusions . . . . .	86
<b>3 Radiative transfer</b>	<b>89</b>
3.1 Preface . . . . .	89
3.2 Radiative Transfer Theory . . . . .	89
3.3 Radiative Transfer in SN ejecta . . . . .	92
3.4 MC code . . . . .	93
3.5 Ionization and excitation . . . . .	96

<i>CONTENTS</i>	10
3.6 Numerical technique . . . . .	97
3.6.1 Photon branching . . . . .	98
3.6.2 Random walk . . . . .	99
3.7 Modelling procedure . . . . .	102
3.7.1 Constraining the abundances . . . . .	102
<b>4 SN 2014J</b>	<b>104</b>
4.1 Preface . . . . .	104
4.2 SN 2014J . . . . .	104
4.3 Observations . . . . .	105
4.4 Extinction . . . . .	106
4.5 Photometry . . . . .	109
4.6 Spectroscopy . . . . .	113
4.7 Models . . . . .	117
4.7.1 Day -8 . . . . .	118
4.7.2 Day -7 . . . . .	121
4.7.3 Day+0 . . . . .	121
4.7.4 Day+1 . . . . .	122
4.7.5 Day +2 . . . . .	122
4.7.6 Day +3 . . . . .	123
4.7.7 Day +4 . . . . .	123
4.7.8 Day +6 . . . . .	125
4.7.9 Day +8 . . . . .	125
4.7.10 Day +10 . . . . .	126
4.8 Abundance stratification . . . . .	126
4.9 Work carried out after this . . . . .	128
4.10 Summary . . . . .	129

<i>CONTENTS</i>	11
<b>5 SN 1986G</b>	<b>131</b>
5.1 Preface . . . . .	131
5.2 SN 1986G . . . . .	132
5.3 Data . . . . .	135
5.4 Flux Calibration of spectra . . . . .	137
5.5 Modelling Techniques . . . . .	139
5.5.1 Photospheric phase modelling technique . . . . .	139
5.5.2 Nebular Phase modelling technique . . . . .	140
5.5.3 Light curve code . . . . .	140
5.6 Photospheric models . . . . .	142
5.6.1 Extinction and distance . . . . .	142
5.6.2 Density profiles . . . . .	143
5.6.3 Photospheric models . . . . .	143
5.6.4 -3 days . . . . .	144
5.6.5 -2 days . . . . .	144
5.6.6 -1 days . . . . .	147
5.6.7 +0 days . . . . .	147
5.6.8 +1 days . . . . .	148
5.6.9 +2days . . . . .	148
5.7 Nebular phase models . . . . .	149
5.8 Abundance tomography . . . . .	152
5.9 A consistent, reduced-energy model . . . . .	157
5.9.1 Energy estimates . . . . .	157
5.9.2 Photospheric-epoch models . . . . .	159
5.9.3 Carbon . . . . .	159
5.9.4 Nebular-epoch model . . . . .	163

<i>CONTENTS</i>	12
5.9.5 Abundance stratification . . . . .	163
5.10 Bolometric Light curves . . . . .	164
5.10.1 Observed light curve . . . . .	164
5.10.2 Synthetic light curve . . . . .	167
5.11 Conclusions . . . . .	169
<b>6 Conclusions</b>	<b>172</b>
6.1 Futurework . . . . .	174
<b>Appendix</b>	<b>176</b>

# List of Figures

1.1	Magnitude phase diagram of transient objects (Kasliwal , 2015). . . .	24
1.2	The SN classification scheme (Turatto, 2003). . . . .	25
1.3	Sketches of SN spectra at maximum light (Carroll & Ostlie, 2007). . .	26
1.4	The width luminsity relation first published in Phillips (1993). . . . .	30
1.5	Abundance distribution of the W7 explosion model in velocity and mass space (Iwamoto et al., 1999). . . . .	37
1.6	A plot showing how P-Cygni profiles are formed in SNe Ia (Kasen, 2016). . . . .	40
1.7	Diversity of maximum light spectra of SNe Ia. The spectra are plotted from top to bottom in terms of light curve shape. It should be noted that the spectrum of SN 2004eo was taken at +2 days compared to <i>B</i> band maximum. Therefore it appears less luminous in the above plot.	42
1.8	A nebular spectrum and model of SN 2011fe (Mazzali et al., 2015). . .	43
2.1	Redshift distribution of the SNe Ia used in this work. The bin sizes are $z=0.002$ . . . . .	49

2.2	An example of the fitting procedure, the $B$ -band light curve of SN 2000dn. The red points are the photometry and the shaded area is the 1000 LCs derived from these photometry points, as explained in section 2.1. . . . .	54
2.3	The $B$ band residuals between the SN photometry and LC spline fit, as a function of time. Data from 46 randomly selected SNe are used. . .	55
2.4	The $V$ band residuals between the SN photometry and LC spline fit, as a function of time. Data from 46 randomly selected SNe are used. . .	55
2.5	The luminosity distributions and $\Delta m_{15}$ distributions of the SN sample before correction for reddening. <i>Top:</i> The left plot is a distribution of $B$ -band absolute magnitude, and the right plot is the distribution of $\Delta m_{15}(B)$ . <i>Bottom:</i> The left plot is a distribution of $V$ -band absolute magnitude, and the right plot is the distribution of $\Delta m_{15}(V)$ . In these plots the SNe have not been corrected for host galaxy extinction. The stars in two right hand panels are the Gaussians calculated from the GMM tests. . . . .	57
2.6	The $B$ -band WLR before reddening correction. The black points are SNe from S-F galaxies, the blue points are SNe from E galaxies, and the red points are SNe Ia from S0 galaxies. The yellow line is the WLR given in Phillips et al. (1999), and the red line is the relation given for the subluminous tail from Taubenberger et al. (2008). . . . .	60
2.7	<i>Top:</i> The WLR before reddening correction including only SNe with $(B - V)_{Bmax} < 0.01$ . The blue line of best fit is a second order polynomial. The yellow model is the line of best fit from Phillips et al. (1999). <i>Bottom:</i> The residuals of the WLR above as a function of $\Delta m_{15}(B)$ . . . . .	61

- 2.8 *Top:* Left: The  $M_B$  LD of the SN Ia from S-F galaxies, before and after correction for extinction. Right: compares the values of  $M_B$ , again before and after correction for extinction, for SNe from S-F galaxies. *Bottom:* Left: The  $M_B$  LD of the SNe Ia from passive galaxies, before and after correction for extinction. Right:  $M_B$ , before and after correction for extinction, for SNe from passive galaxies. . . . . 66
- 2.9 *Top:*  $B$ -band luminosity distribution, corrected for host galaxy extinction. The bin sizes are 0.15 and 0.1 mag for the  $M_B$  and  $\Delta m_{15}(B)$  plots respectively. *Bottom:*  $V$ -band luminosity distribution, corrected for host galaxy extinction. The bin sizes are 0.15 and 0.1 mag for the  $M_V$  and  $\Delta m_{15}(V)$  plots respectively. The stars in the right hand panel are the Gaussians calculated from the GMM tests. . . . . 67
- 2.10 SNe Ia separated by host galaxy type, after correction for host galaxy extinction. Blue shows SNe Ia from S-F galaxies and green is SNe Ia from passive galaxies. . . . . 69
- 2.11  $M_B$  vs  $M_V$  for all SNe Ia in the sample. . . . . 70
- 2.12 The cumulative probability distributions for the samples used in the K-S test. The green solid lines are SNe from passive galaxies, and the blue dashed from SNe from S-F galaxies. . . . . 71
- 2.13 The WLR corrected for host galaxy extinction. The black points are SNe from S-F galaxies, the blue are points are SNe from elliptical galaxies and the red points are SNe Ia from S0 galaxies. The green point is SN2003cg. *Top:*  $B$ -band *Bottom:*  $V$ -band . . . . . 74

2.14 The final  $M_B$  and  $M_V$  luminosity distribution plots for the sample used in this work. SNe Ia from passive galaxies with no known extinction have been re-added to this distribution to increase the sample size. *Top:* The left plot is the full  $M_B$  luminosity distribution, the right plot is the full  $M_V$  luminosity distribution. The overlaid blue histograms are the distributions of SNe from passive galaxies. *Bottom:* The left plot is the full  $M_B$  luminosity distribution separated by host galaxy type, and the right plot is the full  $M_V$  distribution separated by host galaxy type. . . . . 77

2.15 The final  $\Delta m_{15}(B)$  and  $\Delta m_{15}(V)$  LD plots for the sample used in this work. SNe Ia from passive galaxies with no known extinction have been re-added to this distribution to increase the sample size. *Top:* The left plot is the full  $\Delta m_{15}(B)$  LD, the right plot is the full  $\Delta m_{15}(V)$  LD. The overlaid blue histograms are the distributions of SNe from passive galaxies. *Bottom:* The left plot is the full  $\Delta m_{15}(B)$  LD separated by host galaxy type, and the right plot is the full  $\Delta m_{15}(V)$  distribution separated by host galaxy type. . . . . 78

2.16 The  $B$ -band LD for SNe Ia from passive galaxies normalized, scaled and subtracted from the LD of SNe Ia from S-F galaxies. The factor by which the LD from passive galaxies has been normalized is presented on the top of each plot. The blue bars in the bottom right panel are the LD of SNe Ia from passive galaxies scaled to 15% of those from active galaxies. . . . . 81

2.17	The $V$ -band LD for SNe Ia from passive galaxies normalized, scaled and subtracted from the LD of SNe Ia from S-F galaxies. The factor by which the LD from passive galaxies has been normalized is presented on the top of each plot. The blue bars in the bottom right panel are the LD of SNe Ia from passive galaxies scaled to 15% of those from active galaxies. . . . .	82
3.1	Photon packets encounter line events or electron scattering during their random walk within each shell (Mazzali, 2000). . . . .	101
4.1	Maximum light spectra of 2014J and SN 2011fe. . . . .	108
4.2	Aperture photometry light curves, produced using LT data. SDSS $g'r'i'$ light curves are presented. The errors on the photometry appear to be constant; this is due to the catalogue error on the zero point star dominating. . . . .	110
4.3	SIFTO SN 2014J light curve fits . . . . .	111
4.4	Dependence of $\Delta m(B)_{15}$ on $E(B - V)$ for different values of $R_V$ , using SN 2011fe spectrophotometry and the Hsiao template. . . . .	112
4.5	All spectral observations of SN 2014J, LT and INT. The time is given relative to rest-frame $B$ -band maximum. The spectra have not been corrected for reddening. There were no data collected between 5700-5800 Å for the LT observations and the two atmospheric absorption lines have been removed. All of the plots have been offset by an arbitrary amount for the purpose of presentation. . . . .	115
4.6	A check of the flux calibration process of Feige34 back on to itself. The blue points are the catalogue data, and the red the data from the observations. . . . .	116

4.7	An overview of the features of SN 2014J. This spectrum has been dereddened and was taken at B-band maximum. . . . .	116
4.8	Modelled (blue) and observed spectra (green) of SN 2014J. Plot (a) is from -4d, (b) is from -3d, (c) is +0d maximum, (d) is +1d and (e) is +2d. All of the dates are relative to B-band maximum. All spectra have been dereddened. The red spectrum at +1 d is from the INT. . . . .	119
4.9	Modelled (blue) and observed spectra (green) of SN 2014J. Plot (a) is from +3d, (b) is from +4d, (c) is +5d, (d) is +6d and (e) is +8d. All of the dates are relative to B-band maximum. All spectra have been dereddened. The red spectrum of +4 d is from the INT. . . . .	124
4.10	The abundance distribution of SN 2014J. The Ni/Co/Fe abundances are given in terms of mass fractions of $^{56}\text{Ni}$ ( $^{56}\text{Ni}_0$ ) and stable Fe ( $\text{Fe}_0$ ) at $t = 0$ . In the spectral models no stable Ni or Co and no radioactive Fe are assumed to be present. . . . .	128
5.1	The $B$ band absolute magnitude of four SNe Ia which have a variety of LC shapes. . . . .	135
5.2	The spectra of four SNe Ia at $B$ band maximum. The SNe correspond to the 4 SNe in Figure 5.1 . . . . .	136
5.3	SN 1986G spectrum from 11th May. The back spectrum is the original and the red is the spectrum after flux calibration.. The stars are the center of the $B$ and $V$ bands. . . . .	139
5.4	One-zone models of SN 1986G at $B$ band maximum, using a variety of distance modulus and extinction values. The observed spectra are in black and the modelled in blue. . . . .	141

5.5	The photospheric phase models of SN 1986G, where the spectra have been shifted in flux by a constant for clarity. Models for both the W7 (blue solid) and Sub-Ch (red dashed) density profiles are shown. The spectra have been corrected for extinction. . . . .	145
5.6	The nebular phase models of SN 1986G. The blue spectrum was obtained using a W7 density profile and the green spectrum using the Sub-Ch profile. The black line is the observed spectrum. The spectra have been corrected for extinction. . . . .	152
5.7	The abundance distribution of SN 1986G obtained with the W7 density profile. . . . .	155
5.8	The abundance distribution of SN 1986G obtained with the Sub-Ch density profile. . . . .	156
5.9	The W7, Sub-Ch and W7e0.7 density profiles as a function of velocity at $t=100$ s after explosion. The vertical grey lines show the range in values $v_{ph}$ can take, for the -3 d to +2 d models. . . . .	158
5.10	One-zone models at -3 days relative to $B$ band maximum. The synthetic spectra were produced using the W7 (blue), W7e0.7 (green) and Sub-Ch (red dashed) density profiles. The spectra have been corrected for extinction. . . . .	160
5.11	The photospheric phase models of SN 1986G, calculated using the W7e0.7 density profile. The blue line are the models and the black line the observed spectra. The spectra have been corrected for extinction.	161
5.12	Synthetic spectrum at -3 days produced using the W7e0.7 density profile to constrain an upper limit on carbon. The blue line is the model with 0% of C, the red dashed line with the 2% C and the green line with 10% C at the photosphere. The black line is the observed spectra.	162

5.13 The nebular phase models of SN 1986G. The green line is the model calculated using the W7e0.7 density profile. The spectra have been corrected for extinction. . . . . 162

5.14 The abundance distribution of the ejecta of SN 1986G obtained using the W7e0.7 density profile. . . . . 165

5.15 The observed (blue dots) bolometric light curve with the upper (cyan markers) and lower (red markers) limits. As well as the modelled LC using the derived abundance distribution from the W7 (green), Sub-Ch (red) and W7e0.7 (purple) density profiles. . . . . 170

# List of Tables

2.1	Sources of the data. . . . .	49
2.2	The reference of the 11 SNe Ia mentioned in Table 2.1. . . . .	50
2.3	Statistics of the data, not corrected for host galaxy extinction has been applied. . . . .	51
2.4	Statistics of data before correction for host galaxy extinction. The data used in this table are a subset of the full sample. . . . .	72
2.5	Statistics of the data after correction for host galaxy extinction. . . . .	73
2.6	K-S tests for SNe with different types of host galaxies, after correction for host galaxy extinction. . . . .	73
2.7	Statistics of full LD. . . . .	75
4.1	Log of spectroscopic observations of SN 2014J. . . . .	107
4.2	Log of the Si 6355Å absorption line velocities. The resolution of the spectra is $\sim 9\text{\AA}$ , this value has been used to calculate the error on the velocity of the Si II line. . . . .	114
4.3	Input parameters and calculated converged temperature. . . . .	118
5.1	The $\Delta M_{15}(B)$ and absolute $B$ band magnitude of the SNe Ia used in Figures 5.1 and 5.2. . . . .	135
5.2	The spectra of SN 1986G. . . . .	137

5.3	The $B$ and $V$ sythetic photometry ( $m_{spec}$ ) taken form the spectra, and real photometry ( $m_{B_{phot}}$ ) obtained from Phillips et al. (1987). . . . .	138
5.4	Synthetic photometry from the new spectra. . . . .	139
5.5	Published distances to SN 1986G. . . . .	143
5.6	Input parameters and calculated converged black body temperatures for models from the W7 and Sub-Ch density profiles. . . . .	146
5.7	Integrated abundances from the full abundance tomography modelling of SN 1986G. The errors on the masses are $\pm 25\%$ , except for $^{56}\text{Ni}$ which has an error of $\pm 10\%$ . . . . .	155
5.8	Integrated abundances for the W7e0.7 models. The errors on the masses are $\pm 25\%$ , except for $^{56}\text{Ni}$ which has an error of $\pm 10\%$ . . . . .	164
6.1	The SNe used in the luminsity distribution study. The values have been corrected for MW extinction but not host galaxy extinction. . . . .	177
6.2	The photometry of SN 2014J. The errors on the magnitudes do not include the error on the standard star. . . . .	187

# 1. Introduction

Transient objects are important astrophysical events. They can be parameterised by their maximum brightness and their time to peak (Kasliwal , 2015). This can be seen in Figure 1.1, which is a phase diagram of transient objects in the Universe. Recently more and more of this phase diagram has been explored, as recent surveys have higher cadences and can probe to fainter magnitudes (e.g., Rau et al., 2009). Surprisingly there have been objects discovered in almost all parts of it (e.g., Kasliwal et al., 2012). Supernovae are a much studied class of transient event, as they are bright and have a long enough rise time to be discovered by targeted surveys (Leaman et al., 2011). They are the main producers of heavy elements in the Universe (Iwamoto et al., 1999). Type Ia supernovae (SNe Ia) are of particular interest as they produce most of the iron group elements (Iwamoto et al., 1999). They are also the best standardizable candles in the cosmos, and were used in the discovery of the acceleration of the Universe (Riess et al., 1998; Perlmutter et al., 1999). However, the exact nature of these events is unknown. Understanding the progenitor scenario and explosion mechanism of SNe Ia is of great importance if one wants to improve their use as standardizable candles.

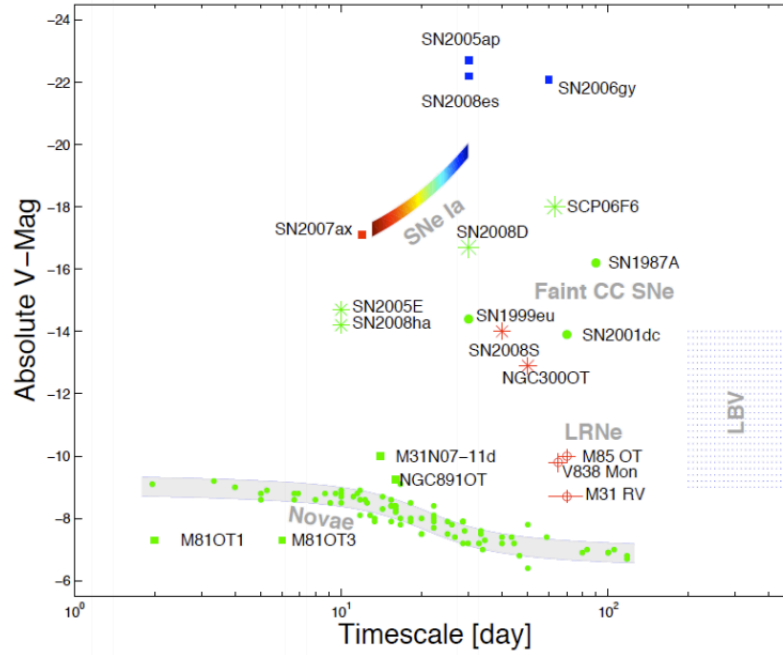


Figure 1.1: Magnitude phase diagram of transient objects (Kasliwal , 2015).

## 1.1 SN classification

Supernovae are extremely energetic explosions, which typically have a kinetic energy (K.E.) of  $\sim 10^{51}$  *erg*, and they are either thermonuclear or core collapse. Supernovae are classified by spectral type and photometric properties, more specifically early time spectra. Therefore SN are classified on the chemical and physical properties of the outermost layers of the exploding star. For a full review see Filippenko (1997). It was first theorised that there were two types of SN, Type I and Type II. This was based on their optical spectra, where type I SNe are defined by a lack of hydrogen. Type Ia SNe were found to be a subset of Type I SNe. Type Ia SNe have a deep absorption trough around  $6150 \text{ \AA}$ , which can be attributed to the Si II  $6355 \text{ \AA}$  line. The remaining type I SNe are divided into two subclasses, type Ib and Ic. They differ with respect to the presence of He I lines, with Ib SNe having He I features. In reality the subclassification is more complicated than this, but for this work it is adequate to know that SNe Ia are

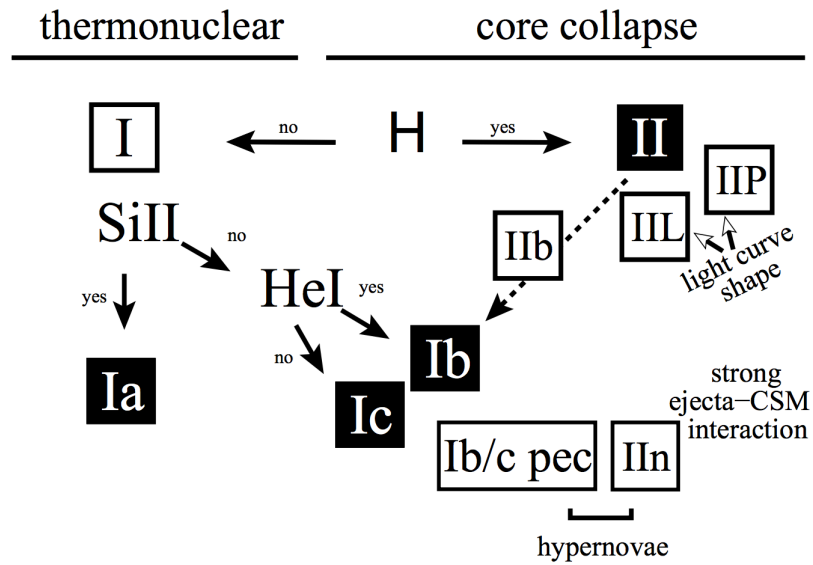


Figure 1.2: The SN classification scheme (Turatto, 2003).

intrinsically different from all other types of SN.

Type II SNe are characterised by the presence of H in their spectra. They avoid early type galaxies and are associated with the core collapse of massive stars. There are typically four subclasses of type II SNe, IIP, IIL, IIn and Iib. IIP SNe stop declining shortly after optical maximum and show a plateau of 2-3 months, whereas IIL SNe show a steep linear decline in their light curves after maximum light. SNe IIn have a slow evolution and are dominated by strong Balmer emission lines. Type Iib SNe are observationally a mixture of type Ib and II SNe, in the sense that they have hydrogen lines at early times but show signs of Type Ib in their late-time spectra, in the form of helium lines. Fig 1.2 visually represents the classification scheme of SNe, and Figure 1.3 presents an example of the different subtypes at maximum light. Turatto (2003) present a more detailed explanation of this classification scheme.

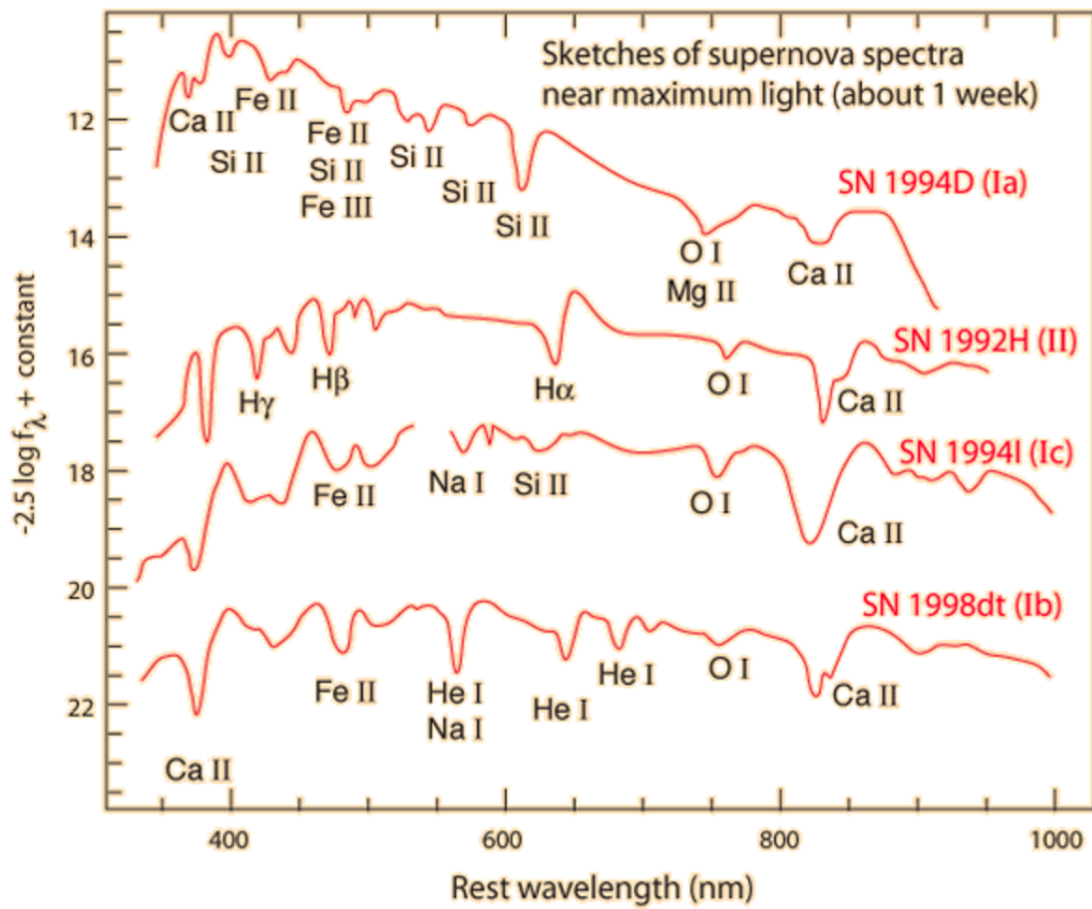


Figure 1.3: Sketches of SN spectra at maximum light (Carroll & Ostlie, 2007).

## 1.2 SN Ia light curves

SN are often analysed using multi-band photometry. These photometry points are known as light curves (LC), and it is these LCs which show the evolution of a SN as a function of time. To first order all SNe Ia can be parameterised by their power source, which is the amount of  $^{56}\text{Ni}$  in the ejecta (Arnett, 1982).  $^{56}\text{Ni}$  is the main product of burning to nuclear statistical equilibrium (NSE) during the explosion (Colgate & McKee, 1969).  $^{56}\text{Ni}$  is a radioactive isotope which follows the decay chain,



The  $^{56}\text{Ni}$  decay produces  $\gamma$ -rays due to its decays to  $^{56}\text{Co}$  caused by electron capture. The  $^{56}\text{Co}$  decays to stable  $^{56}\text{Fe}$  through electron capture (81%) or  $\beta$ -decay (19%). The positrons from the  $\beta$ -decay deposit their K.E. in the ejecta and then annihilate with electrons producing two photons of energy  $E_\gamma = m_e c^2$ , which are therefore  $\gamma$ -rays. The  $\gamma$ -rays from both forms of decay are thermalised and escape the ejecta as optical or IR photons (Mazzali, 2000).

A SN Ia LC can be broken down into three sections: the rise to maximum light, maximum light and post maximum light. At very early times the ejecta of the SN is optically thick, therefore photons which are produced from the decay chain are trapped and cannot escape immediately. As the ejecta becomes more transparent more photons can be released and the LC rises. Arnett's law states that the maximum of the LC is reached when the released energy from the ejecta is balanced by the energy input from the decay (Arnett, 1982). The time it takes for a SN Ia to reach maximum light is usually between 15-21 days (Ganeshalingam et al., 2011). After maximum light the envelope of the SN is dilute enough for the trapped photons to stream outwards, and the energy input from the decay chain decreases due to the ongoing decay. The trapped photons continue to escape after maximum light, with the emitted energy being larger than the input energy. This occurs after  $\sim 50$  days past maximum light. After this the

light curve drops back level with the heating-cooling equilibrium, this is when the LC is on the  $^{56}\text{Co}$  decay (Mazzali, 2000).

SNe Ia LCs can be summarised by two parameters, their absolute magnitude and their stretch or decline rate,  $\Delta m_{15}(B)$ .  $\Delta m_{15}(B)$  is the difference in the  $B$ -band magnitude of the SN between maximum light and +15 days relative to maximum (Phillips, 1993; Phillips et al., 1999; Conley et al., 2008). This width-luminosity relationship (WLR) was first found by Phillips (1993), see Figure 1.4. It is this relation that means SNe Ia were found to be standardizable, and therefore good cosmological distance indicators.

The variation in the maximum luminosity of a SNe Ia is, to first order, caused by variation in the amount of  $^{56}\text{Ni}$  in the ejecta, and for a SNe Ia this can vary from  $\sim 0.1M_{\odot}$  to  $\sim 1.2M_{\odot}$  (Mazzali et al., 2007). As Arnett's law states, the brightness of a SN Ia is proportional to the mass of synthesised  $^{56}\text{Ni}$ , and the peak luminosity can be approximated by

$$\frac{M(^{56}\text{Ni})}{M_{\odot}} = L \times 10^{43} \times (6.45 \times e^{\frac{t_p}{8.8}} \times e^{-\frac{t_p}{111.3}})^{-1} \quad (1.1)$$

(Stritzinger & Leibundgut, 2005), where  $L$  is the bolometric luminosity at maximum and  $t_p$  is the rise time of the SNe Ia. Theoretically the width of a SN Ia LC,  $\tau$ , depends on kinetic energy of the explosion,  $E_K$  (or K.E) (Mazzali et al., 2007). Most SNe Ia are thought to come from a system close to the Chandrasekhar mass therefore a range of masses is probably not the cause in the variation of SNe Ia peak luminosity<sup>1</sup> (Nomoto, 1982). That leaves the  $E_K$  and  $\kappa$ . However,  $E_K$  is produced in almost equal amounts by burning a given mass to nuclear statistical equilibrium (NSE), or by incomplete burning to intermediate mass elements (IMEs) (Mazzali et al., 2001); given

---

<sup>1</sup> It is thought that some SNe Ia may deviate from the Chandrasekhar mass, but this is probably only at the extremes of the WLR

that NSE and IME make up to  $1.3M_{\odot}$  of the ejecta. The  $E_K$  of the ejecta can be given by,

$$E_K = [1.56M(^{56}\text{Ni}) + 1.74M(\text{stableNSE}) + 1.24M(\text{IME}) - \text{BE}] \times 10^{51} \text{erg} \quad (1.2)$$

(Woosley et al., 2007), where BE is the binding energy of the White Dwarf (WD). Therefore if the  $E_K$  and  $M_{ej}$  do not play the main role in the variation in LC shape, then opacity must be the dominant factor.

SNe Ia are dominated by line opacity not continuum opacity. The photons in the SNe Ia ejecta must first propagate through optically thick SN ejecta, through a random walk process; in this region they will interact with spectral lines and free electrons until they are redshifted (due to the expansion of the ejecta, relative to the rest frequency of the photon) into a region of the spectrum where the opacity is low. SNe Ia opacity is dominated by line opacity of low-ionization species, in particular low-excitation ions of Fe-group elements (Mazzali et al., 2001). These Fe-group elements have many more lines than the corresponding IMEs (by about a factor of 10). Therefore the average opacity is higher in regions where Fe-groups elements dominate, and hence SNe with a higher  $\text{Ni}^{56}/\text{IME}$  ratio have broader LCs (Mazzali et al., 2001). This can be summarised by

$$\tau \propto M(\text{NSE}) + 0.1(M(\text{IME})). \quad (1.3)$$

### 1.3 SN Ia progenitors

It is currently accepted that SNe Ia are produced from a carbon/oxygen White Dwarf (WD) in a binary system (e.g., Maoz et al., 2014). The three currently favoured pro-

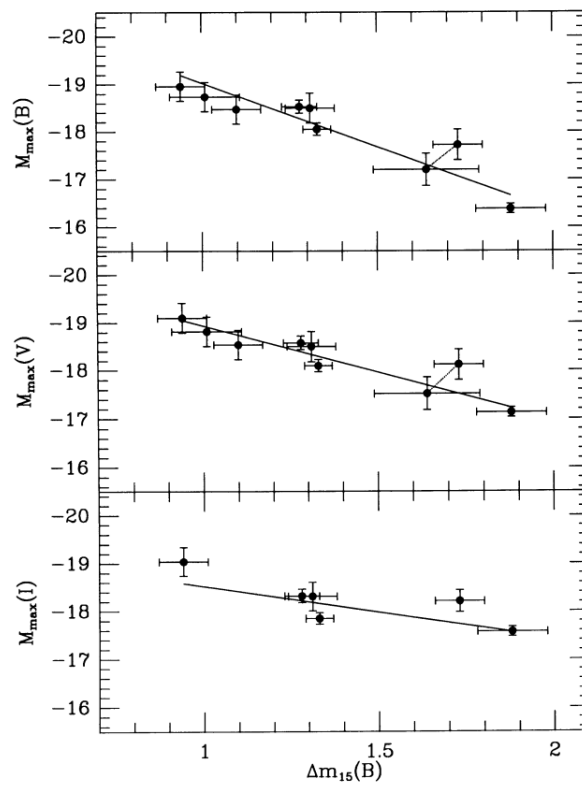


Figure 1.4: The width luminosity relation first published in Phillips (1993).

genitor scenarios are single degenerate (SD), double degenerate (DD) and collisions of C+O WDs in a triple system.

### 1.3.1 Single Degenerate scenario

In the SD scenario a C+O WD accretes material from a non-electron-degenerate companion star (Nomoto et al., 1997). This can be through H accretion or He accretion. Once the accretor reaches the Chandrasekhar mass (Ch-mass) thermonuclear runaway can occur and a SNe Ia is produced. It should be noted that a thermonuclear runaway reaction can occur on the surface of the WD well before the Chandrasekhar mass .

#### SD H accretion

Single Degenerate H accretion: This scenario can consist of two stars with a zero age main sequence (ZAMS) masses of  $> 3.5M_{\odot}$  and  $< 3.5M_{\odot}$ . The more massive star reaches the red giant phase and a common envelope (CE) phase occurs. After the common envelope phase the primary star burns its He and becomes a C+O WD. The secondary star then donates H rich material to WD, and the Chandrasekhar mass can be reached if the accretion is efficient (Ruiter et al., 2009, 2010). This is the ‘standard’ SD scenario.

#### SD explosions

After the WD reaches the Chandrasekhar mass the exact composition and central density of it is crucial in the outcome of the explosion. In terms of the explosion it has been theorised that the flame front can propagate either supersonically (detonation) or subsonically (deflagration) (Nomoto et al., 1984). However, pure detonations of Chandrasekhar mass WDs burn at high efficiency, and produce almost only iron-group elements (Arnett et al., 1971), whereas pure deflagrations have a lower kinetic energy

and a mixed abundance distribution which consists of a large amount of partially burnt and unburnt material (Röpke et al., 2007).

Therefore, it has been theorised that SNe Ia come from a delayed detonation scenario (Blinnikov & Khokhlov, 1986, 1987). This is one where the burning starts as a deflagration and at a certain density it transitions to a detonation. This is known as a deflagration-detonation-transition (DDT). The DDT happens after the star has expanded due to the deflagration phase. This causes the detonation to run through less dense material, which in turn makes more IMEs. Therefore the delayed detonation models produce a larger K.E. and less mixing, which is in line with observations (Stehle et al., 2005; Mazzali et al., 2007).

The delayed detonation model has been shown to produce the range and diversity that SNe Ia have. One unknown factor in this scenario is the density at which the DDT occurs, and the reason for this transition (Schmidt et al., 2010). It is usually set depending on the physical conditions of the flame front. It has been demonstrated that by changing the DDT the whole diversity of SNe Ia can be produced, including 1999by, a subluminous SNe Ia (Höflich et al., 2002). Some secondary parameters which can affect the explosion of the WD are variations in the initial carbon-to-oxygen profile in the progenitor, and the central density in the WD exploding as a SNe Ia. When the central density increases so does the binding energy, which translates to small expansion velocities (Höflich et al., 2002).

A fast deflagration explosion has also been shown to produce the observed properties of a normal SN Ia (Nomoto et al., 1984). The best example of this fast deflagration model is the W7 model. This model synthesises  $0.5\text{-}0.6 M_{\odot} {}^{56}\text{Ni}$ , and produces  $1.3 \times 10^{51} \text{ erg}$  of K.E. (Nomoto et al., 1984). The W7 model is favoured by radiative transfer modellers of SNe Ia (e.g., Ashall et al., 2014).

Another method which could pre-expand the star by a deflagration and then trans-

fer to a detonation is the pulsation scenario, although this is not currently popular. This explosion is one where the deflagration is so slow that the burning first quenches without making the transition to detonation (Hoefflich et al., 1995). This leaves the WD expanding but bound. The WD will then experience a strong pulsation. During the contraction of the WD, compression of the mixed layers of iron-peak and CO elements, which are formed at the dead deflagration front, give rise to a detonation. This model can explain why the transition does not happen at high densities (Hoefflich et al., 1995).

### **SD Sub-Chandrasekhar explosion**

The Sub-Chandrasekhar mass (sub-Ch) explosion of a C+O WD is also a viable progenitor scenario. WD masses in the scenario can range from 1-1.4  $M_{\odot}$ . One of the sub-Ch explosion scenarios is a C+O WD which accretes He from a He rich companion star. An edge-lit explosion on the WD can occur if a detonation is ignited in the He shell (Livne & Arnett, 1995). V445 Puppis is the only known example of a He-shell flash (Woudt et al., 2009). Other sub-Ch models are a carbon flash that triggers a core detonation and the double detonation model. The double detonation model is one where C+O WD accretes from a companion star and develops a helium-rich outer shell. If the helium shell becomes massive enough it can become unstable and detonate, and subsequently compression of the inward core by the propagating shocks may produce a secondary carbon detonation which explodes the WD (Woosley & Weaver, 1986; Fink et al., 2007).

Sim et al. (2010) demonstrated that sub-Ch explosions can produce a range of Ni masses from 0.3-0.8 $M_{\odot}$ , which is almost sufficient to cover the whole range of SNe Ia luminosities. Sub-Ch explosion models can produce enough IMEs to synthetically form a typical SNe Ia spectrum, without having to artificially transition a deflagration

to a detonation. The sub-Ch model has the advantage that it can provide a simple physical parameter (the mass of the explosion WD) which can account for the range and diversity of SNe Ia. The parameter also allows for a correlation between stellar population and brightness. However, in this model the  $M_{ej} \propto M_{Ni}$  therefore the SNe Ia do not follow the WLR, which is inconsistent with observations (e.g. Phillips et al., 1999).

### 1.3.2 Double Degenerate (DD) scenario

In the DD scenario two WDs violently merge after losing orbital angular momentum through the emission of gravitational waves (Iben & Tutukov, 1984). The DD scenario is favoured by some as it matches population synthesis studies (Ruiter et al., 2010). It also agrees with delay time studies (Maoz et al., 2010). Furthermore, it has been argued that a lack of hydrogen in the nebular phase spectra of SNe Ia favours a DD scenario, as swept-out hydrogen would be a sign of a non-degenerate companion star (Maguire et al., 2016).

It should be noted that non-violent mergers are thought not to lead to thermonuclear explosions, because these mergers would leave behind the more massive WD with a hot envelope, made up of material from the less massive WD. Fast accretion from the envelope would then turn the C+O WD into a O-Ne WD, which would collapse to a neutron star (Nomoto & Kondo, 1991).

### 1.3.3 Triple system collision

Finally, the collision scenario is the head-on collision of two C+O WDs in a triple system (Rosswog et al., 2009; Dong et al., 2015). When the two WDs collide they both detonate. The sum of both of the WDs should be larger than the Chandrasekhar mass. It has been hypothesised that these SNe Ia occur at such a rate to explain all of

the SNe Ia (Katz & Dong, 2012). Furthermore, double-peaked nebular lines could be an observational trait of this progenitor scenario. Dong et al. (2015) found that 3 out of 20 SNe Ia had these double peaks.

## 1.4 Nucleosynthesis

SNe Ia produce a large amount of metals. Nuclei up to the Fe group elements are synthesised by fusion of C and O and by capture of  $\alpha$ -particles. It has been theorised that  $\sim 55\%$  of the Fe-group elements in the Cosmos come from SNe Ia, with almost all of the rest of them coming from core collapse SNe (Iwamoto et al., 1999). A large amount of SNe Ia ejecta consist of IMEs and C/O. But when SN rates are taken into account core collapse SN contribute significantly more to IMEs and C/O abundances in the Universe (Iwamoto et al., 1999).

Depending on the peak temperature and peak density of the SNe Ia explosion there will be different stages of nucleosynthesis burning (Woosley et al., 1973). The burning stages are explained below from the most to least dense.

Nuclear statistical equilibrium is reached with a high peak density (above  $2 \times 10^8 \text{ g cm}^{-3}$ ) and a high peak temperature (more than  $5 \times 10^9 \text{ K}$ ). NSE is a rate equilibrium where there is a balance between the production rate and the respective destruction rate (by photodissociation). For SNe Ia this is dominated by Fe-group elements. At large densities, electron capture decreases the electron fraction, which leads to neutron-rich isotopes. Freeze out occurs when temperature and density decrease (some back and forth reactions stop being balanced). The result depends on which value falls low enough first, when the temperature is low enough normal freeze out occurs. This is where temperatures are too low to produce more  $\alpha$  particles, which are important for building up heavier elements (i.e. the temperatures are too low to pro-

duce  $\alpha$  particles by photodissociation). Conversely, for lower densities and a higher temperature ( $T > 5 \times 10^9$  K) the conditions are different in NSE.  $^{56}\text{Ni}$  is the dominant species produced, and neutron-rich nuclei are less common.  $\alpha$  particles remain in high abundance in this scenario.  $^{12}\text{C}$  and heavy nuclei are overabundant compared to a normal NSE composition, this is as triple  $\alpha$  processes occur at a larger rate.

Incomplete Si burning occurs if the peak temperature is between  $4.5$  and  $5 \times 10^9$  K. In incomplete Si burning, two clusters of elements form, one with  $28 < A < 45$  and the other  $A > 46$ . The result of this is roughly equal amounts of IMEs and Fe-group elements. As the peak temperature decreases so does the abundance of the Fe group elements. Iwamoto et al. (1999) state that the composition of the Fe group elements in this zone is strongly dependent on metallicity.

If the peak temperature is more than  $3.5 \times 10^9$  K and less than  $4.5 \times 10^9$  K explosive O burning occurs. This mostly makes IMEs (e.g. Si and S).

Figure 1.5 shows the abundance distribution in mass and velocity space for the standard W7 explosion model. This model produces the correct kinetic energy and abundances for a normal SNe Ia, and is therefore adopted as the standard explosion scenario. This model is a Chandrasekhar mass fast deflagration explosion. It has a kinetic energy of  $1.3 \times 10^{51}$  erg. It is the standard model to use as a density distribution for radiative transfer modelling of SNe Ia (Mazzali et al., 2014; Ashall et al., 2014, 2016).

## 1.5 SN Ia by host type

One way to separate SNe Ia is by host galaxy morphology. There have been many studies on SNe Ia differences depending on host galaxy type. It is known that faster declining and intrinsically dimmer SNe Ia are mostly found in passive galaxies (Hamuy et al.,

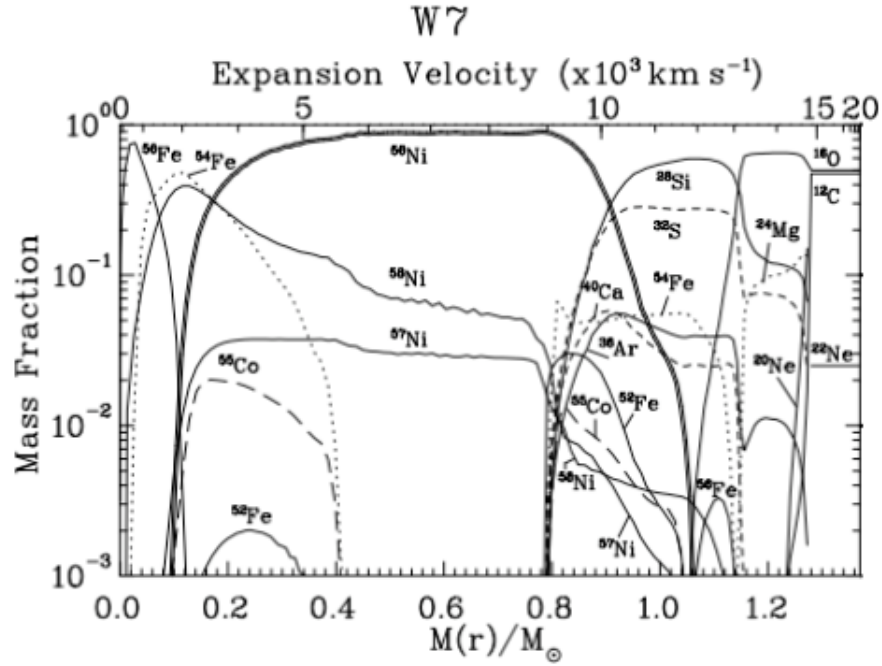


Figure 1.5: Abundance distribution of the W7 explosion model in velocity and mass space (Iwamoto et al., 1999).

1995, 1996). Peculiar sub-luminous 91bg-like SNe come from old stellar populations, at least 10 Gyr old (Howell, 2001). Host stellar mass was also found to correlate with SN luminosities; more massive galaxies tend to host SNe Ia which have lower stretch (i.e. a larger rate of decline) than SNe in lower-mass galaxies (Sullivan et al., 2010). It is possible that SNe Ia that occur in galaxies with different star formation, age and dust properties may have intrinsically different luminosities (Rigault et al., 2013; Childress et al., 2013). It has also been shown that SNe Ia with a higher Si II 6355Å line velocity tend to explode in more massive galaxies (Pan et al., 2015). This is not dissimilar from the result of Wang et al. (2013), who find that SNe Ia with high-velocity ejecta are more concentrated in inner, brighter regions of their host galaxy. Maguire et al. (2014) present a comparison of optical spectra with LC width information from PTF, an untargeted transient survey. They find that on average SNe Ia with a broader LC shape have a larger contribution from the high-velocity component relative to the

photospheric component in the Ca II NIR feature.

## 1.6 SN Ia by sub types

There are currently at least 6 subclasses of SNe Ia: ‘normal’, 91T-like, 02cx-like, 91bg-like, ‘Super-Chandrasekhar’ and SNe Ia-CSM.

SN 91T-like events, named after SN 1991T, are peculiar and overluminous. Spectroscopically they are characterised at early times by the weakness or absence of Ca II and Si II lines, and show very strong Si III lines. SN 1991T was  $\sim 0.6$  mag more luminous than normal SNe Ia (Saselli et al., 2014). It has been hypothesised that 91T-like events come from super-Chandrasekhar mass explosion mechanisms (Fisher et al., 1999; Mazzali et al., 1995), but Saselli et al. (2014) find that a Chandrasekhar mass explosion is more suited to SN 1991T.

SN 1991bg and SN 91bg-like events have low luminosity, rapidly declining light curves, low ejecta velocities and a cool spectrum which is dominated by IMEs, as well as particularly strong O I and Ti II lines. They are also unusually red and are underluminous by about  $\sim 2$  mag. The explosion mechanism of a 91bg-like SNe is a matter of debate, with options including DD explosions of WDs, sub-Chandrasekhar mass explosions triggered by detonation of the helium layer, or the collision of two WDs (Hillebrandt & Niemeyer, 2000; Höflich et al., 2002; Mazzali & Hachinger, 2012; Dong et al., 2015).

SN 2002cx like events exhibit hot, SN 1991T-like pre-maximum spectra, a low, 91bg-like luminosity, a LC which is broad for its luminosity, and low expansion velocities, roughly half of those of a normal SNe Ia (Li et al., 2003). These events are thought to come from the deflagration of a C+O WD, which only experiences partial burning that may (Sahu et al., 2008) or may not (Kromer et al., 2015) fully disrupt the

WD.

Super-Chandrasekhar SNe Ia are very luminous, which suggests a large  $^{56}\text{Ni}$  content and therefore a large ejected mass. They are thought to contain  $> 1.4M_{\odot}$  of ejecta, and probably come from a DD scenario (Howell et al., 2006; Yamanaka et al., 2009). However, they can also be explained by an ‘interacting scenario’, in which a SN Ia interacts with a H-/He-poor circumstellar medium (Hachinger et al., 2012).

Finally, SNe Ia-CSM show strong interaction with multiple thin H-rich CSM shells in the form of  $\text{H}\alpha$  emission and a black-body-like continuum (Hamuy et al., 2003; Deng et al., 2004; Dilday et al., 2012; Silverman et al., 2013), and are probably SD SNIa.

## 1.7 SN Ia spectra

### 1.7.1 Photospheric phase

The early time spectra of SNe Ia are dominated by P-Cygni like profiles (Filippenko, 1997), see Figure 1.6. This is because the core is optically thick at early times, due to line opacity of Fe-group elements (Mazzali, 2000). The radiation diffuses through the central core, which contains mostly  $^{56}\text{Ni}$ , reaches the outer layers and escapes. As the  $^{56}\text{Ni}$  is in the inner core, the outer layers can be assumed to be in radiative equilibrium. Therefore the outer layers just reprocess the flux coming from the inner layers (Mazzali, 2000). Hence, the outer layers leave P-Cygni like profiles (red emission + blue absorption) on a smooth underlying spectrum.

Although SNe Ia are standardizable candles their spectra can vary considerably as one looks down the WLR. Figure 1.7 demonstrates the diversity of SNe Ia spectra at maximum light. From top to bottom is a luminosity and temperature evolution (excluding SN 2002cx and SN 2003hv). As the luminosity decreases the Si II ratio

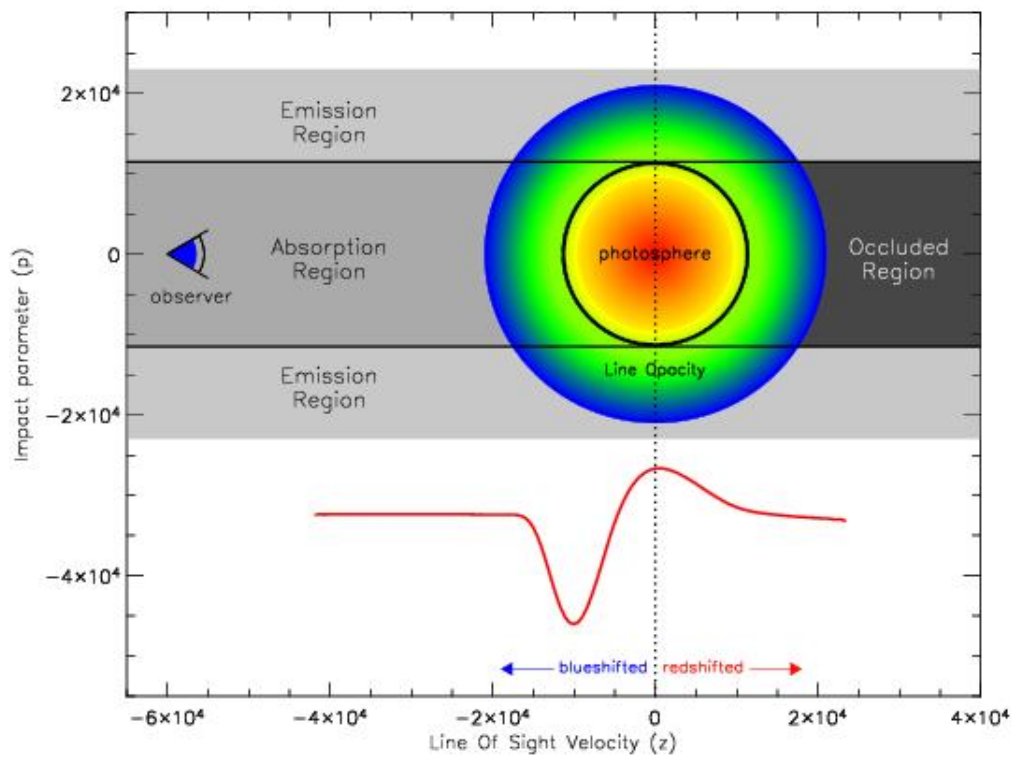


Figure 1.6: A plot showing how P-Cygni profiles are formed in SNe Ia (Kasen, 2016).

increases. This is due to the increase in recombination of Si III to Si II, which populates the blue of the Si II lines, as this line is at a higher excitation level (Hachinger et al., 2006). Furthermore, at the lowest luminosities the  $\sim 4500\text{\AA}$  Ti II feature begins to show. This feature is a good indication of a low luminosity SNe Ia (Ashall et al., 2016). Some SNe Ia have been seen with high velocity features (HVF). A HVF is defined as a feature which has a minimum which is greater than  $6000\text{ km s}^{-1}$  faster than the photospheric velocity. The most prominent HVFs for SNe Ia are Ca II H&K, Si II  $\lambda 6355$  and Ca NIR triplet. HVF Ca II features are found in all SNe Ia except subluminal ones (Silverman et al., 2015). HVFs of Si II  $\lambda 6355$  are significantly rarer, and they tend to exist at the earliest epochs and mostly in objects with large photospheric velocities, and stronger HVFs in  $\lambda 6355$  are seen in objects which lack C II absorption at early times (Silverman et al., 2015). HVFs have been theorised to be abundance or density enhancements. Abundance enhancements would imply an outer region dominated by Si and Ca. Density enhancements may result from the sweeping up of circumstellar material (CSM) by the highest velocity SN ejecta (Mazzali et al., 2005). They are also thought to be related to geometrical effects, where the HVF has a clumpy structure (Tanaka et al., 2006).

### 1.7.2 Nebular phase

At late times the SN ejecta is optically thin, therefore the inner part of the ejecta can be explored. This phase in the SN explosion is known as the nebular phase. The inner part of a SN ejecta is dominated by semi-forbidden and forbidden transitions (Axelrod, 1980). A normal SNe Ia nebular spectrum is dominated by  $\sim 4700\text{\AA}$  Fe III and  $\sim 5200\text{\AA}$  Fe II features. Figure 1.8 is a nebular spectrum and model of SN 2011fe. This spectrum presents most of the lines in a normal SN Ia spectrum. The nebular spectra provides information about the central density of the exploding WD. For example, a high Fe III

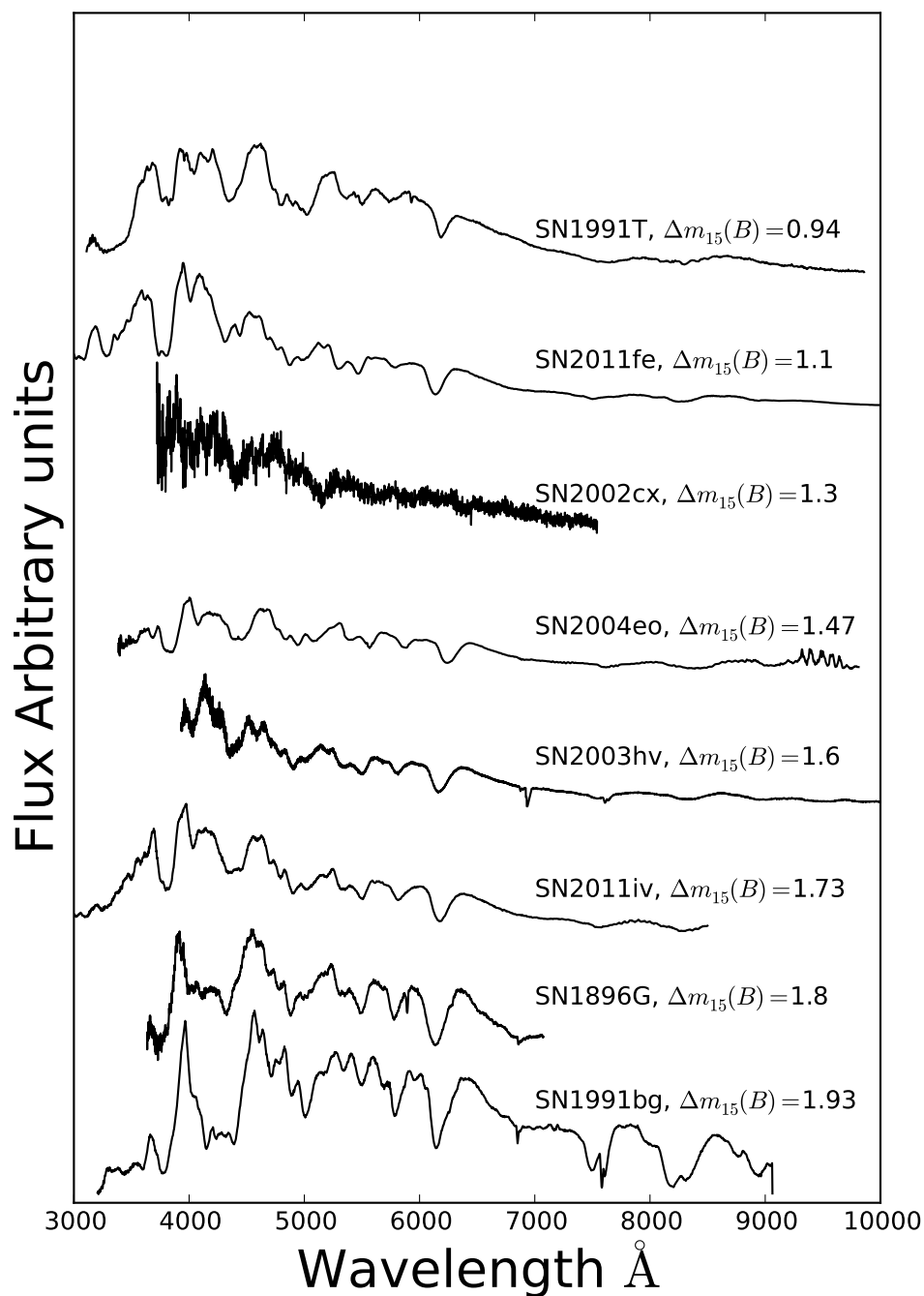


Figure 1.7: Diversity of maximum light spectra of SNe Ia. The spectra are plotted from top to bottom in terms of light curve shape. It should be noted that the spectrum of SN 2004eo was taken at +2 days compared to  $B$  band maximum. Therefore it appears less luminous in the above plot.

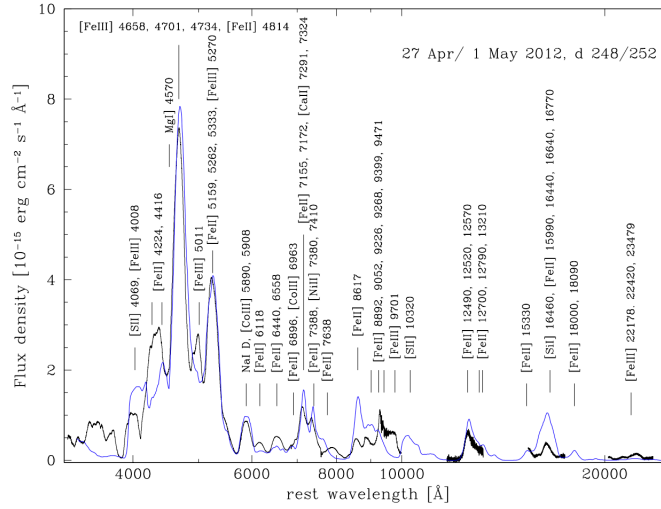


Figure 1.8: A nebular spectrum and model of SN 2011fe (Mazzali et al., 2015).

to Fe II ratio can imply a low central density, such as that seen in SN 2003hv (Mazzali et al., 2008).

## 1.8 SN Ia UV data

Early UV spectra of SNe Ia contain important information about the metallicity of the SN progenitors, as well as the outer layers of the explosion. To date there have been a handful of detailed studies on SN Ia UV spectra. Studying the early ultraviolet (UV) spectra of SNe Ia can let us infer information about the metallicity of the progenitor system (Lentz et al., 2000; Sauer et al., 2008; Mazzali et al., 2014). Maguire et al. (2012) studied individual spectra of 32 low redshift SNe Ia at maximum light. They found that mean low redshift NUV( $2900\text{\AA} < \lambda$ ) spectrum has a depressed flux compared to its intermediate redshift counterpart. Foley et al. (2016) presented the first set of high signal-to-noise ratio of SNe Ia spectra which extend blue-ward of  $2900\text{\AA}$ . The Foley et al. (2016) sample go to  $1800\text{\AA}$ . They present a sample of 10 SN which span the majority of the parameter space of SN Ia optical diversity. They found that

the majority of the UV variance correlates with the optical light curve shape.

Other work has concentrated on taking high cadence UV spectra of individual SN, such as SN 2011fe, 2014J and 2013dy. Mazzali et al. (2014, 2015) present 10 HST near-UV to optical spectra of SN 2011fe. They perform spectral synthesis analysis, and conclude, by using an ad-hoc density profile, that SN 2011fe was a relatively weak explosion and had a stronger high velocity tail compared to a standard W7 explosion model. They also conclude that the metallicity of the SN is half of the solar metallicity, which Foley et al. (2016) agree with. Pan et al. (2015) present a high cadence data set of SN 2013dy, spanning from 0.1 to 500 days after explosion, including 10 epochs of HST UV-to-NIR spectra. SN 2013dy was a normal low velocity gradient SNe Ia with a broad slow declining light curve. They also found that models for SN 2013dy are in good agreement with a solar-metallicity standard W7 model explosion. Foley et al. (2014) presented 10 epochs of observations of HST UV spectra of SN 2014J. SN 2014J was the closest SN Ia in possibly the last 410 years. It was located in M82 and they argue that the peculiar extinction towards SN 2014J is caused by a combination of dust reddening and scattering off circumstellar material.

## 1.9 Outline of thesis

The rest of this thesis will be presented in the following way. The next chapter will present the project on SNe Ia light curves, separated by host galaxy morphology. The following chapter will describe the theory of radiative transfer and the abundance tomography technique and method. The following chapter will present the project on SN 2014J. Modelling of SN 1986G will then be shown. Finally a general discussion and conclusions will be presented.

# 2. Luminosity Distributions of SNe Ia

## 2.1 Preface

To examine the diversity of SNe Ia I first present a large sample analysis of their  $B$  and  $V$ - band light curves separated by host galaxy type. A dataset of 165 low redshift,  $z < 0.06$ , publicly available type Ia supernovae (SNe Ia) has been assembled. Maximum light magnitude ( $M_B$  and  $M_V$ ) distributions of SNe Ia have been produced to explore the diversity of parameter space that they can fill. Before correction for host galaxy extinction it is found that the mean  $M_B$  and  $M_V$  of SNe Ia are  $-18.58 \pm 0.07$  mag and  $-18.72 \pm 0.05$  mag respectively. Host galaxy extinction is corrected using a new method based on the SN spectrum. After correction, the mean values of  $M_B$  and  $M_V$  of SNe Ia are  $-19.10 \pm 0.06$  and  $-19.10 \pm 0.05$  mag respectively. After correction for host galaxy extinction, ‘normal’ SNe Ia ( $\Delta m_{15}(B) < 1.6$  mag) fill a larger parameter space in the Width-Luminosity Relation (WLR) than previously suggested, and there is evidence for luminous SNe Ia with large  $\Delta m_{15}(B)$ . We find a bimodal distribution in  $\Delta m_{15}(B)$ , with a pronounced lack of transitional events at  $\Delta m_{15}(B)=1.6$  mag. We confirm that faster, low-luminosity SNe tend to come from passive galaxies. Dividing the sample by host galaxy type, SNe Ia from star-forming

(S-F) galaxies have a mean  $M_B = -19.20 \pm 0.05$  mag, while SNe Ia from passive galaxies have a mean  $M_B = -18.57 \pm 0.24$  mag. Even excluding fast declining SNe, ‘normal’ ( $M_B < -18$  mag) SNe Ia from S-F and passive galaxies are distinct. In the  $V$ -band, there is a difference of  $0.4 \pm 0.13$  mag between the median ( $M_V$ ) values of the ‘normal’ SN Ia population from passive and S-F galaxies. This is consistent with ( $\sim 15 \pm 10$ )% of ‘normal’ SNe Ia from S-F galaxies coming from an old stellar population. Work from this chapter of the thesis was published in Ashall et al. (2016). All of the work in this chapter was carried out by myself, except calculating for the host galaxy extinction which was calculated by Michele Sasdelli and the K-correction code which was written by Simon Prentice.

## 2.2 Previous studies

In modern times there has been a dramatic increase in SNe data, which means that SNe Ia can be studied in more detail. The increase in available data has meant that large sample studies can now be performed, allowing one to gain more information about the variation in SNe Ia properties. A few studies have attempted to build the luminosity functions (LF) of SNe Ia. Such information would be useful because it would make it possible to quantify the incidence of different subtypes of SNe Ia, and thus of their progenitor/explosion scenarios. Li et al. (2011) present a volume-limited LF from LOSS, and find evidence for a difference in absolute magnitude between SNe Ia when these are separated into host galaxy bins of E-Sa and Sb-Irr. However, they do not correct for host galaxy extinction. Yasuda & Fukugita (2010) produce a LF of low redshift SN discovered by SDSS-II supernova survey. They claim that the occurrence of type Ia supernovae does not favour a particular type of galaxy, but is predominantly dependent on the luminosity of the galaxy. They also claim that the rate

of SNe Ia is higher by  $31 \pm 35\%$  in late-type than in early-type galaxies. Hicken et al. (2009) present a sample of 185 SNe Ia. They find that 91bg-like SNe Ia are distinct from other SNe Ia in their colour and light curve shape-luminosity relation, and state that they should be treated separately in light curve distance fitter training samples.

Although the use of SNe Ia as cosmological probes is well established, it is also known that a few events do not follow the normal ‘rules’ of SNe Ia. For example, PTF10ops (Maguire et al., 2011) was a sub-luminous SN Ia, but its LC had a normal width. 02cx-like events can also be broad in LC shape and intrinsically dim. Traditional LC fitting methods find it difficult to differentiate between colour and host galaxy extinction, so that, for example, a SN Ia which has a normal LC shape but is intrinsically red may be mistaken for a SN which is normal but has more host galaxy extinction. Furthermore, for cosmological purposes, traditional methods exclude any intrinsically peculiar SNe Ia.

The objective of this project is to include as many peculiar SNe Ia as possible, and hence examine their range and diversity. As there are many subclasses of SNe Ia, an approach different from LC template fitting analysis is taken. This analysis makes as few assumptions as possible so the intrinsic properties of these unusual SNe Ia can be examined. This allows for the possibility that SNe with the same LC shape can have intrinsically different properties. This is achieved by obtaining the distance to the SNe first, from data that do not use the SN as distance indicator, rather than obtaining the distance to the SNe from the LC shape and observed colour information. Although this method is possibly less accurate, it allows us to explore the full parameter space of SNe Ia, and is better at treating peculiar SNe Ia. Furthermore, the method is unique as host galaxy extinction is derived from the spectra rather than the photometry, which helps to break the colour-reddening degeneracy (Saselli et al., 2016), see Section 2.4.6. Because the observed sample cannot be controlled it is not possible to build a

LF, but only a LD, which is however useful as all SNe used here are nearby, suggesting that the sample should be reasonably complete.

A large sample analysis is carried out, which primarily focuses on SN Ia LC properties, separated by host galaxy type. In section 2.3 the data and methods used in this work are presented. Section 2.4 discusses the quality of the data fit. Section 2.5 presents the observed SN Ia luminosity distributions and discusses the Width Luminosity Relation. In Section 2.6 the data are corrected for host galaxy extinction, and separated by host galaxy type. In Section 2.7 the full luminosity distribution is presented. Section 2.8 attempts to separate the distributions of SNe Ia from young and old stellar systems. The main discussion is provided in Section 2.9, and a short summary is presented in Section 2.10.

## 2.3 Data & Method

A dataset of 165 low redshift,  $z < 0.05$ , SNe Ia with publicly available data has been assembled. Their redshift distribution is shown in Figure 2.1. The photometric data in this work come from a variety of public sources, see Table 1. The mean redshift of the sample is  $z = 0.019$ . When comparing SN Ia LCs and their derived parameters it is essential that they have sufficient temporal coverage, as overinterpolating or incorrectly extrapolating the data can cause incorrect results. All SNe in the data set used in this work have good temporal coverage, at least 6 data points, from maximum to +15 days and at least one pre-maximum data point. The data used in this work were published in the standard Johnson-Cousin filter system, and no filter conversions were carried out in this analysis. The  $B$  and  $V$ -band filters are used for the analysis as this is where SNe Ia peak in flux; these bands are also historically the most often used, and therefore the best sampled. Most of the optical lines are within the  $B$  and  $V$  passbands,

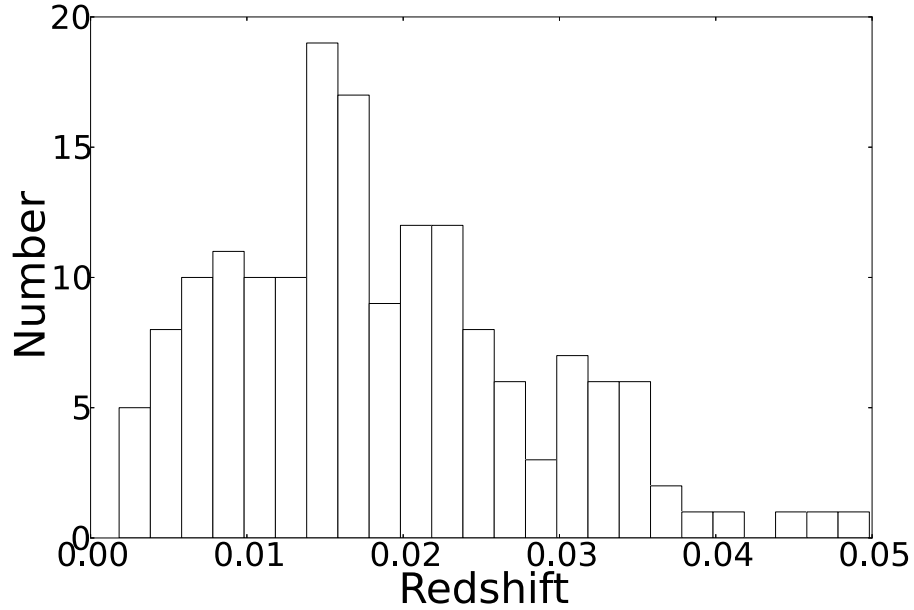


Figure 2.1: Redshift distribution of the SNe Ia used in this work. The bin sizes are  $z=0.002$ .

Table 2.1: Sources of the data.

Reference	Number of SNe Ia
Ganeshalingam et al. (2010)	102
Hicken et al. (2009)	24
Hicken et al. (2012)	18
Riess et al. (1999)	10
Individual papers <sup>a</sup>	11

<sup>a</sup> See Table 2.2

therefore these bands are the best to study the diversity of SNe Ia. There is an obvious bias in our sample caused by the fact that most data were obtained by magnitude-limited surveys. However, as many SNe Ia as possible are used to avoid small sample statistics. Because the data come from a range of sources it is not possible to carry out completeness corrections, therefore in this work we produce luminosity distributions (LD), which can show the diversity of SNe Ia, rather than luminosity functions (LF).

In order to avoid introducing any further biases, here it is not assumed that two

Table 2.2: The reference of the 11 SNe Ia mentioned in Table 2.1.

SNe name	Reference
SN 1986G	Phillips et al. (1987)
SN 1990N	Lira et al. (1998)
SN 1991bg	Krisciunas et al. (2004)
SN 1991T	Krisciunas et al. (2004)
SN 1998aq	Riess et al. (2005)
SN 2000ca	Krisciunas et al. (2004)
SN 2000E	Valentini et al. (2003)
SN 2001bt	Krisciunas et al. (2004)
SN 2001cz	Krisciunas et al. (2004)
SN 2001el	Krisciunas et al. (2003)
SN 2003du	Anupama et al. (2005)

SNe Ia that have the same LC shape necessarily also have the same intrinsic luminosity and colours (unlike, e.g., Riess et al., 1996). This is done by first finding an independent distance to each SN and using that distance to determine the luminosity of the SN. The distances were derived using the local velocity field model of Mould et al. (2000), which takes into consideration the influence of the Virgo Cluster, the Great Attractor, the Shapley Supercluster, and the CMB. To verify the reliability of the distance measurements they were checked against Cepheid distances for 5 SNe Ia which occurred in galaxies with Cepheid distance measurements. It was found that the distances to the SNe Ia are consistent with the Cepheid distances (within 0.06 Mpc). The velocity field model requires a value of  $H_0$ . Cosmological parameters which are consistent with Cepheid measurements are used, i.e.  $H_0=73 \text{ km s}^{-1} \text{ Mpc}^{-1}$ ,  $\Omega_m = 0.27$ ,  $\Omega_\Lambda = 0.73$ . It should be noted that a change in  $H_0$  would cause a global shift in values, but it would not directly affect the results in this work.

Before different SNe can be compared their photometry must be dereddened and converted to rest frame. All SNe were corrected for foreground Galactic extinction using the Schlafly & Finkbeiner (2011) map and assuming  $R_v = 3.1$ . In this chapter, from this point forward all of the data has been corrected for MW extinction. Where

Table 2.3: Statistics of the data, not corrected for host galaxy extinction has been applied.

Amount of SNe	All 165	S-F 134	Passive 26	E 17	S0 9
$\overline{M_B}$	$-18.58 \pm 0.07$	$-18.63 \pm 0.07$	$-18.29 \pm 0.21$	$-18.29 \pm 0.24$	$-18.30 \pm 0.39$
$\sigma M_B$	0.82	0.77	1.06	0.99	1.17
$\overline{\Delta M_{15B}}$	$1.14 \pm 0.03$	$1.11 \pm 0.03$	$1.29 \pm 0.08$	$1.30 \pm 0.10$	$1.28 \pm 0.12$
$\sigma \Delta M_{15B}$	0.32	0.30	0.39	0.40	0.35
$\overline{M_V}$	$-18.72 \pm 0.05$	$-18.75 \pm 0.05$	$-18.52 \pm 0.15$	$-18.50 \pm 0.17$	$-18.56 \pm 0.29$
$\sigma M_V$	0.61	0.58	0.76	0.71	0.86
$\overline{\Delta m_{15V}}$	$0.68 \pm 0.01$	$0.67 \pm 0.01$	$0.77 \pm 0.05$	$0.79 \pm 0.06$	$0.74 \pm 0.07$
$\sigma \Delta m_{15V}$	0.18	0.16	0.25	0.25	0.22
$(B - V)^1$	$0.11 \pm 0.02$	$0.11 \pm 0.02$	$0.17 \pm 0.06$	$0.16 \pm 0.07$	$0.20 \pm 0.10$
$\sigma(B - V)^a$	0.25	0.24	0.29	0.29	0.29

any further discussion is made with regards to parameters with and without extinction, this refers to host galaxy extinction. The data were converted to the rest frame and K-corrections were applied. A time series of spectra of SN 2011fe (Mazzali et al., 2014) were used as a template to calculate the K-corrections, the corrections were carried out in accordance with Oke & Sandage (1968). Using SN 2011fe as a template is making an assumption about the SED of the SN, however this affects the fluxes in our final results by less than 5% in most cases. The K-corrections were applied to each SN at the corresponding redshift and epoch, using both the  $B$  and  $V$ -bands.

Finding the host galaxy morphology of each SN in the dataset is integral to this study. Host galaxy types were obtained from NED<sup>2</sup>. The dataset was separated into two galaxy Hubble type bins, E-S0 (passive galaxies) and Sa-Irr (star forming (S-F) galaxies). Only two bins were chosen to separate the sample, as the properties of the stellar populations are different in each bin. Also, using more bins would significantly decrease the sample in each bin. E+S0 galaxies have an older stellar population with little or no star formation. Out of the sample of 165 SNe, 134 (82%) SNe are from the Hubble Sa-Irr bin, 26 (13%) are from the E+S0 bin, of which 17 (10%) are from

<sup>2</sup> NASA/IPAC Extragalactic Database (NED)

elliptical galaxies and 9 (5%) are from S0 galaxies. Finally, 5 SNe (3%) are from galaxies whose host type could not be determined. Binning the SNe by host galaxy type does not decrease the sample as much as distinguishing by star forming rates or galaxy stellar mass.

133 (81%) of the SNe were classified as spectroscopically ‘normal’, 14 (9%) 91T or 99aa-like, 14 (8%) as 91bg-like and 4 (2%) as 02cx-like. Comparing this to the rates of SNe Ia from Li et al. (2011) (70% normal, 15% 91bg, 9% 91T, 5% 02cx) shows that the public data set has a bias of too many ‘normal’ SNe Ia and fewer dimmer SNe. The lack of 91-bg like events in the sample could be due to their short rise time, which makes them harder to detect before maximum light. SNe without maximum light information would be excluded from the sample in this work. Additionally, 91bg-like SN are dimmer events and are therefore affected by Malmquist bias. This does raise the issue that if one wants a true representation of the intrinsic properties of SNe Ia, a very high cadence, deep and volume-limited survey is required, as well as a lot of ground-based spectroscopic follow up, however this is not available. The Large Synoptic Survey Telescope (LSST) which will come online in 2020 will provide the cadence required for this (Ivezic, 2014). It should be noted that the host galaxy subtraction from Li et al. (2011) excludes the central 2.4 – 3.2 arcsec region of the host galaxies, so the true rate may differ from theirs.

SNe Ia photometry, to first order, can be analysed using two parameters, the decline rate or stretch of the LC and the colour correction of the SNe. This is traditionally done using LC template fitters, and is therefore based on existing assumptions, data and templates. In reality SNe Ia are a far more diverse group than these LC fitters can assume, as their spectra show. Therefore, no prior pre-existing LC fitter is used, a different method of fitting the data is applied. In this section it is explained how the photometry is fitted and how the errors are calculated. The LCs are produced by using

a smoothed cubic spline, implementing the PYTHON module UNIVARIANT SPLINE, on the photometry which has been K-corrected and dereddened for foreground Galactic extinction. These values are used as the final values of the apparent magnitude and light curve shape, as measured by the parameter  $\Delta m_{15}(B)$ , the difference in magnitude between maximum and +15 days (Phillips et al., 1999). This process was carried out for both the  $B$  and  $V$ -bands. The two spline fits were subtracted to obtain the  $B - V$  curve, and from this the colour at  $B$  maximum,  $(B - V)_{B_{\max}}$ , was obtained. The distance modulus was used to obtain the absolute magnitudes  $M_B$  and  $M_V$  of all SNe in the sample.

To compute the errors on the apparent magnitude and  $\Delta m_{15}$ , all of the photometric errors are treated as Gaussians. Each photometric point is randomly varied, in accordance to the weighting of a Gaussian. From this new LCs are produced, using the method discussed above. This was done 1000 times per SN, and the standard deviation in the spread of values is taken as the errors on apparent magnitude and  $\Delta m_{15}(B)$ . As an example of this process, Figure 2.2 shows the photometry and fitted LCs for SN 2000dn. The peak apparent magnitude for SN 2000dn is  $16.63 \pm 0.03$  mag and the decline rate  $\Delta m_{15}(B) = 1.11 \pm 0.07$  mag. Only the LC up to 30 days past  $B$ -band maximum is fitted, as late time photometry is not analysed in this work. The plot demonstrates that there is a larger spread in values when the errors on the photometry are larger. On the other hand, high cadence photometry reduces the errors. As SNe are obtained from multiple sources it is not possible to distinguish between systematic errors which could cause a global shift in the LC, and errors such as poor host galaxy subtraction, which would affect the shape of the LC. Therefore the errors of the fits could be overestimated if the errors on the photometry include systematics.

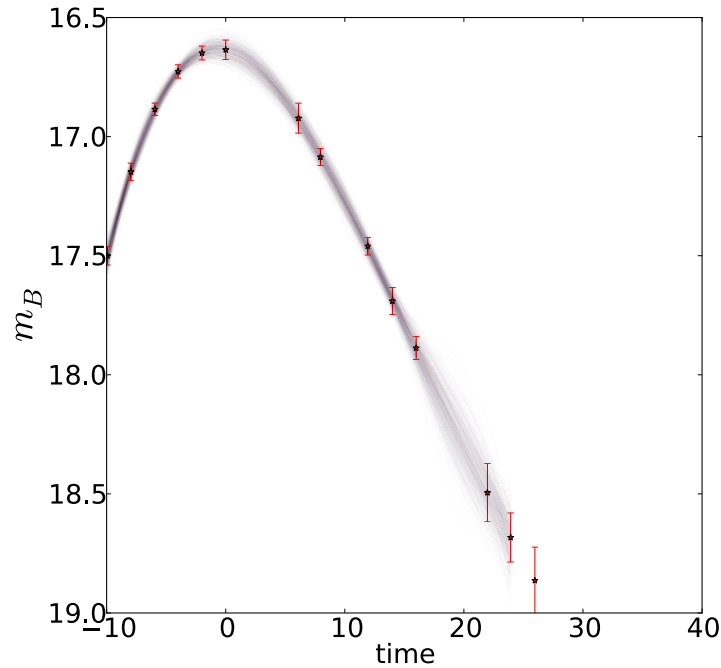


Figure 2.2: An example of the fitting procedure, the  $B$ -band light curve of SN 2000dn. The red points are the photometry and the shaded area is the 1000 LCs derived from these photometry points, as explained in section 2.1.

## 2.4 Quality of LC spline fit

In this section the quality of the spline LC fits are quantified. In Figure 2.3, in the  $B$  band, the residuals between the SN data and fitted LC for 46 randomly selected SN from the sample are plotted. The residuals in this plot are less than 0.05 mag for each SN. These are significantly smaller than the errors, which were taken as the errors on the photometric data. Such small residuals can be produced as the LC is only fitted until 20 days past maximum, and only SNe with very good temporal coverage are selected. Figure 2.4 shows the same residuals using the  $V$  band, the residuals for these bands are also less than 0.05 mag. The residuals in these plots are constant as a function of time, therefore there are no systematic residuals with phase.

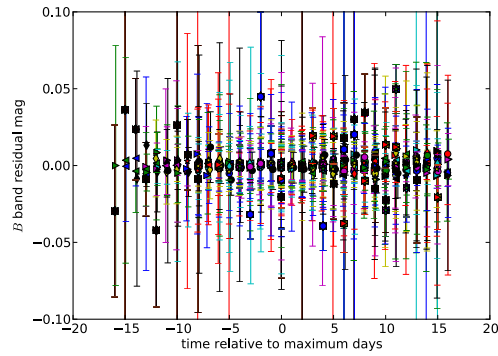


Figure 2.3: The  $B$  band residuals between the SN photometry and LC spline fit, as a function of time. Data from 46 randomly selected SNe are used.

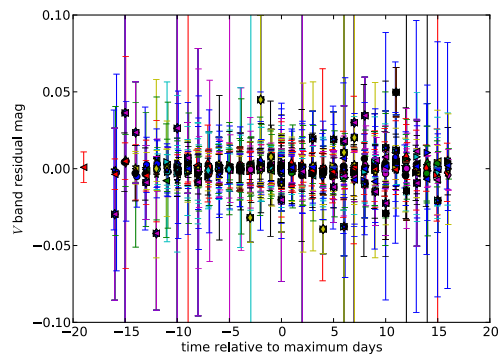


Figure 2.4: The  $V$  band residuals between the SN photometry and LC spline fit, as a function of time. Data from 46 randomly selected SNe are used.

## 2.5 Luminosity Distribution

### 2.5.1 $B$ and $V$ luminosity distributions

The  $B$ -band absolute magnitude and decline rate distributions of the SNe in the sample before correction for reddening are shown in the top panels of Figure 2.5. The bin sizes are 0.2 mag for  $M_B$  and 0.1 mag for  $\Delta m_{15}(B)$ . The mean  $B$ -band absolute magnitude of the sample is  $\bar{M}_B = -18.58 \pm 0.07$  mag, and the sample ranges from  $-19.8$  to  $-15.6$  mag. There is no definitive peak in absolute magnitude in this distribution, which is due to the missing correction for host galaxy extinction and to the ‘tail’ of sub-luminous SNe. The distribution in  $\Delta m_{15}(B)$  is bimodal, with two peaks at  $0.9 - 1.0$  mag and  $1.7 - 1.8$  mag. A Gaussian-mixture modelling test (GMM; Muratov & Gnedin, 2010) was run to evaluate the likelihood that a bimodal distribution is preferred over a unimodal one. It is found that for  $\Delta m_{15}(B)$  a bimodal distribution is preferred: the probability that the  $\Delta m_{15}(B)$  distribution is unimodal is less than 0.1 per cent. The bimodal distributions was fitted by two Gaussians. Out of the 165 SNe Ia in the sample, the test places  $135.3 \pm 20.8$  SNe (82 per cent) in a Gaussian with mean decline rate  $\Delta m_{15}(B) = 1.034 \pm 0.035$  mag and standard deviation  $0.207 \pm 0.032$  mag, and  $29.7 \pm 20.8$  SNe (18 per cent) in a Gaussian with mean decline rate  $1.713 \pm 0.131$  mag and standard deviation  $0.164 \pm 0.080$  mag. 18% is more than the fraction of 91bg-like SNe in the sample. The bimodal distribution could be due to the presence of sub-Chandrasekhar mass events with large  $\Delta m_{15}(B)$  (e.g. Mazzali & Hachinger, 2012; Mazzali et al., 2011), or to delayed-detonation explosions with a range of transition densities from deflagration to detonation: Höflich et al. (2002) find that for a range of smoothly distributed transition densities there is a lack of SNe Ia with  $^{56}\text{Ni}$  mass between  $0.15$  and  $0.25 M_\odot$ . This gap corresponds to the lack of SNe Ia at  $\Delta m_{15}(B)=1.6$  mag seen in Figure 2.5.

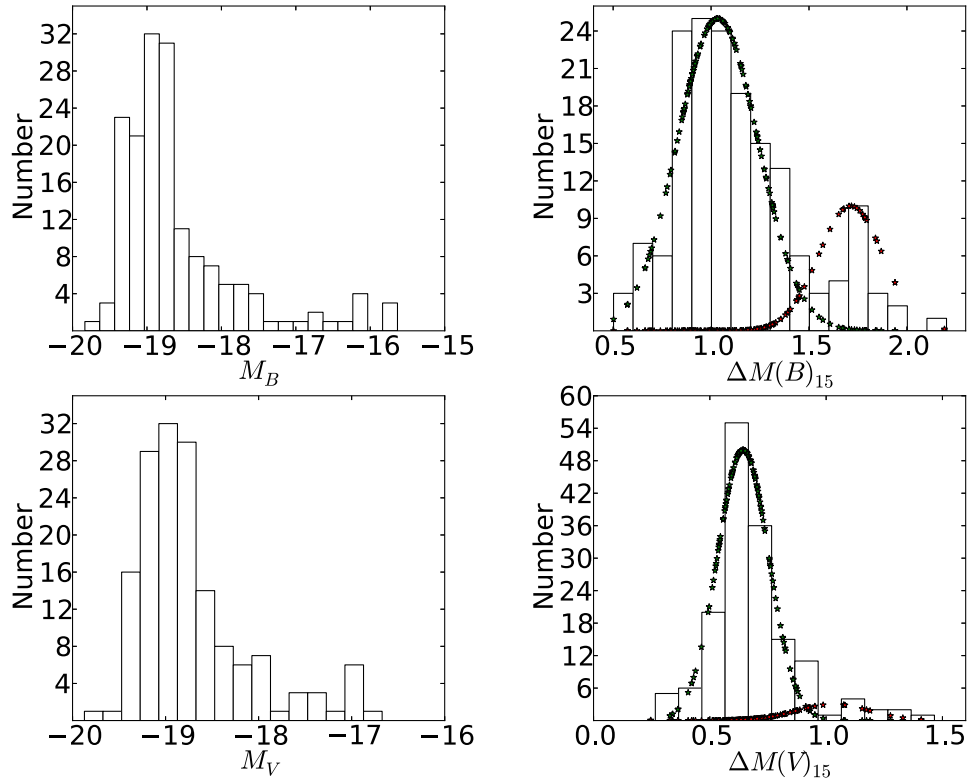


Figure 2.5: The luminosity distributions and  $\Delta m_{15}$  distributions of the SN sample before correction for reddening. *Top*: The left plot is a distribution of  $B$ -band absolute magnitude, and the right plot is the distribution of  $\Delta m_{15}(B)$ . *Bottom*: The left plot is a distribution of  $V$ -band absolute magnitude, and the right plot is the distribution of  $\Delta m_{15}(V)$ . In these plots the SNe have not been corrected for host galaxy extinction. The stars in two right hand panels are the Gaussians calculated from the GMM tests.

SNe in the trough between the two peaks are typically classified as ‘transitional’, with examples being SNe 2004eo (Pastorello et al., 2007) and 2012ht (Yamanaka et al., 2014). Transitional SNe bridge the gap between ‘normal’ and 91bg-like SNe Ia. The ejected  $^{56}\text{Ni}$  masses ( $M_{\text{Ni}}$ ) of transitional SNe Ia lie near the lower limit of the  $M_{\text{Ni}}$  distribution of normal SNe Ia. There is still a lack of published literature on transitional SNe Ia. It is these objects which could help define whether 91-bg-like SNe Ia arise from a separate population or there is a smooth distribution of properties SNe Ia. iPTF13ebh, SN 1986G and SN 2003hv are all classified as transitional SNe Ia. None of these events follow the normal paradigm of SNe Ia. SN 2003hv may have less mass in the inner layers of the ejecta than Chandrasekhar mass density profiles predict: synthetic nebular models were unable to produce the high Fe III/Fe II ratio in the optical spectrum along with the low infrared flux using a W7 density profile (Leloudas et al., 2009), but a lower mass yielded good results (Mazzali et al., 2011). SN 1986G was the first reported SN of this type. It was spectroscopically similar to sub-luminous SNe, showing a (weaker) Ti II feature, a large ratio of the Si II lines (Nugent et al., 1995; Hachinger et al., 2006) and narrow unblended lines in the Fe $\sim$ 4800 Å feature (Phillips et al., 1987). iPTF13ebh showed several strong NIR C I lines in the early time spectra, but no strong C I lines in the optical (Hsiao et al., 2015).

It should be noted that Maguire et al. (2014) do not find a bimodal distribution in  $\Delta m_{15}$  when they convert their values of stretch to  $\Delta m_{15}$ . This may indicate that the double-peak distribution in  $\Delta m_{15}$  could be a selection effect. However, it is unclear how reliable the conversion from stretch to  $\Delta m_{15}(B)$  is. Furthermore, Maguire et al. (2014) use data from a flux limited survey, and therefore the difference between their distribution and ours could stem from the lack of observed SN 91bg-like events in their sample. Burns et al. (2014) state that  $\Delta m_{15}(B)$  is an unreliable parameter for fast declining SNe Ia with  $\Delta m_{15}(B) > 1.7$  mag, because for these SNe there is a

degeneracy between LC shape and  $\Delta m_{15}(B)$ . Here, however,  $\Delta m_{15}(B)$  is used only to discriminate between normal and sub-luminous SNe Ia, which is sufficient for our analysis.

The lower part of Figure 2.5 presents the  $V$ -band absolute magnitude and  $\Delta m_{15}(V)$  distributions. Bin sizes are again 0.2 mag and 0.1 mag respectively. The mean  $M_V$  value is  $\bar{M}_V - 18.72 \pm 0.05$  mag, while  $\Delta m_{15}(V) = 0.68 \pm 0.01$  mag. There is no statistically significant evidence that the distribution in  $\Delta m_{15}(V)$  is bimodal. Although not statistically significant, a bimodal  $\Delta m_{15}(V)$  distribution has been plotted in Figure 2.5 (bottom left panel). The two Gaussians have mean  $\Delta m_{15}(V)$  of  $0.642 \pm 0.015$  and  $0.999 \pm 0.201$  mag and standard deviations of  $0.106 \pm 0.031$  and  $0.166 \pm 0.067$  mag, respectively.

The standard deviation in absolute magnitude, see Figure 2.5, is less in the  $V$ -band (0.61 mag), than in the  $B$ -band (0.82 mag). This is partly caused by the fact that the  $B$ -band is more affected by extinction. It could also be caused by some SNe Ia having broad, a High Velocity Ca II feature at  $\sim 3800 \text{ \AA}$  or different amount of line blanketing in the UV, although the latter will not be the largest contributor to the difference.

## 2.5.2 Width Luminosity Relation

The WLR relationship was extended by Phillips et al. (1999) and then Taubenberger et al. (2008) to include sub-luminous SNe Ia. Figure 2.6 shows this relation within the context of this work. It is clear that there is an underlying correlation (‘The Phillips Relation’) with some scatter. The relation from Phillips et al. (1999) is plotted in Figure 2.6 to show this. SNe Ia with low luminosity but  $\Delta m_{15}(B) < 1.6$  are likely to be affected by host galaxy extinction, but the exact amount cannot be determined using only this plot. Faster-declining SNe tend to come from passive galaxies and are less affected by extinction. Therefore, the ‘tail’ in the WLR, which was first pointed out

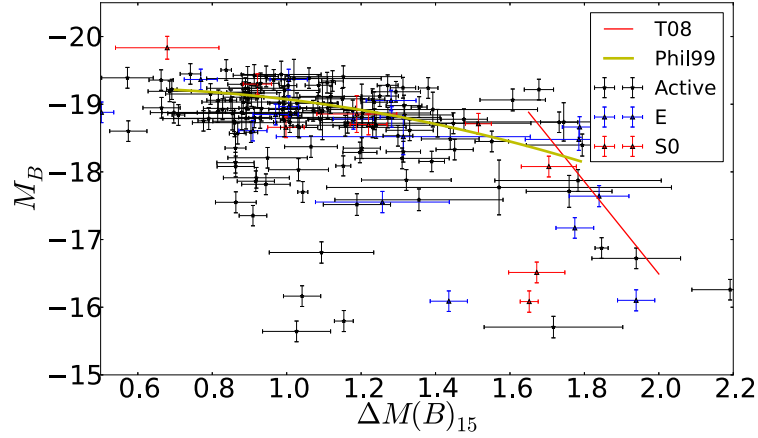


Figure 2.6: The  $B$ -band WLR before reddening correction. The black points are SNe from S-F galaxies, the blue points are SNe from E galaxies, and the red points are SNe Ia from S0 galaxies. The yellow line is the WLR given in Phillips et al. (1999), and the red line is the relation given for the subluminous tail from Taubenberger et al. (2008).

by Taubenberger et al. (2008), is likely to be intrinsic, and not the effect of extinction. Their relation for the subluminous tail is also plotted in Figure 2.6. Furthermore, there is a dearth of SNe at  $\Delta m_{15}(B) \sim 1.6$  mag, where the SNe transition from ‘normal’ to sub-luminous. Interestingly this gap is where the two relations from Phillips et al. (1999) and Taubenberger et al. (2008) meet.

To overcome the effect of extinction, one could select only SNe with a very small colour term,  $(B-V)_{\text{Bmax}} < 0.01$ , as they are thought to be less affected by host galaxy extinction. The top panel in Figure 2.7 shows that the scatter in the WLR plot is indeed reduced when only these SNe are selected. A second-order polynomial line of best fit is obtained, shown as the blue line in Figure 2.7. This is given by,

$$M_B = 0.252\Delta m_{15}(B)^2 - 0.015\Delta m_{15}(B) - 19.31 \quad (2.1)$$

However, this approach eliminates any intrinsically red or unusual SNe Ia. The bottom plot in Figure 2.7 shows the residuals from this fit; the mean residual is 0.22 mag. The reduced  $\chi^2$  of the fit is 3.3. When compared to the fit from Phillips et al. (1999)

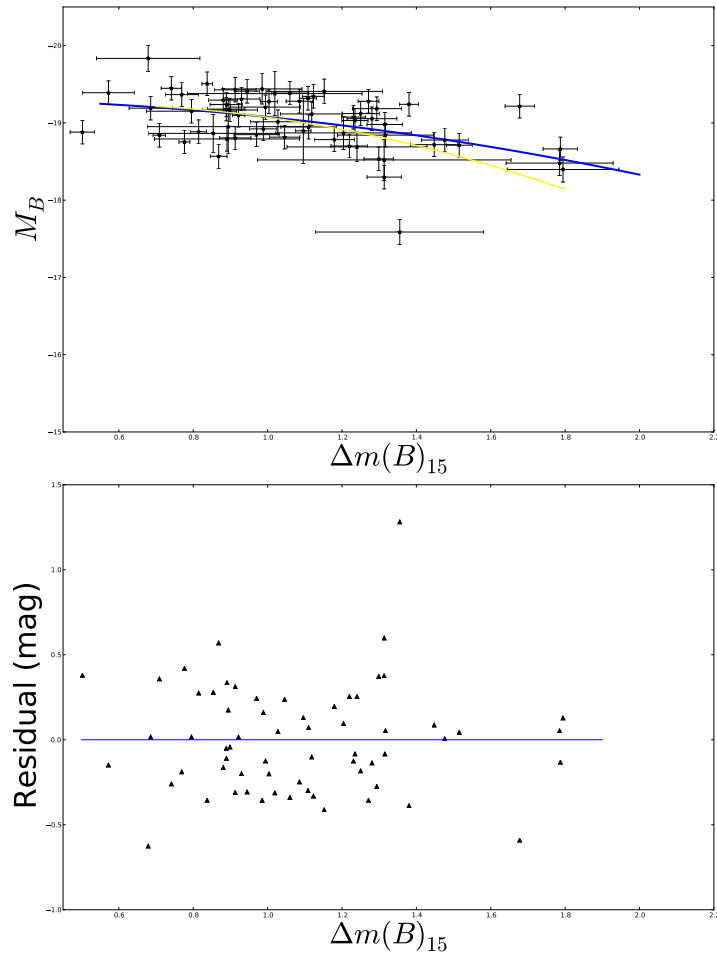


Figure 2.7: *Top:* The WLR before reddening correction including only SNe with  $(B - V)_{Bmax} < 0.01$ . The blue line of best fit is a second order polynomial. The yellow model is the line of best fit from Phillips et al. (1999). *Bottom:* The residuals of the WLR above as a function of  $\Delta m_{15}(B)$ .

(yellow model in the top panel of Figure 2.7), a similar result is found, although the fit is not as tight. The SN which sits clearly off the Phillips relation, with a value of  $M_B > -18$  mag is SN 2008cm. SN 2008cm has been rejected in cosmological studies for being an outlier (Rest et al., 2014). This demonstrates that LCs alone do not contain enough information to differentiate between types of SNe Ia.

## 2.6 Correction for host galaxy extinction

The intrinsic colours of SNe Ia change over time because of the changing properties of the ejecta. Normally, for less luminous SNe this change is over a shorter time scale than for more luminous SNe. It is observationally difficult to distinguish between intrinsic colour properties of a SNe and reddening due to dust between the SNe and the observer. Determining this is central to the full understanding of the nature of SNe Ia, but it is not trivial. Several studies tried to estimate SN Ia colour. The Lira law (Phillips et al., 1999) found that the  $B - V$  colours of SNe Ia, at all decline rates, evolve in a nearly identical way, from +30 to +90 days past  $V$  maximum. It has also been shown that high- and normal-velocity (NV) SNe exhibit significant discrepancies in  $B - V$  and  $B - R$ , but not in other colours (Mandel et al., 2014).

Spectral properties such as equivalent widths (EW) can be used as indicators to attempt to distinguish between colour and host galaxy extinction. EWs are not affected by extinction, and there are intrinsic relationships between the EW of certain lines and the SN LC parameters, such as between  $\text{EW}(\text{Si II } 5972)$  and  $\Delta m_{15}(B)$  (Nugent et al., 1995; Hachinger et al., 2006). When trying to obtain extinction from estimates of reddening, it is important that the correct value of  $R_v$  (the ratio of total to selective extinction) is used. In the Milky Way the average value of  $R_v$  is 3.1 (Cardelli et al., 1989), but it varies depending on the region observed. For SNe Ia very low values of

$R_v$  have sometimes been reported, ranging from 1.1 to 2.2 (Tripp, 1998; Kessler et al., 2009; Guy et al., 2010; Folatelli et al., 2010). Chotard et al. (2011) derived a larger value of  $R_v = 3.1$ , which is consistent with the MW value. Sasdelli et al. (2016) used time-series of SNe Ia spectra in derivative space, which is not affected by poor calibration, to explore host galaxy extinction, and found that  $R_v = 2.9 \pm 0.3$  fits the data the best, and is also consistent with the MW value.

From the WLR in Figure 2.6, it is not possible to tell how much of the scatter is intrinsic and how much is due to extinction, since SNe Ia are not perfectly homogeneous. For almost all astronomical data, correction for both Galactic and host extinction is important, especially when comparing objects. Sasdelli et al. (2014) attempted to break the colour-reddening degeneracy using spectroscopic time series as predictor variables of the intrinsic colour. They built a metric space for SNe Ia independent of extinction using Principal Component Analysis (PCA). The intrinsic spectral evolution of the SNe Ia is represented by a 5-dimensional feature space. This space does not include dust extinction. Two intrinsically similar SNe with different extinction have similar projections in this feature space. Sasdelli et al. (2014) use this feature space to predict the  $B - V$  colour of SNe using a Partial Least Square regression (PLS). Only the intrinsic part of the  $B - V$  colour can be predicted by PLS. The difference between the predicted intrinsic colour and the observed  $B - V$  colour can then be interpreted as due to dust extinction. This yields estimates of  $E(B - V)$  for the individual SNe. With this host galaxy extinction information we can examine the intrinsic properties of SNe Ia.

In this section a correction for host galaxy extinction based on the method of Sasdelli et al. (2016) is applied and the values of  $E(B - V)$  are thus derived. This method removes spectroscopically peculiar SNe Ia that are underrepresented in the data, and therefore can bias our sample towards normal and luminous SNe Ia. Extinction is corrected for using the CCM law (Cardelli et al., 1989) with  $R_v = 2.9$ , and the ap-

proximation

$$\Delta m_{15}(B)_{\text{true}} = \Delta m_{15}(B)_{\text{obs}} + 0.1 \times E(B - V), \quad (2.2)$$

to correct  $\Delta m_{15}(B)$  for extinction is used.  $\Delta m_{15}(V)$  has not been corrected for extinction as the effect is negligible in the  $V$  band (Phillips et al., 1999). This is as for objects with a very large extinction the difference in observed and intrinsic  $V$  band flux is less than that of the  $B$  band, and therefore the time of  $V$  band maximum changes by a negligible amount. Which means the change in  $\Delta m_{15}(V)$  is not affected by  $E(B - V)$ .

As the sample size is reduced in this section of the analysis, the main properties of the SN sample must be verified before and after host galaxy extinction correction is applied, in order to determine whether the reduced sample is selected randomly from the larger one or it is biased towards normal SNe Ia by the selection process. For the sample before correction,  $\bar{M}_B = -18.66 \pm 0.07$  mag, which is comparable to  $-18.58 \pm 0.07$  mag from the larger uncorrected sample. The mean  $\Delta m_{15}(B)$  values from the two samples are also similar,  $1.14 \pm 0.03$  mag and  $1.11 \pm 0.03$  mag for the larger and smaller samples respectively. The mean  $M_V$  values were also found to be similar,  $-18.72 \pm 0.05$  mag and  $-18.77 \pm 0.05$  mag for the larger and smaller samples respectively. Out of the 56 SNe Ia which were removed from the sample 2 were 91-bg like, 4 were- 91T-like and 47 were normal SNe Ia. These SNe were rejected as they had insufficient spectral coverage, so it is not possible to tell if they have a peculiar spectral evolution. The other 3 of the 56 had to be removed from the sample for being spectroscopically peculiar. These were 2005hk (a 2002cx like SN), 2004dt (a highly polarised SN, Altavilla et al. (2007)) and 1999cl (a highly extinguished SN).

Figure 2.8 shows the amount of host extinction for each galaxy type derived with the method of Sasdelli et al. (2016). The top left plot shows how the LD of SNe Ia from S-F galaxies changes when host galaxy extinction is corrected for. The top-

right plot shows that there is a large difference between the values of  $M_B$  before and after extinction correction. If there was no correction for extinction all data points would fall on a linear relation. This is however not the case: 67% of SNe Ia from S-F galaxies are affected by detectable amounts of host galaxy extinction. The average  $E(B - V)$  of all SNe Ia from S-F host galaxies is  $0.130 \pm 0.023$  mag. In contrast, only 43% of the SNe Ia from passive galaxies are affected by detectable amounts of host galaxy extinction, as would be expected due to the lack of dust in early-type galaxies. Their mean  $E(B - V) = 0.040 \pm 0.013$  mag. Therefore on average SNe from passive galaxies have almost negligible host galaxy extinction. The average change in absolute  $B$  magnitude for SNe Ia from S-F galaxies is 0.50 mag, compared to 0.15 mag for SNe from passive galaxies.

### 2.6.1 Luminosity Distribution

The top left panel of Figure 2.9 shows the  $M_B$  distribution of the SNe after correction for host galaxy extinction. The distribution has mean  $\bar{M}_B = -19.09 \pm 0.06$  mag and a standard deviation  $\sigma(M_B) = 0.62$  mag. The LD consists of a ‘normal’ distribution of SNe Ia and of a sub-luminous ‘tail’ comprising faster declining SNe Ia. A similar result is found in the  $V$ -band (Figure 7, lower left), where the distribution has mean  $\bar{M}_V = -19.10 \pm 0.05$  mag and  $\sigma(M_V) = 0.52$  mag. From Figure 2.9 it is apparent that when corrected for extinction ‘normal’ SNe Ia lie within the range  $-20 > M_B > -18$ , and similarly for  $M_V$ .

### 2.6.2 Host galaxy extinction

The right hand side of Figure 2.9 shows the distribution of decline rates. In the  $B$  band, the distribution has a mean  $\Delta m_{15}(B) = 1.12 \pm 0.03$  mag and a standard deviation of 0.32. A bimodal distribution is still visible in  $\Delta m_{15}(B)$  showing a lack of ‘transi-

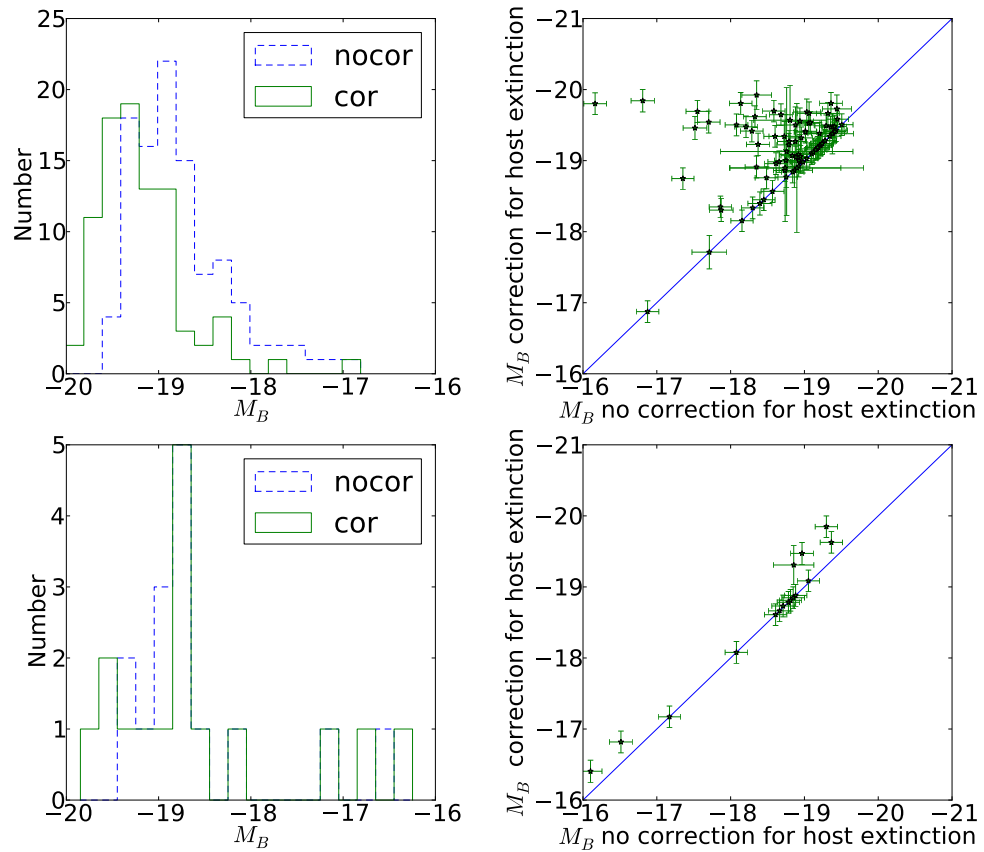


Figure 2.8: *Top*: Left: The  $M_B$  LD of the SNIa from S-F galaxies, before and after correction for extinction. Right: compares the values of  $M_B$ , again before and after correction for extinction, for SNe from S-F galaxies. *Bottom*: Left: The  $M_B$  LD of the SNe Ia from passive galaxies, before and after correction for extinction. Right:  $M_B$ , before and after correction for extinction, for SNe from passive galaxies.

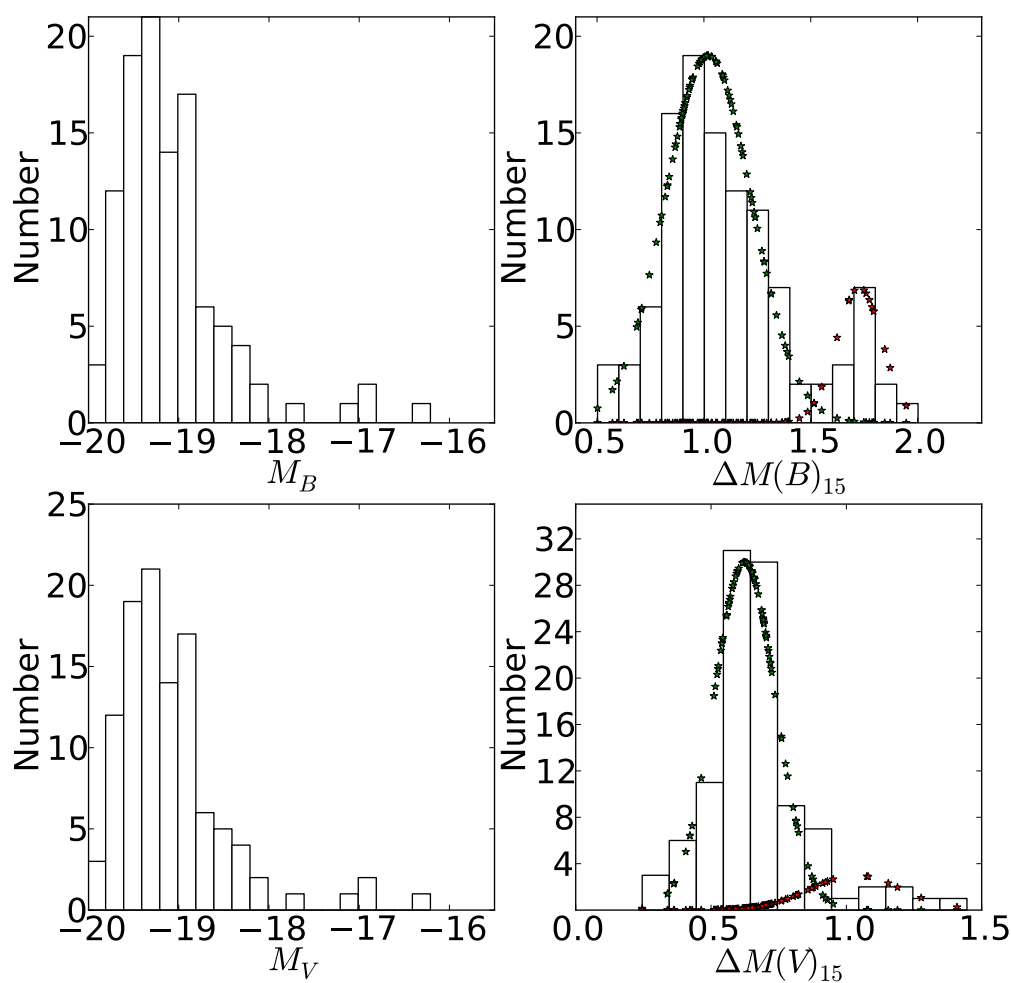


Figure 2.9: *Top*:  $B$ -band luminosity distribution, corrected for host galaxy extinction. The bin sizes are 0.15 and 0.1 mag for the  $M_B$  and  $\Delta m_{15}(B)$  plots respectively. *Bottom*:  $V$ -band luminosity distribution, corrected for host galaxy extinction. The bin sizes are 0.15 and 0.1 mag for the  $M_V$  and  $\Delta m_{15}(V)$  plots respectively. The stars in the right hand panel are the Gaussians calculated from the GMM tests.

tional' objects. The gaussian mix modelling test was run on the  $\Delta m_{15}(B)$  now it has been corrected for extinction. The likelihood that this sample came from a unimodal distribution was less than 0.1%. A bimodal distribution is preferred. One which takes the form of two Gaussians. The first with a mean of  $1.020 \pm 0.022$ , a  $\sigma = 0.204 \pm 0.032$  and contains  $93 \pm 11.2$  SNe Ia. The second distribution has a mean of  $1.727 \pm 0.125$ , a  $\sigma = 0.108 \pm 0.064$  and contains  $16 \pm 11.2$  SNe Ia. In the  $V$  band it was found that there is an 11% chance that the sample came from a unimodal distribution. Therefore, there is no evidence that it is bimodal. If there were two gaussian distributions that formed the set, the first would have a mean of  $0.624 \pm 0.013$ , a  $\sigma = 0.115 \pm 0.019$  and contain  $91 \pm 16.3$  SNe Ia. The second would have a mean of  $1.037 \pm 0.221$ , a  $\sigma = 0.162 \pm 0.081$  and contain  $18 \pm 16.3$  SNe Ia.

Table 2.5 contains the statistics of the SNe Ia sample when corrected for extinction.

### 2.6.3 LD by host galaxy type

The SNe were separated by host galaxy type, as discussed in Section 4.3. Figure 2.10 shows the luminosity distributions of SNe Ia separated by host galaxy type, after correction for extinction. In the  $B$ -band, SNe from S-F galaxies have  $\bar{M}_B = -19.20 \pm 0.05$  mag, while SNe from passive galaxies have  $\bar{M}_B = -18.57 \pm 0.24$  mag, which is  $0.63 \pm 0.24$  mag dimmer. In the  $V$ -band, SNe Ia from S-F galaxies have  $\bar{M}_V = -19.19 \pm 0.05$  mag, while SNe from passive galaxies have  $\bar{M}_V = -18.71 \pm 0.18$  mag. The difference in  $V$ -band average absolute magnitude is  $0.48 \pm 0.24$  mag. Faster declining SNe tend to favour passive galaxies, which is expected as sub-luminous SNe tend to favour old stellar populations (Howell, 2001). The mean  $\Delta m_{15}(B)$  for SNe from passive galaxies is  $1.29 \pm 0.10$  mag, compared to  $1.10 \pm 0.03$  mag for SNe Ia from S-F galaxies. In Figure 2.10 it is apparent that some of the less luminous SNe Ia are brighter in the  $V$  band than the  $B$  band. This is not an effect of binning the data.

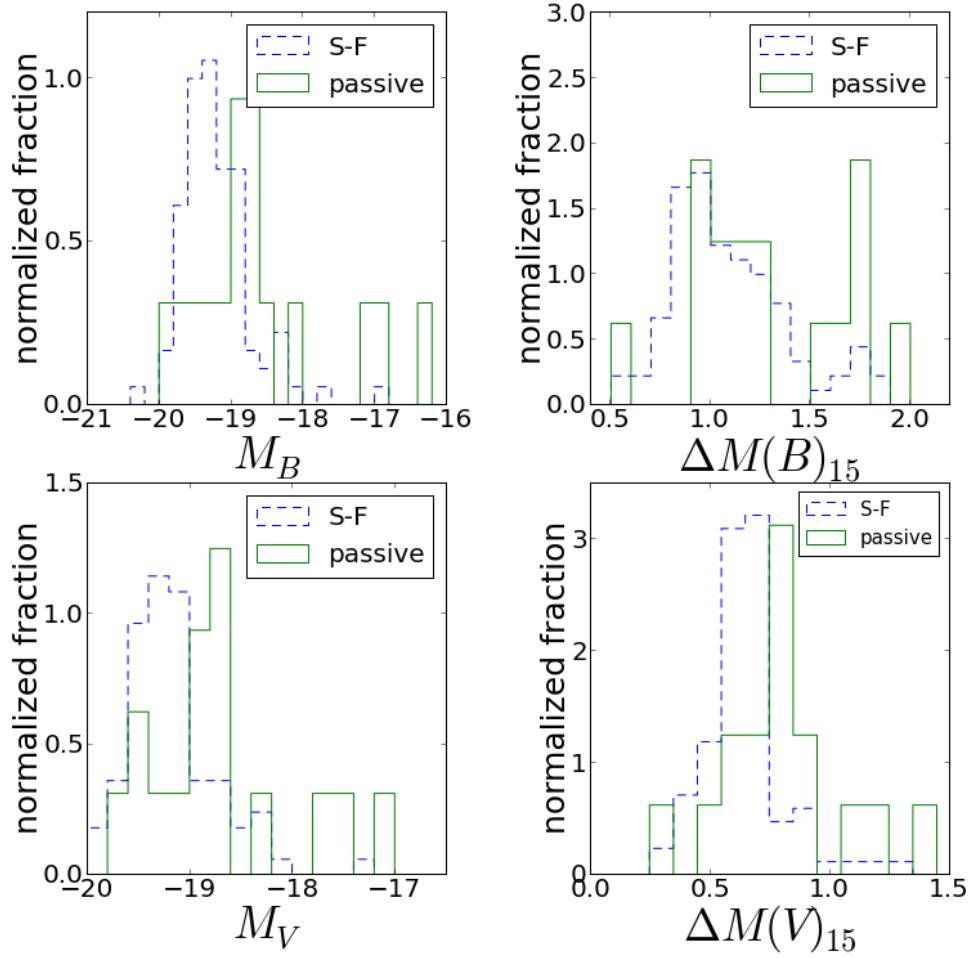


Figure 2.10: SNe Ia separated by host galaxy type, after correction for host galaxy extinction. Blue shows SNe Ia from S-F galaxies and green is SNe Ia from passive galaxies.

It is infact due to subluminous SNe Ia being intrinsically dimmer and cooler than normal SNe Ia, and therefore peak in the V band. This is effect is seen at magnitudes dimmer than  $M_B$  less than  $-18$  mag, see Figure 2.11.

K-S tests were run on the distributions from each host galaxy, see Table 5. The probability that the  $M_B$  samples come from the same parent distribution is less than 0.1%. There is marginal evidence for a difference between the  $\Delta m_{15}(B)$  distributions, with a 12% probability that they came from the same parent sample. When these tests were run on the V-band, it was found that the  $M_V$  distributions had less than a 0.4%

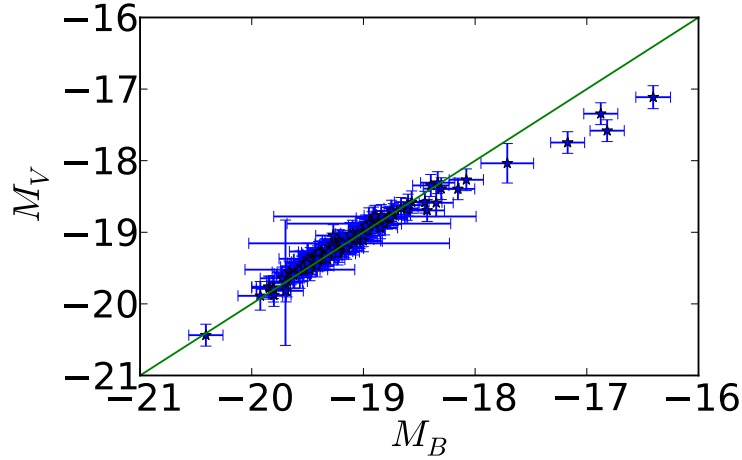


Figure 2.11:  $M_B$  vs  $M_V$  for all SNe Ia in the sample.

probability of coming from the same parent distribution. The cumulative probability distributions of the samples used in the K-S tests can be found in Figure 2.12.

The mean colour term for SNe Ia, after correction for host galaxy extinction, is  $-0.008 \pm 0.013$  mag. SNe Ia from S-F galaxies have an average  $(B - V)_{B_{\max}} = -0.025 \pm 0.010$  mag. This is  $0.12 \pm 0.06$  mag bluer than for SNe Ia from passive galaxies, which have an average colour term of  $0.095 \pm 0.060$  mag. This demonstrates that SNe Ia from S-F galaxies are intrinsically bluer than those from passive galaxies.

## 2.6.4 WLR after extinction correction

Figure 2.13 shows the WLR of the SNe Ia in the sample after correction for host galaxy extinction. There is a larger intrinsic scatter in this WLR compared to when only SNe with  $(B - V)_{B_{\max}} < 0.01$  mag are used. This indicates that the parameter space that SNe Ia can fill is much larger than originally thought. This is the result of the breaking of the colour/extinction degeneracy by the method of Sasdelli et al. (2016). The bulk of ‘normal’ SNe Ia lie in a  $M_B$  range of  $\sim 1.5$  mag, rather than showing a tight correlation between LC shape and absolute magnitude. Among SNe with

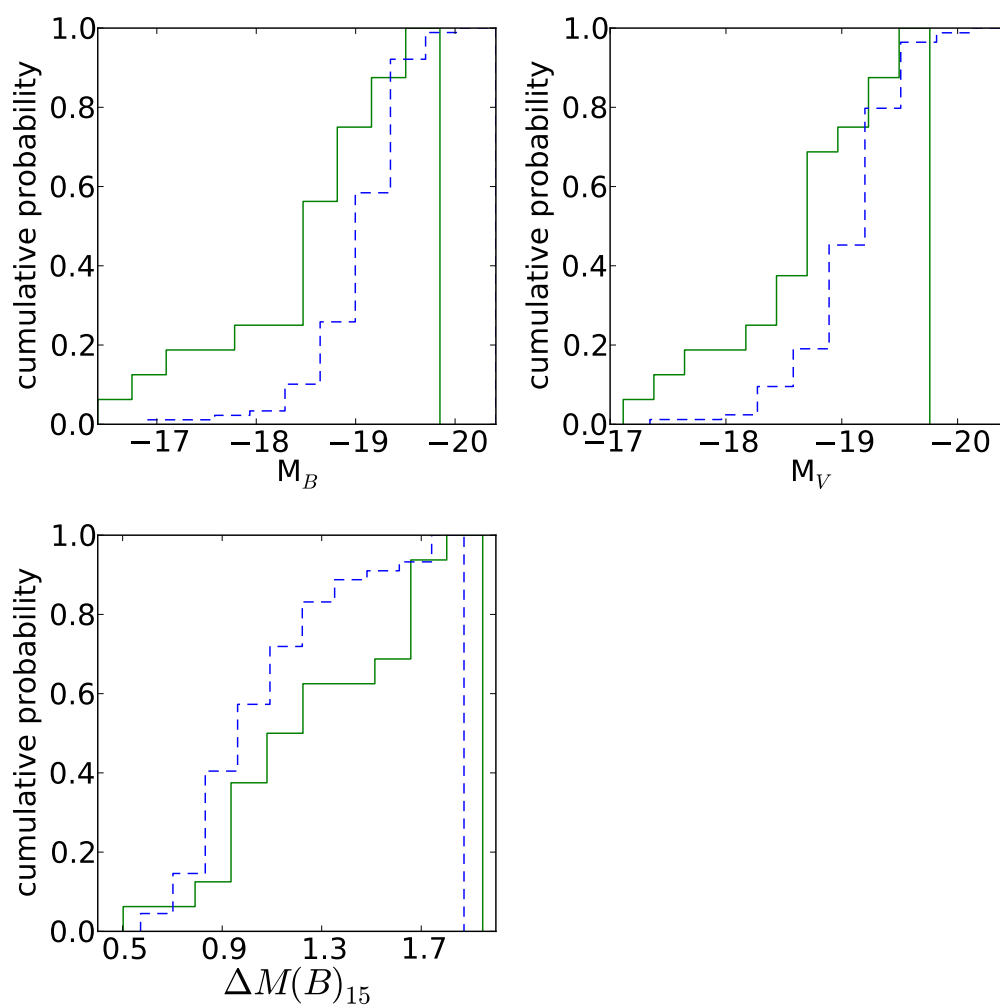


Figure 2.12: The cumulative probability distributions for the samples used in the K-S test. The green solid lines are SNe from passive galaxies, and the blue dashed from SNe from S-F galaxies.

Table 2.4: Statistics of data before correction for host galaxy extinction. The data used in this table are a subset of the full sample.

Amount of SNe	All 109	S-F 89	Passive 16	E 11	S0 5
$\overline{M_B}$	$-18.66 \pm 0.07$	$-18.70 \pm 0.08$	$-18.42 \pm 0.23$	$-18.48 \pm 0.28$	$-18.29 \pm 0.43$
$\sigma M_B$	0.74	0.71	0.94	0.92	0.97
median $M_B$	$-18.85 \pm 0.09$	$-18.88 \pm 0.09$	$-18.80 \pm 0.29$	$-18.81 \pm 0.35$	$-18.71 \pm 0.54$
$\overline{\Delta m_{15} B}$	$1.11 \pm 0.03$	$1.08 \pm 0.03$	$1.29 \pm 0.10$	$1.24 \pm 0.13$	$1.40 \pm 0.13$
$\sigma \Delta m_{15} B$	0.32	0.29	0.39	0.42	0.30
$\overline{(B - V)}$	$0.097 \pm 0.022$	$0.095 \pm 0.025$	$0.132 \pm 0.062$	$0.104 \pm 0.070$	$0.193 \pm 0.118$
$\sigma(B - V)$	0.233	0.233	0.247	0.234	0.263
median $(B - V)$	$0.040 \pm 0.03$	$0.040 \pm 0.03$	$0.039 \pm 0.08$	$0.030 \pm 0.09$	$0.077 \pm 0.15$
$\overline{M_V}$	$-18.77 \pm 0.05$	$-18.81 \pm 0.06$	$-18.60 \pm 0.17$	$-18.63 \pm 0.20$	$-18.53 \pm 0.31$
$\sigma M_V$	0.55	0.52	0.68	0.68	0.68
median $M_V$	$-18.88 \pm 0.07$	$-18.90 \pm 0.07$	$-18.83 \pm 0.21$	$-18.86 \pm 0.26$	$-18.74 \pm 0.38$
$\overline{\Delta m_{15} V}$	$0.67 \pm 0.02$	$0.65 \pm 0.02$	$0.80 \pm 0.06$	$0.79 \pm 0.09$	$0.82 \pm 0.08$
$\sigma \Delta m_{15} V$	0.19	0.16	0.26	0.29	0.17

$\Delta m_{15}(B) > 1.6$  mag, the sub-luminous tail dominates. This is where transitional SNe, with  $1.6 < \Delta m_{15}(B) < 1.8$  mag, and subluminous SNe Ia, with  $\Delta m_{15}(B) > 1.8$  mag, are. These SNe Ia are far more diverse in properties than “normal” ones. In Figure 2.13 the highlighted green mark located well above the WLR is SN 2003cg. This is the SN with the largest extinction,  $E(B - V) = 1.026$  mag. Elias-Rosa et al. (2006) find that SN 2003cg has an anomalous extinction with  $R_v = 1.80 \pm 0.19$  mag. SNe with very high extinction may require a different reddening law, but this is the only case in our sample for which this occurs. For more information on highly extinguished objects see Sasdelli et al. (2016).

## 2.7 Full luminosity distribution

It is apparent that SNe Ia from passive galaxies suffer only from negligibly from host galaxy extinction, with 57% of SNe Ia from passive galaxies having no detectable host galaxy extinction. The mean  $E(B - V)$  for SNe Ia from passive galaxies is  $0.04 \pm 0.013$  mag. In this section the sample of 105 SNe Ia which could be corrected for

Table 2.5: Statistics of the data after correction for host galaxy extinction.

Amount of SNe	All 109	S-F 89	Passive 16	E 11	S0 5
$\overline{M_B}$	$-19.09 \pm 0.06$	$-19.20 \pm 0.05$	$-18.57 \pm 0.24$	$-18.58 \pm 0.27$	$-18.56 \pm 0.47$
$\sigma M_B$	0.62	0.49	0.96	0.91	1.05
median $M_B$	$-19.22 \pm 0.07$	$-19.27 \pm 0.07$	$-18.80 \pm 0.30$	$-18.81 \pm 0.34$	$-18.73 \pm 0.59$
$\overline{\Delta m_{15} B}$	$1.12 \pm 0.03$	$1.10 \pm 0.03$	$1.29 \pm 0.10$	$1.24 \pm 0.13$	$1.41 \pm 0.13$
$\sigma \Delta m_{15} B$	0.32	0.29	0.39	0.42	0.30
$\overline{(B - V)}$	$-0.008 \pm 0.013$	$-0.025 \pm 0.010$	$0.095 \pm 0.060$	$0.079 \pm 0.067$	$0.129 \pm 0.119$
$\overline{(B - V)}$	0.135	0.097	0.239	0.223	0.266
median $(B - V)$	$-0.029 \pm 0.02$	$-0.034 \pm 0.01$	$-0.007 \pm 0.07$	$-0.019 \pm 0.08$	$0.004 \pm 0.15$
$\overline{M_V}$	$-19.10 \pm 0.05$	$-19.19 \pm 0.05$	$-18.71 \pm 0.18$	$-18.71 \pm 0.20$	$-18.73 \pm 0.34$
$\sigma M_V$	0.52	0.45	0.70	0.68	0.76
median $M_V$	$-19.17 \pm 0.06$	$-19.23 \pm 0.06$	$-18.83 \pm 0.22$	$-18.86 \pm 0.26$	$-18.75 \pm 0.43$
$\overline{\Delta m_{15} V}$	$0.67 \pm 0.02$	$0.65 \pm 0.02$	$0.80 \pm 0.07$	$0.79 \pm 0.087$	$0.82 \pm 0.08$
$\sigma \Delta m_{15} V$	0.19	0.16	0.26	0.29	0.17
$\overline{E(B - V)}$	$0.114 \pm 0.019$	$0.130 \pm 0.023$	$0.040 \pm 0.013$	$0.026 \pm 0.013$	$0.070 \pm 0.026$
$\sigma E(B - V)$	0.20	0.21	0.05	0.04	0.06

Table 2.6: K-S tests for SNe with different types of host galaxies, after correction for host galaxy extinction.

Compared distributions	Value used	$P$ value
SNe S-F vs SNe passive	$M(B)$	0.001
SNe S-F vs SNe passive	$\Delta M(B)_{15}$	0.118
SNe S-F vs SNe passive	$M_V$	0.004

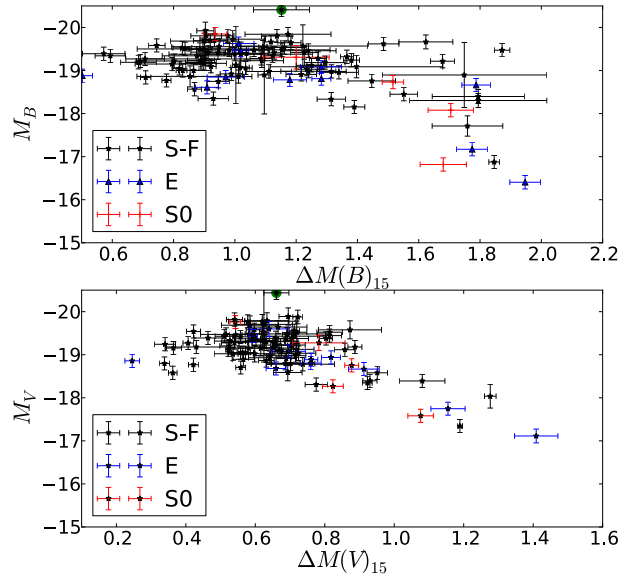


Figure 2.13: The WLR corrected for host galaxy extinction. The black points are SNe from S-F galaxies, the blue are points are SNe from elliptical galaxies and the red points are SNe Ia from S0 galaxies. The green point is SN2003cg. *Top: B-band Bottom: V-band*

host galaxy extinction are used, and the 10 SNe Ia from passive galaxies for which host galaxy extinction could not be derived are added back into the sample. This is done to avoid small sample statistics. It is justified because it is reasonable to assume that the SNe in passive galaxies have very little host extinction<sup>3</sup>. The new sample sizes comprises then 115 SNe, of which 89 are from S-F galaxies and 26 from passive galaxies. Figure 2.14 is the final SNIa luminosity distribution. The mean absolute magnitudes of the full sample are  $\bar{M}_B = -19.04 \pm 0.07$  mag and  $\bar{M}_V = -19.07 \pm 0.06$  mag. Figure 2.15 shows the final SNe Ia  $\Delta m_{15}$  distributions.

Figure 2.14 is the LD plot of the SNe Ia, divided by host galaxy type. It can be assumed that at least three different populations of SNe Ia are present in these plots: a normal population of SNe Ia from S-F galaxies, which dominates the population of

<sup>3</sup> The one exception is SN 1986G which was corrected for extinction of  $E(B - V) = 0.65$  mag (Nugent et al., 1995; Ashall et al., 2016). SNe 1986G is from an S0 galaxy, but sits in the dust lane in NGC 5128.

Table 2.7: Statistics of full LD.

Amount of SNe	All 115	S-F 89	passive 26
$\bar{M}_B$	$-19.04 \pm 0.07$	$-19.20 \pm 0.05$	$-18.48 \pm 0.19$
$\sigma M_B$	0.70	0.49	0.98
median $M_B$	$-19.20 \pm 0.08$	$-19.27 \pm 0.07$	$-18.68 \pm 0.24$
$\bar{M}_V$	$-19.07 \pm 0.06$	$-19.19 \pm 0.05$	$-18.67 \pm 0.14$
$\sigma M_V$	0.57	0.45	0.72
median $M_V$	$-19.16 \pm 0.07$	$-19.24 \pm 0.06$	$-18.78 \pm 0.18$
$\bar{M}_B^a$	$-19.19 \pm 0.04$	$-19.24 \pm 0.04$	$-18.94 \pm 0.11$
$\sigma M_B$	0.43	0.40	0.47
median $M_B$	$-19.23 \pm 0.05$	$-19.27 \pm 0.05$	$-18.80 \pm 0.13$
$\bar{M}_V^b$	$-19.16 \pm 0.04$	$-19.22 \pm 0.04$	$-18.94 \pm 0.10$
$\sigma M_V$	0.43	0.41	0.46
median $M_V$	$-19.19 \pm 0.05$	$-19.25 \pm 0.06$	$-18.86 \pm 0.12$

<sup>a</sup>  $M_B < -18$  mag

<sup>b</sup>  $M_V < -18$  mag

normal SNe, a normal population of SNe Ia from passive galaxies, and a subluminous population, which is dominated by SNe in passive galaxies. The numbers of subluminous SNe in S-F galaxies are too small to determine whether their population has different properties with respect to that in passive galaxies.

The shape of the LD depends strongly on host type. The LDs of SNe Ia in S-F galaxies have Gaussian shapes, with mean magnitudes  $\bar{M}_B = -19.20 \pm 0.05$  mag and  $\bar{M}_V = -19.19 \pm 0.05$  mag and standard deviations of 0.49 and 0.45 mag, respectively. In passive galaxies the SNIa LD is much wider: the mean magnitudes are  $\bar{M}_B = -18.48 \pm 0.19$  mag and  $\bar{M}_V = -18.67 \pm 0.14$  mag, with standard deviations 0.72 mag and 0.98 mag respectively.

To compare the distributions of ‘normal’ SNe Ia from the two different host galaxy types the subluminous SNe Ia must be excluded. This is done by removing any SNe Ia with  $M_B$  and  $M_V > -18.0$  mag. These values are obtained by visual inspection of the plots. It should be noted that the cut off is applied in terms of absolute magnitude

rather than decline rate, as fast declining SNe Ia can be both intrinsically bright and intrinsically dim (Figure 2.13). If the  $^{56}\text{Ni}$  is located further out in ejecta it can cause the SN Ia LC to be bright and fast.

When the subluminous population is removed, the distributions change. S-F galaxies have  $\bar{M}_B = -19.24 \pm 0.04$  mag and  $\bar{M}_V = -19.22 \pm 0.05$  mag, with median values  $M_B = -19.27 \pm 0.05$  mag and  $M_V = -19.25 \pm 0.06$  mag. For passive galaxies,  $\bar{M}_B = -18.94 \pm 0.11$  mag,  $\bar{M}_V = -18.94 \pm 0.10$  mag, with median values  $M_B = -18.80 \pm 0.13$  mag and  $M_V = -18.86 \pm 0.12$  mag.

The photometric distributions of ‘normal’ SNe Ia depends on host galaxy types. The differences between the mean values of  $M_B$  and  $M_V$ , in S-F and passive galaxies, are  $0.30 \pm 0.11$  mag and  $0.28 \pm 0.11$  mag respectively, and are  $0.47 \pm 0.14$  mag and  $0.39 \pm 0.13$  mag in the median values. These two separate distributions lead us to the conclusion that within the ‘normal’ SNe Ia population, intrinsically dimmer SNe Ia are more common from older stellar populations, confirming previous results (e.g. Sullivan et al., 2006).

## 2.8 SNe Ia from young and old stellar populations

SNe Ia are thought to come from both young ( $< 400 \text{ Myr}$ ) and old ( $> 2.4 \text{ Gyr}$ ) stellar populations (Brandt et al., 2010). Traditionally, faster declining SNe Ia are thought to come from old stellar populations, and slower declining SNe Ia from young stellar systems. In section 2.7 it has been stated that there are at least 3 populations of SNe Ia, ‘normal’ SNe from S-F, ‘normal’ SNe from passive galaxies and subluminous SNe. As passive galaxies predominantly consist of old stars, it can be concluded that some of the ‘normal’ SNe Ia must originate from old stellar systems. On the other hand, S-F galaxies consist of both young and old stellar populations. Therefore they must contain

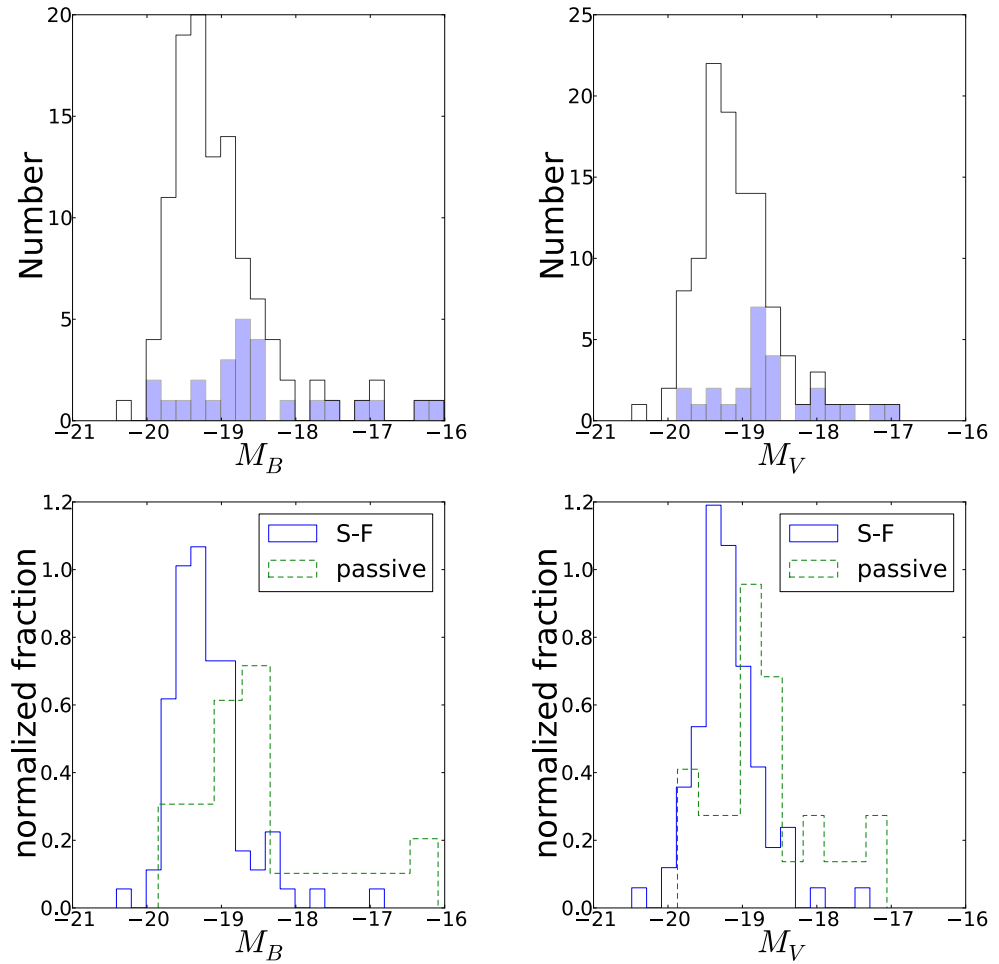


Figure 2.14: The final  $M_B$  and  $M_V$  luminosity distribution plots for the sample used in this work. SNe Ia from passive galaxies with no known extinction have been re-added to this distribution to increase the sample size. *Top:* The left plot is the full  $M_B$  luminosity distribution, the right plot is the full  $M_V$  luminosity distribution. The overlaid blue histograms are the distributions of SNe from passive galaxies. *Bottom:* The left plot is the full  $M_B$  luminosity distribution separated by host galaxy type, and the right plot is the full  $M_V$  distribution separated by host galaxy type.

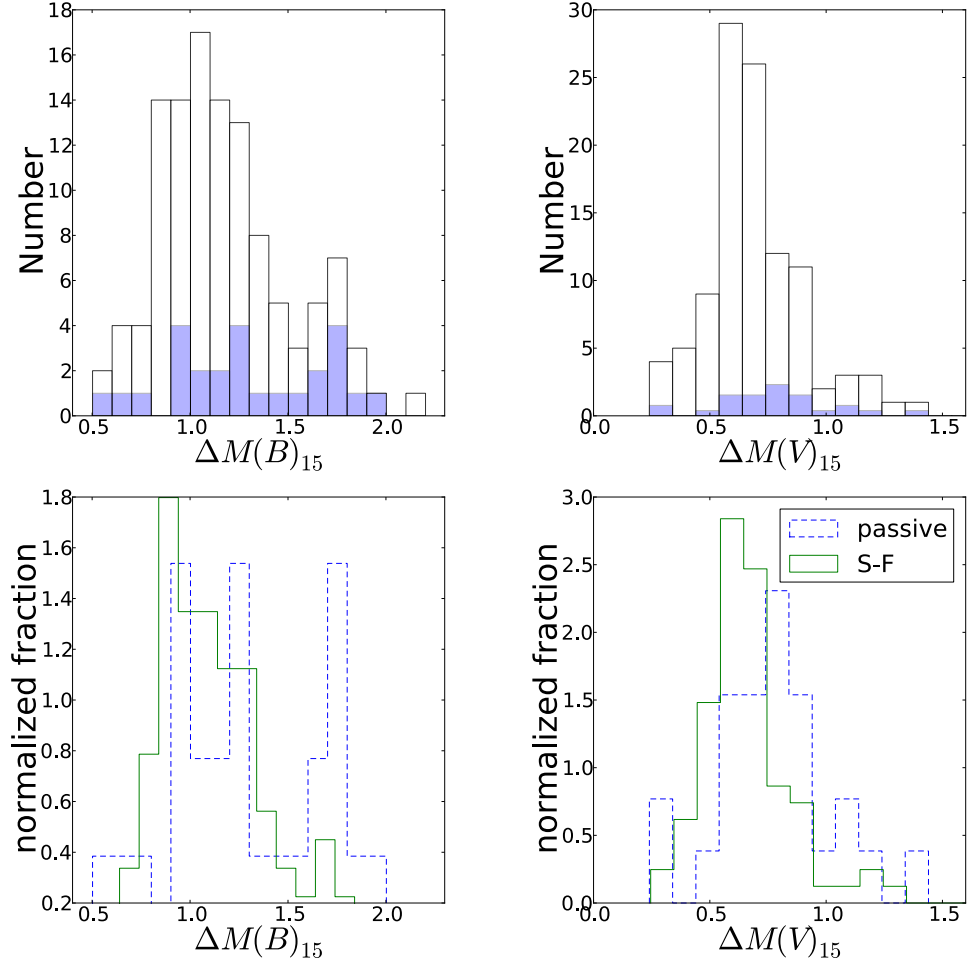


Figure 2.15: The final  $\Delta m_{15}(B)$  and  $\Delta m_{15}(V)$  LD plots for the sample used in this work. SNe Ia from passive galaxies with no known extinction have been re-added to this distribution to increase the sample size. *Top:* The left plot is the full  $\Delta m_{15}(B)$  LD, the right plot is the full  $\Delta M_{15}(V)$  LD. The overlaid blue histograms are the distributions of SNe Ia from passive galaxies. *Bottom:* The left plot is the full  $\Delta m_{15}(B)$  LD separated by host galaxy type, and the right plot is the full  $\Delta m_{15}(V)$  distribution separated by host galaxy type.

SNe from both groups. In this section the fraction of SNe Ia from S-F galaxies which are produced from old stellar populations are quantified. From this the LD of SNe Ia from young stellar populations is produced.

The normalised LDs shown in Figure 2.14 are used to determine the fraction of SNe Ia from young/old stellar populations. This is done by scaling the LD from passive galaxies and subtracting this distribution from SNe from S-F galaxies. It is known that SNe Ia with  $M_B > -18$  mag are mostly from older stellar populations, so only SNe Ia with  $M_B < -18$  mag are examined. Both LDs were divided into 20 bins with similar size (0.2 mag); so that the LDs can be scaled and subtract from one another. The passive LD are scaled to 10%, 20%, 30% and 40% with respect to the S-F LD and subtracted it. The assumption is that the sample of passive SNe Ia is a fair representation of the intrinsic sample, i.e. that SNe from passive environments in S-F galaxies have the same properties as SNe from passive galaxies. The scaled and subtracted S-F LDs are shown in Figure 2.16, which shows that if the passive-like component exceeds 20 per cent of the total the subtraction is unrealistic as more than 50% of the bins are negative. Therefore, in the  $B$ -band a value of  $(15 \pm 10)\%$  is selected as the optimum scaling value to use in the LD subtractions, which suggests that this is the fraction of ‘normal’ SNe Ia in S-F galaxies which are from old stellar populations. The LD when a scaling factor of 15% is used is shown in the bottom right panel in Figure 2.16, where the “passive” component is also shown. In the remaining plots of Figure 2.16, the result of the subtraction are presented, i.e. the “young” component. The LD of SNe Ia from young stellar systems is narrower than that of the whole sample. This effect is seen in both the  $B$  and  $V$  bands. Figure 2.17 shows the  $V$ -band scaled and subtracted LDs. The  $V$ -band results also suggest that  $(15 \pm 10)\%$  of ‘normal’ SNe Ia from S-F galaxies are from old stellar populations. The bottom right panel in Figure 2.17 presents the  $V$ -band LD when a scaling factor of 15% is chosen. The blue bars over-

laid in this plot show the LD of SNe Ia from passive galaxies scaled to 15%. Therefore it is concluded that there are photometrically 4 populations of SNe Ia: ‘normal’ ones from S-F galaxies that come from young stellar systems, ‘normal’ SNe Ia from passive galaxies, which come from an old population, ‘normal’ SNe Ia from S-F galaxies that come from an old population, and subluminal SNe, which are thought to come from old stellar systems.

If it is assumed that the sample is complete, and  $M_B < -18$  mag is used as the cut off between subluminal and normal SNe Ia, the frequency of SNe Ia in our sample can be quantified. Out of the 115 SNe Ia in Figure 2.14, 8 (7%) are subluminal. This leaves 107 SNe Ia, of which 20 are ‘normal’ SNe Ia from passive galaxies (from an old population), and 16 are ‘normal’ SNe Ia from S-F galaxies and which come from an old population. Therefore, 32 (28%) of all SNe Ia are normal and come from an old population, and 75 (65%) of SNe Ia are normal and come from a young stellar population.

## 2.9 Discussion

The aim of this work was to explore the diversity of SN Ia LCs. Therefore, luminosity distributions were built using as few prior assumptions as possible. The analysis does not rely on any empirical LC fitting method, and used distances to the SNe derived from independent methods. The mean values of  $\Delta M_{15}(B/V)$  and  $M_{B/V}$  were used in the analysis as this is a good way to highlight outliers, which make up a small fraction of the overall population. The analysis is presented both before and after applying a correction for host galaxy extinction. Deriving the host galaxy extinction of SNe Ia is a difficult task as it requires resolving the degeneracy between colour and extinction. Although the method used for calculating the host galaxy extinction can resolve the

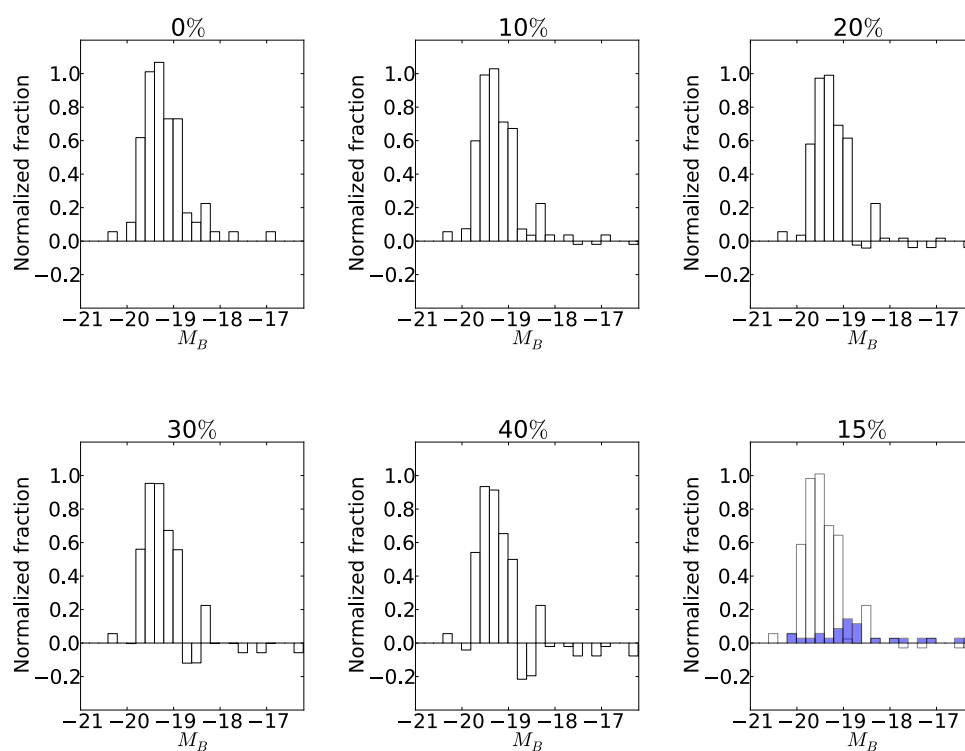


Figure 2.16: The  $B$ -band LD for SNe Ia from passive galaxies normalized, scaled and subtracted from the LD of SNe Ia from S-F galaxies. The factor by which the LD from passive galaxies has been normalized is presented on the top of each plot. The blue bars in the bottom right panel are the LD of SNe Ia from passive galaxies scaled to 15% of those from active galaxies.

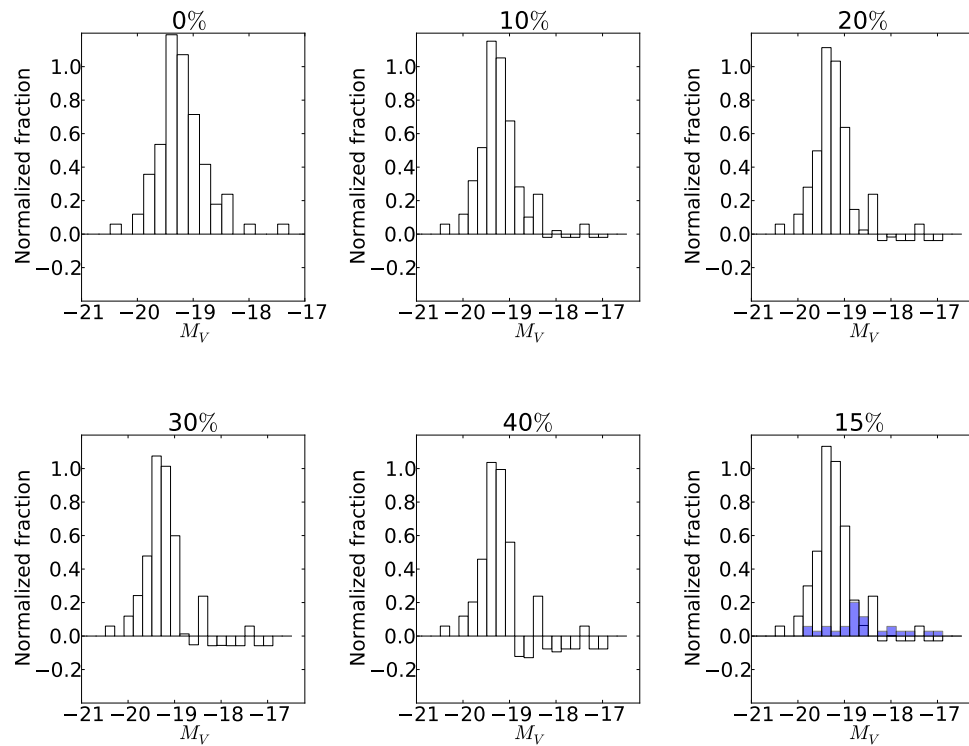


Figure 2.17: The  $V$ -band LD for SNe Ia from passive galaxies normalized, scaled and subtracted from the LD of SNe Ia from S-F galaxies. The factor by which the LD from passive galaxies has been normalized is presented on the top of each plot. The blue bars in the bottom right panel are the LD of SNe Ia from passive galaxies scaled to 15% of those from active galaxies.

colour-extinction degeneracy, it does remove the intrinsically unusual SNe, as there are not enough unreddened spectral matches. Only a subset of the SNe can be corrected for extinction, and some peculiar SNe may not pass this cut. Therefore, the true diversity of SNe Ia may be underrepresented in the corrected sample.

Before correction for host galaxy extinction, our sample includes 165 SNe Ia, 134 of which are from S-F galaxies, 26 from passive galaxies and 5 from host galaxies whose type could not be determined. The average  $M_B$  and  $M_V$  for the sample are  $-18.58 \pm 0.07$  mag and  $-18.72 \pm 0.05$  mag, respectively. The average  $\Delta m_{15}(B)$  and  $\Delta m_{15}(V)$  values for the sample are  $1.14 \pm 0.03$  mag and  $0.68 \pm 0.01$  mag.

A bimodal distribution in  $\Delta m_{15}(B)$  (Figure 2.5) is found, with a lack of transitional SNe. Transitional SNe such as 1986G, 2003hv and iPTF13ebh all have unique properties, and can hold information about potential differences between progenitor channels of sub-luminous and normal SNe Ia. If it is not a selection effect, the lack of transitional SNe could suggest that SNe Ia may come from multiple populations, with different LC properties, which only cross in  $\Delta m_{15}(B)$  at their extremes.

Correcting the data for host galaxy extinction reduces the sample size to 109 SNe Ia, 89 of which are from S-F galaxies, 16 from passive galaxies and 5 from host galaxies whose type could not be determined. The smaller sample is comparable to the larger sample in most relevant parameters. SNe Ia from S-F galaxies suffer from much larger host extinction than those from passive galaxies: 67% of the SNe Ia from S-F galaxies are affected by detectable host galaxy extinction, whose the average value is  $E(B - V) = 0.130 \pm 0.023$  mag. In contrast, only 43% of the SNe Ia from passive galaxies are affected by detectable extinction, with average  $E(B - V) = 0.04 \pm 0.013$  mag. When corrected for host galaxy extinction, the mean  $\bar{M}_B = -19.09 \pm 0.06$  mag and  $\bar{M}_V = -19.10 \pm 0.05$  mag. In the  $B$ -band SNe from passive galaxies were found to be  $0.63 \pm 0.25$  mag less luminous on average than SNe in S-F galaxies.

In the  $V$ -band, the difference is  $0.48 \pm 0.19$  mag.

The WLR is one of the underlying foundations in SN Ia cosmology. It is driven by Ni mass, opacity and ejecta mass. A strong correlation between  $\Delta m_{15}(B)$  and absolute magnitude is found for normal SNe, when only SNe which have a small observed colour term are selected. The WLR in this study is similar to that of Phillips et al. (1999). However, after correcting for host galaxy extinction the spread of properties increases, as shown in Figure 2.13. Furthermore, correcting for reddening leads to the removal of some of the more unusual SNe Ia, and so the true parameter space SNe Ia can fill in the WLR diagram is probably even larger.

K-S tests were run on the sample after correction for extinction. The probability that  $M_B$  values for SNe Ia from passive and S-F galaxies come from the same parent distribution was found to be  $< 0.1\%$ . In the case of  $M_V$  the probability is  $< 0.4\%$ . The likelihood that the  $\Delta m_{15}(B)$  samples come from the same parent distributions is  $\simeq 12\%$ .

SNe Ia in passive galaxies for which the extinction could not be derived were reintroduced to the extinction-corrected sample. As only 43% of the SNe Ia from passive galaxies were affected by detectable host galaxy extinction, and this average extinction was very small, it is assumed that the reintroduced sample has negligible host extinction. When the final LD is separated by host galaxy type, it is found that there are three main populations of SNe Ia: ‘normal’ SNe Ia in S-F galaxies, ‘normal’ SNe Ia in passive galaxies and sub-luminous SNe Ia. Normal SNe Ia in S-F galaxies were found to have a median  $M_B = -19.27 \pm 0.05$  mag and  $M_V = -19.25 \pm 0.06$  mag. Normal ( $M_B < -18$ ) SNe Ia in passive galaxies have median  $M_B = -18.80 \pm 0.13$  mag and  $M_V = -18.86 \pm 0.12$  mag. The difference hints at differences in properties of normal SNe Ia depending on host galaxy type, as shown in Figure 2.14. SNe Ia in S-F galaxies appear to be a much more uniform sample: their distribution is similar to a Gaussian,

whereas SNe Ia in passive galaxies appear to be far more diverse.

In the final section of the analysis the LDs for SNe Ia from passive and S-F galaxies are normalised. In order to quantify the fraction of ‘normal’ SNe Ia which come from old stellar systems in S-F galaxies I scaled the LD of SNe Ia from passive galaxies to represent different fractions of the full S-F LD and subtracted it from the full S-F LD. It is found that  $(15 \pm 10)\%$  of ‘normal’ SNe Ia from S-F galaxies are likely to come from old stellar systems.

In order fully to explore the range in parameter space that SNe Ia can fill one would need to obtain a large sample LF, in both redshift and volume, which is out of the scope of our study. Yasuda & Fukugita (2010) produced a LF, however they removed any peculiar SNe Ia and did not break the colour-reddening degeneracy. Li et al. (2011) produced a volume-limited LF, but did not correct for host galaxy extinction.

As transitional objects appear to be rare, a large sample survey would have to operate continuously for many years to produce a comprehensive LF of SNe Ia. In the years of LSST and large high cadence surveys, along with robotic telescopes on multiple sites (LCOGT), this will be possible. It will then be possible to know the variance of SN Ia properties and place tighter constraints on the progenitor systems.

### 2.9.1 Errors and significance of results.

Through out this chapter the errors on the values of  $M_B$  and  $M_V$  were calculated by propagating the errors on the distance, host galaxy extinction and photometry. This was done using the following equation:

$$errM_{B/V} = \sqrt{errE(B - V)^2 + (errB/V)^2 + errdist^2} \quad (2.3)$$

where  $B/V$  changes depending on which filter band you are using. Where

$err_{dist}^2 \approx (5 \frac{err_d}{d \ln(10)})^2$ , the error on the distance is  $err_d$ , the error on the photometry is  $B$  or  $V$  and the error on the extinction is  $err E(B - V)$ .

In this chapter a number of comparisons are made between SNe Ia from different host galaxy types. Most noticeably that SNe Ia from passive galaxies suffer from significantly less extinction than those from S-F galaxies, and that SNe Ia from S-F and passive galaxies are distinct. Although, it is apparent from the plots that this is true, the significance of these results should be discussed. In astrophysics it is normal to use standard deviation to compare if samples are different. In this chapter I have provided the standard deviations of the samples in the tables. As most of the analysis in the chapter uses the mean, errors next to values in the text are given as the standard errors on the mean. The fact that SNe Ia from S-F galaxies on average suffer from significantly more host galaxy extinction than those from passive galaxies is a three standard errors result. However, this fact is not only based on knowledge from the data in this paper. It is commonly accepted that passive galaxies produce far less dust than S-F galaxies. Therefore it is also a physically sensible result.

Although, some of the results in this chapter are not at the 5 sigma level they are still worth discussing. It is known that SNe Ia are very similar therefore any differences would not be expected to be at this level. Furthermore, two distributions which come from physically different channels but sit in a similar area of parameter space would not have a difference of 3 or 5 sigma but will merit discussion. With this in mind the results from this chapter are interesting and deserve scientific discussion.

## 2.10 Conclusions

This work takes a different approach to normal SN Ia LC analysis. It makes as few assumptions as possible about the SNe, so two SNe Ia with a similar LC shape can have

different properties. This way it is possible to explore the diversity of SNe Ia. SNe Ia are studied by first independently obtaining the distance to each one then calculating its properties,  $M_B$ ,  $\Delta m_{15}(B)$ ,  $M_V$  and  $\Delta m_{15}(V)$ . This allowed the parameter space that SNe Ia can fill to be seen.

Previous results that SNe in passive galaxies tend to decline more rapidly, with an average  $\Delta m_{15}(B) = 1.29 \pm 0.08$  mag, compared to  $\Delta m_{15}(B) = 1.11 \pm 0.03$  mag for SNe in S-F galaxies, are confirmed. This is partly due to the presence of sub-luminous SNe Ia, which are mostly found in older stellar populations. Our method confirms that SNe with small observed  $(B-V)_{B_{\max}} < 0.01$  mag follow the WLR, with some scatter. However, when a larger sample of SNe are corrected for host galaxy extinction the scatter in the WLR increases. It is found that the range in  $M_B$  of normal SNe Ia in the WLR is  $\sim 1.5$  mag. This suggests that (intrinsically) SNe Ia can fill a large parameter space on the WLR. The distribution in  $\Delta m_{15}(B)$  was found to be bimodal, with a lack of transitional SNe. More data from transitional SNe can hold the key to fully understanding the explosion mechanisms of the faint end of the ‘normal’ SNe on the WLR.

There is evidence for differences in parameters for SNe Ia from different host galaxies. SNe Ia in passive galaxies are more likely to be peculiar than those in S-F galaxies. These peculiarities could be central in the debate on different progenitor systems or populations. It is found that there are three main populations of SNe Ia: normal SNe Ia in S-F galaxies, normal SNe Ia in passive galaxies and sub-luminous SNe Ia. Normal ( $M_V < -18$  mag) SNe from passive galaxies have a median  $M_V = -18.86 \pm 0.12$  mag, while those from S-F galaxies have a median  $M_V = -19.25 \pm 0.06$  mag. Finally, it is found that  $(15 \pm 10)\%$  of ‘normal’ SNe Ia from S-F galaxies are likely to come from old stellar systems.

SNe Ia are, although “standardisable”, not an extremely homogeneous group of

objects. There are unusual events which could possibly result from diverse progenitor scenarios. Previous results that sub-luminous SNe favour passive galaxies were confirmed, and the questions about the nature of ‘normal’ SNe Ia from passive galaxies were raised. The key to examining these differences further could be through finding a convincing method to calculate host galaxy extinction on unusual SNe Ia, and with this it will be possible to put tighter constraints on the parameter space SNe Ia can fill.

## 3. How to model a SN

### 3.1 Preface

In astrophysics advances are often made when data have been discovered that seems unusual or intriguing, and theoretical models are produced to explain these observations. These models are often developed and adapted in order to explain the diversity of what is observed. Radiative transfer models simulate the propagation of photons in a medium, and predict the radiation which should occur from the theoretical models. If this prediction matches the observations it is said that the theory is correct. Therefore radiative transfer modelling is a very important part of astrophysics, as it can couple the theory and observations.

This section will give an overview on the basics of radiative transfer and how to model a SN. For a full detailed understanding of the theory and the code used here see Mihalas (1978); Mazzali & Lucy (1993); Lucy (1999); Mazzali (2000); Stehle et al. (2005).

### 3.2 Radiative Transfer Theory

Specific intensity,  $I_\nu(\vec{r}, \hat{n}, t)$ , is one of the fundamental quantities in all problems involving radiation. It is defined at a position  $\vec{r}$  travelling in a direction  $\hat{n}$  at time  $t$ , as the

amount of energy  $dE$ , per unit frequency interval  $d\nu$ , passing through a unit area  $dA$  oriented normal to the beam, into a solid angle  $d\Omega$ , in a time interval between  $t$  and  $t + dt$ :

$$dE = I_\nu(\tilde{r}, \hat{n}, t) dA \cos \theta d\nu d\Omega dt \quad (3.1)$$

The angle between the normal of the reference surface  $dA$  and the direction  $\hat{n}$  is denoted as  $\theta$ .

Spectral features are the imprint matter leaves on a beam of radiation. There are two ways radiation can interact with matter, by absorption or emission. The emission coefficient  $j_\nu$  describes the emission of radiation, whereas the absorption coefficient

$$k_\nu = \kappa_\nu + \sigma_\nu \quad (3.2)$$

gives the loss of radiation due to absorption,  $\kappa_\nu$ , and scattering out of the beam,  $\sigma_\nu$ , and hence is a measure of the overall attenuation of the radiation. The radiative transfer equation for radiation of frequency  $\nu$ , can be obtained by combining the changes in intensity of a radiation beam along the path  $ds$ :

$$\frac{\partial I_\nu(\vec{r}, \hat{n})}{\partial s} = -k_\nu I_\nu + j_\nu \quad (3.3)$$

It can be seen from this equation that the coefficients depend on the frequency  $\nu$  as well as the state of the material, such as the temperature, pressure or composition of the material. If the beam passes through a non-emitting layer ( $j_\nu=0$ ), the intensity after passing through the traversing layer of thickness  $s$  is related to the incident radiation by:

$$I_\nu = I_{\nu,0} e^{-\tau_\nu} \quad (3.4)$$

where  $\tau_v$  is the, dimensionless, optical depth of the transmitting layer:

$$\tau_v = \int_0^s k_v ds \quad (3.5)$$

Using the optical depth the radiation transfer equation can be written as :

$$\frac{\partial I_v(\vec{r}, \hat{n})}{\partial \tau_v} = -I_v + \frac{j_v}{k_v} = -I_v + S_v \quad (3.6)$$

where  $S_v$  is the source function, which is the ratio of emission to absorption coefficients. If an atmosphere is in thermodynamic equilibrium the source function is a universal function of  $\nu$  which depends only on the local temperature  $T$ . In this case it can be described by a blackbody function:

$$S_v = B_v(T) = \frac{2h\nu^3}{c^2} \frac{1}{e^{\frac{h\nu}{kT}} - 1} \quad (3.7)$$

In a purely scattering atmosphere the source function becomes equal to the mean intensity  $J_v$ , which is the intensity integrated over all incident directions.

$$J_v(\vec{r}) = \frac{1}{4\pi} \oint I_v(\vec{r}, \hat{n}) d\Omega \quad (3.8)$$

In this case the source function depends on the distant point where the radiation was originally emitted, and not the local temperature. Even in a purely scattering envelope the equation couples different directions  $\hat{n}$  together and becomes a nonlocal problem. Generally, both  $S_v$  and  $\tau_v$  depend on  $I_v$  in a complicated way, including knowledge about the excitation and ionisation state of the gas. The radiative transfer equation is coupled to the equations of statistical equilibrium (Mihalas, 1978).

### 3.3 Radiative Transfer in SN ejecta

This section will describe the basics of radiative transfer in SN ejecta, and one way to numerically solve the problem using a Monte Carlo (MC) approach. For the exact details of the theory and method of modelling SN one should read Mihalas (1978); Mazzali & Lucy (1993); Lucy (1999); Mazzali (2000); Stehle et al. (2005).

At early times a SN is in the ‘photospheric’ phase. This is because the ejecta is dense enough to emit continuum radiation within the ejecta itself. The point at which the continuum optical depth reaches unity gives rise to an effective photosphere. The continuum radiation must traverse the fraction of the envelope above the photosphere, and interact with the expanding gas. This is where the early time SN spectra are formed. This justifies using the Sucher-Schwarzschild approximation, and makes it sensible to only calculate the radiative transfer above a predefined photosphere, which in the case of a SN can be a black body. (At early times a SNe Ia’s photosphere can be idealised as an infinitely thin layer, above which no continuum is formed. In the case of SNe Ia, continuum opacities are small compared to the effects of line blanketing. Therefore, the photosphere we talk about with respect to SNe Ia is actually a line dominated pseudo photosphere.)

A SN can be thought of as a spherical homologous expansion, where the radius and velocity of the ejecta is proportional to the expansion velocity of the ejecta as a fixed time from explosion:  $r = v \times t_{exp}$ , where  $r$  is the radius,  $v$  is the photospheric velocity and  $t_{exp}$  is the time from explosion. This also means the density at a co-moving point scales with  $t_{exp}^3$ . A density structure is required to carry out a radiative transfer calculation. The density of a SNe Ia is normally very steep, and for the purpose of this work for now it can be assumed that the W7 density profile (Nomoto et al., 1984) was used, unless it is stated otherwise. This template density profile, which can be expressed as a function of velocity  $\rho(v)$ , can be rescaled to different epochs, because

of the homologous expansion. Once the density has been determined the ejecta can be split into 10-20 shells in which the radiation transport calculations can take place.

Due to the large velocity gradient in a SN ejecta a single photon can interact with many spectral lines, due to the progressive redshift of the photons in the co-moving frame, as the photon scatters in the differentially expanding envelope. This Doppler overlapping makes a connection between different parts of the SN envelope. In the UV this line overlapping is so large that it constitutes a source of continuum opacity known as line blocking.

Furthermore, due to the large velocity gradient in SNe using the Sobolev approximation is justified for SN modelling. The basic idea of the Sobolev approximation is that a photon emitted from a photosphere only interacts with a line in a small region of the atmosphere where the photon is Doppler shifted (due to the expansion of the photosphere) into resonance with the line. Since the source function can be assumed to be constant over this small resonance region, the solution of the radiative transfer equation is greatly simplified (Kasen et al., 2002). This means that a photon with a specific radial position with a specific frequency can only be absorbed by a single line with which it is in resonance. This is a good approximation as the resonance region of a line is so small compared to the length scale over which the physical properties change, due to the large velocities. Therefore a photon packet with rest frequency  $\nu$  will interact with lines of progressively lower frequency, regardless of its direction of motion, as  $v \propto r$ .

### 3.4 MC code

In this section the MC code will be discussed. Using a MC approach to SN radiative transfer has the advantages that it is quick and robust and still reasonably accurate.

Due to the speed of the code it is good for detailed studies of many SN.

One of the assumptions which is made in this code is that the conditions remain constant during one calculation. The MC code only uses the momentary luminosity of the SN, which is a result of time-dependent photon diffusion, and does not attempt to determine the photon diffusion time and photospheric properties. This is valid assumption as the diffusion time through the reversing layer is small.

With a given density, split into shells, the MC procedure can begin. First the temperature must be known before occupation number calculations can be performed. In the case of a SN, redshifts and backscattering (photon packets re-entering the photosphere and increasing the temperature) cause the radiation to change with radius. To take this into account a simplified radiation equilibrium equation is adopted.

The mean energy of a photon in a black body radiation field is given by:

$$\bar{x} = \frac{h\bar{\nu}}{kT} \quad (3.9)$$

with  $\bar{x}=3.832$ . The radiation temperature is computed after the frequency moment is obtained from:

$$\bar{\nu} = \frac{\int_0^\infty \nu J_\nu d\nu}{\int_0^\infty J_\nu d\nu} \quad (3.10)$$

The temperature is obtained by iterating between the occupation numbers and the radiation field obtained, using the most recent value of  $T_R$  (radiation temperature) until convergence is obtained. The electron temperature is defined to be

$$T_e(r) = 0.9T_R(r), \quad (3.11)$$

to simulate approximately the radiative control of the electron temperature. This is only a crude assumption and the real temperature structure depends on the ionisation regime. A detailed analysis performed in NLTE and taking into account the physical

processes coupling the kinetic temperature to the radiation field may be more accurate. The iteration procedure is started with  $T_R(r) = T_{eff}$ , where the effective temperature  $T_{eff}$  is given by the photospheric radius  $R_{ph}$  and the luminosity is given by

$$L = 4\pi R_{ph}^2 \sigma T_{eff}^4 \quad (3.12)$$

The effect of viewing a finite photosphere and of the progressive degradation of the radiation upon its interaction with the envelope matter is such that  $J(r)$  falls below  $B(T_R(r))$ . This allows us to compute an equivalent dilution factor (Mihalas, 1978):

$$J = WB(T_{eff}) = W \frac{\sigma}{\pi} T_R^4. \quad (3.13)$$

The MC code adopts a purely scattering envelope in terms of interaction with electrons, and line absorptions are treated in a photon branching scheme. If an electron is in an excited state  $u$  all downward transitions from  $u \rightarrow l$  are considered. This is very important for modelling the UV part of a SN spectrum, as most of the flux here is made via reverse fluorescence. Conversely it is equally as important for making the optical part of the spectrum, as most of the flux here is made via fluorescence. This will be discussed further in section 5.6.1. In the code only line transitions and electron scattering occurs as the Sucher-Schwarzschild approximation is used, and no continuum formation occurs above the photosphere.

The attenuation of a beam of radiation in the envelope over a distance  $s$  is given by

$$I_v(s) = I_v(0) \exp[-(\tau_e + \tau_L)] \quad (3.14)$$

where  $\tau_e$  is the integrated electron scattering optical depth and  $\tau_L$  is the integrated line optical depth.

As  $v \propto r$ ,  $dv/dr \equiv v/r$ . Therefore, the optical depth of a single line is given by:

$$\tau_l = \kappa \rho \lambda \frac{r}{v}, \quad (3.15)$$

where

$$\kappa \rho = \frac{\pi e^2}{m_e c} n_l f_{li} \quad (3.16)$$

and  $e$  is the electron charge,  $m_e$  is the electron rest mass,  $n_l$  is the population of the lower level of the line transition, and  $f_{lu}$  is the oscillator strength of the transition.

### 3.5 Ionization and excitation

The ionization and excitation of the envelope of gas is required to compute the line optical depths. Usually this would mean solving simultaneously the coupled equations of statistical equilibrium and radiative transfer. However, for none minor species this is computationally expensive and would require a large number of photoionization rates and an iteration process between radiation field and occupation number.<sup>1</sup> The code used for this project uses a modified nebular approximation to treat ionization and excitation. This nebular approximation has the advantage that it can be computed at almost LTE cost. The basic idea of this is to fit the actual radiation field,  $J_\nu$ , with a function including two fit parameters  $W$  (equivalent dilution factor) and  $T_R$  (radiation temperature). A subset of levels for each atom is then considered, either metastable states which are connected to the ground state (via higher lying transitions), or normal states which are connected to the ground state or meta stable state via a single permitted transition. Approximating the system of the ground state 1 and a normal excited state

---

<sup>1</sup> The MC code can do this for H and He, however these are not needed in this project and will not be discussed further.

as a two level atom, and neglecting stimulated emission as well as collisional processes, the occupation number for normal excited states  $u$  can be obtained:

$$\frac{n_u}{n_1} = W \times \frac{g_u}{g_1} e^{-hv_{1u}/k_B T_R} \quad (3.17)$$

and for the metastable states  $m$  one calculates, considering an appropriate three level atom:

$$\frac{n_m}{n_1} = W \times \frac{g_m}{g_1} e^{-hv_{1m}/k_B T_R} \quad (3.18)$$

which equals an LTE excitation pattern at  $T_R$ .

Ionisation can be calculated by an equation similar to the Saha-Boltzman equation. A basic form of this can be derived assuming a diluted blackbody radiation field and a negligible influence of collisions. The nebular ionisation approximation which is used in this version of the code is:

$$\frac{n_e n_{1,j+1}}{n_{1,j}} = \frac{2g_{1,j+1}}{g_{1,j}} \times W \zeta \left( \delta + W \left( \frac{1}{\zeta} - 1 \right) \right) \times \sqrt{\frac{T_e}{T_R}} \times \left( \frac{2\pi m k T_R}{h^2} \right)^{3/2} \times e^{-\frac{hv_{T(1j)}}{k_B T_R}} \quad (3.19)$$

The factor  $\zeta \left( \delta + W \left( \frac{1}{\zeta} - 1 \right) \right)$  has been added here compared to Mihalas (1978) in order to account for ionisation from the recombination to excited states, and for a modified field at UV wavelengths. For further details see Mazzali et al. (1993).

### 3.6 Numerical technique

As the basic physics in the code has been described above, the numerical technique and code itself will now be explained. The code requires as input, the time from explosion  $t_{exp}$ , the photospheric velocity  $v_{ph}$ , the bolometric (emergent) luminosity  $L$ , as well as

the chemical composition of the ejecta. The code divides the SN ejecta into a number of shells, between 15-20, whose thickness increases as a function of radius.

The code makes use of an extensive line list of 500 000 lines. From this line list a set of lines are selected during the first temperature iteration. The lines selected depend on the abundances and the temperature in the SN ejecta. After the main lines are determined the temperature structure can be calculated, as described above. This is done by running through a series of MC experiments, until convergence to the appropriate radiative equilibrium is reached. It should be noted that both  $T_B$  and  $T_R(r)$  are calculated with this method. After interactions with lines and electrons, photons can re-enter the photosphere, in a process called back warming. This can cause the  $T_B$  to be higher than  $T_{eff}$ , as  $T_B$  has to be large enough to match the required input luminosity. Furthermore, it leads to an increased temperature gradient immediately above the photosphere.

### 3.6.1 Photon branching

An important part of the MC code is the inclusion of photon branching. Photon branching allows photon packet emitted through downward transitions to make big jumps in wavelength. All permitted decays are allowed and given a weighting, the most likely of these decays is then selected. This means that photons do not have to be re-emitted at the same frequency that they are absorbed, meaning they can make large jumps. As lines are the main source of opacity in a SN envelope, they can effectively block regions of the spectrum. This is known as line blocking. Line blocking is especially strong in the UV part of a SN spectra, where there are so many lines at various velocities they act as a source of opacity and no photons emitted from the photosphere can escape. Photons can only escape if they reach a line free region. The next available window is always the next one to the red, in the co-moving frequency of the photon. To reach

this window the photon has to undergo many scattering events, and has a high probability of reentering the photosphere. However, with branching the photon can make big jumps in frequency during one single event. The reprocessing of flux from the UV to the red, and then the escape of the photons, makes the optical part of a SN spectrum. It should also be noted that to properly model the UV part of a SN spectrum photon branching is required. This is because photon branching allows reverse fluorescence to take place, where blue and UV photons are generated by downward decays to low lying levels in the outer part of the envelope. This means the UV photons are produced far above the photosphere, and therefore have less ejecta to propagate through before they escape the envelope. UV photons at the photosphere face too large an optical depth to be able to escape without first being redshifted to optical wavelengths.

### 3.6.2 Random walk

Now that the inputs are known, the line list is built and the temperature is determined, the real MC calculation can take place. The random walk of a number of photon packets are followed through the SN envelope. The photospheric luminosity is divided evenly between  $N$  packets, so that each packet has the same initial energy  $\epsilon_0 = L/N$ , and each packet contains a number of photons  $n_v$  where  $\epsilon = n_v h\nu$ . Using packets with the same energy is very useful in a MC simulation, as it leads to good sampling in the wavelength regime where most of the energy is. It is also very useful in photon branching where large jumps in frequency can happen but the energy of the packet can be conserved, as the number of photons in each packet can change.

The frequency of each packet in each bin is assigned randomly from a number generator, and the direction of emission is also assigned randomly as a direction cosine. The event histories of the packets are then followed as they propagate through a random walk process in the ejecta. Photon packets have two fates: they either re-enter the

photosphere or escape the envelope, and either way they can undergo line interaction or electron scattering.

The main part of the code determines what happens next: does the packet encounter a line interaction or a scattering event before it crosses either the inner or outer border of the shell where the physical conditions change. The direction of ejection must be used to calculate the distance the packet must travel to reach the outer edge of the first shell. A random optical depth is selected  $\tau_R = 1 - \ln(z)$ , where  $z$  is a random number between 0 and 1. Two possible events can occur, electron scattering and line interaction. Electron scattering occurs with a probability that is linear with radius, since it is assumed that the electron density is constant in each shell, whereas line opacity occurs at a specific point in a packet's trajectory, where the frequency of the packet is the same as the resonance frequency of a spectral line. A packet emitted from the photosphere can only interact with lines which are at a longer wavelength than itself, due to the expanding nature of the ejecta. The energy packet encounters an electron optical depth  $\tau_e$  during its flight. The path length  $s_e$  the photon can travel freely before  $\tau_e$  becomes equal to  $\tau_R$  is calculated using  $\tau_e = \sigma_T n_e(i) s_e$  where  $n_e(i)$  is the electron density of the  $i$ th shell, and  $\sigma_T$  is the Thomson electron cross section. If  $s_e$  is less than the distance needed to exit the shell, the packet may undergo electron scattering in the next shell. After this the distance of the line encounter  $s_l$  needs to be compared to  $s_e$ . This can be calculated at the packet's co-moving frequency at the resonance point  $\nu' = \nu[1 - \mu(\nu/c)]$ , using the Doppler formula with  $\nu \propto r$ .

Finally  $s_e$  and  $s_l$  are compared to the distance of the edge of the shell  $s_{sh}$ , and the smallest of these values decides what happens next. If the packet is closest to the edge of the shell, it enters the next shell with the new physical conditions and a new optical depth calculation must begin. If electron scattering occurs next a new random direction is assigned to the packet and the MC experiment starts again. If the photon

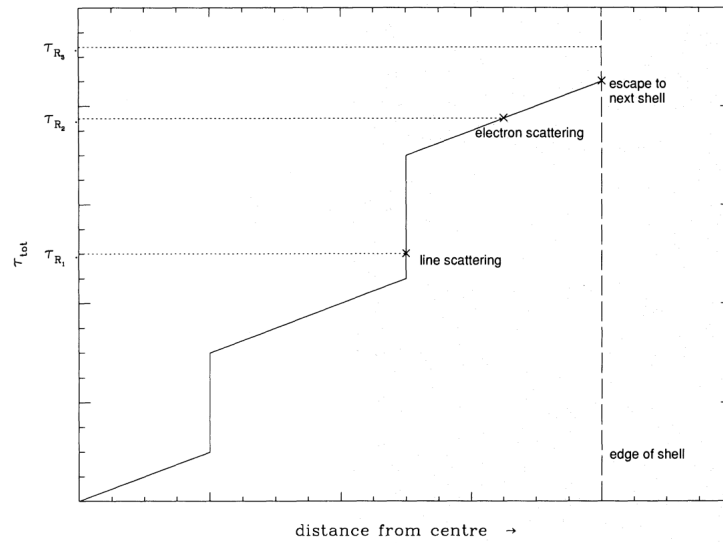


Figure 3.1: Photon packets encounter line events or electron scattering during their random walk within each shell (Mazzali, 2000).

encounters a line event, the downwards transition has to be chosen. The probability of spontaneous decay to a particular level  $i$  is then:

$$p_{ji} = \frac{A_{ji}\beta_{ji}hv_{ji}}{\sum_i A_{ji}\beta_{ji}hv_{ji}} \quad (3.20)$$

The factor  $hv_{ji}$  is introduced as energy packets are used in the MC experiment. Figure 3.1 shows how photon packets react when they encounter a line or scattering event, before they escape the shell.

Typically about 50 000 photon packets are used in the MC calculation. Once the propagation of each packet is followed through the ejecta the final spectrum must be formed. The spectrum is formed by calculating the formal integral for the emergent intensity. A full explanation of this can be found in Lucy (1999).

## 3.7 Modelling procedure

The aim of producing synthetic models of SNe is to compare them with observations. The normal process of modelling a time series of spectra involves producing synthetic spectra starting with the earliest epoch. This is done by setting the distance and extinction to the SN, then determining the bolometric luminosity of the ejecta and the photospheric velocity. A typical abundance distribution is assumed and a synthetic spectrum of the first epoch is produced. Usually 2 or 3 synthetic shells are placed above the photosphere of the first observed spectrum, in order to produce a stratified abundance distribution at higher velocities, and to avoid wrong elements being seen at high velocities in the synthetic spectra. The abundances above the photosphere are varied to produce the best fit to the observed spectrum. Once an acceptable fit is obtained the next spectrum is modelled using the same procedure, and only the abundances inside the previous photosphere are modified. Abundances in the outer layers can affect the synthetic spectra at later epochs. If this is the case iteration is required on the abundances of the elements in the outer layers. Once the modelling procedure is complete, physical properties about the SN ejecta can be obtained, including the abundance distribution in velocity space. This technique is known as ‘abundance tomography’, it was first published in Stehle et al. (2005). Abundances given in this work have an error of  $\pm 25\%$ , and photospheric velocities have an error of  $\pm 15\%$ . A detail analysis of errors using the ‘abundance tomography’ method was carried out in Mazzali et al. (2008). The error on the  $^{56}\text{Ni}$  mass is  $\pm 10\%$ , as it is constrained through multiple methods.

### 3.7.1 Constraining the abundances

In the abundance tomography process all of the main elemental abundances (Ca, Mg, Si, S, C, Ti, Cr, Fe, Ni) are constrained by the data. The default abundance is oxygen.

If all of the other features in the spectra are matched, in both depth and velocity, but the total abundance in the shell is not unity the remaining mass will be put as oxygen. Therefore, in some cases if the oxygen feature is fit poorly, (i.e. it is too strong) it could be an indication that there is too much mass above the photosphere. However, this is not a problem found in this thesis.

One assumption in the models is that there is smooth mixing of elements throughout the ejecta. For example if there are two synthetic spectra at  $12000 \text{ km s}^{-1}$  and  $8000 \text{ km s}^{-1}$ , and if at  $12000 \text{ km s}^{-1}$  the Si abundance is 10% and at  $8000 \text{ km s}^{-1}$  the Si 30%, the assumption is made that the Si abundance at  $10000 \text{ km s}^{-1}$  will be 20%. This is a fair assumption as most explosion models show elements smoothly mixed throughout the ejecta. The only times there will be a significant jump in abundance values in the abundance tomography models is when the synthetic spectra become significantly worse if the smooth mixing assumption is assumed.

## 4. SN 2014J

### 4.1 Preface

One way to understand the link between subluminescent SNe Ia and normal SNe Ia is through radiative transfer modelling. Therefore, the second project in this thesis was to observe and model SN 2014J. This SN is a close and interesting object, and was used as a good test for modelling a normal SN Ia. This section presents spectroscopic and photometric observations and abundance tomography modelling of this SN. Work from this section has been published in Ashall et al. (2014). All of the work in this chapter was carried out by myself, except for the observations and reduction of the INT spectra which were performed by Phil James and Sue Percival respectively. Furthermore, the SIFTO fitting in the work was carried out by Kate Magure, and the study into the effect of  $R_v$  on  $\Delta m_{15}(B)$  was carried out by Mark Phillips.

### 4.2 SN 2014J

SN 2014J was discovered on 2014/01/21.810 (Fossey et al., 2014). It is located in M82, which makes it the closest SN Ia in at least the last 28 years and possibly the last 410 years, depending on distance estimates. SN 2014J is a spectroscopically normal SN Ia, with high-velocity features. There have been many studies into SN 2014J which

confirm it as a normal SN Ia (Ashall et al., 2014; Goobar et al., 2014; Amanullah et al., 2014; Kelly et al., 2014; Marion et al., 2015; Foley et al., 2014; Brown et al., 2015). Photometric and spectroscopic observations of SN 2014J were obtained, and abundance stratification models were produced. As technology has dramatically improved in recent times, this SN gives us a unique opportunity to intensely observe, analyse and model a SN Ia with modern techniques. SN 2014J is located at RA=9:55:42 Dec=69:40:26.0 (J2000), and is in M82 which is at a distance of  $3.77 \pm 0.66$  Mpc. This value was obtained from the mean distance from NED, from 2 methods, PNLF (Planetary Nebula Luminosity Function) and TRGB (Tip of the Red Giant Branch). However, it should be noted that Foley et al. (2014) derive a distance of 3.3 Mpc. M82 is known for having a large amount of star formation; hence it has a large amount of dust (Hutton et al., 2014). Because of this, SN 2014J is highly and unusually reddened. It does not follow the average galactic reddening law of  $R_V=3.1$ . Detailed investigations into the host galaxy extinction were produced by Amanullah et al. (2014) and Foley et al. (2014). With our modelling approach, the published extinction values are optimised by deciding which values produce the best-fits of SN 2014J from the spectra.

### 4.3 Observations

Photometric and spectroscopic observations of SN 2014J were carried out with the Liverpool Telescope (LT). The LT is a 2.0 metre fully robotic telescope located at Observatorio del Roque de los Muchachos (ORM) on La Palma. 10 spectra were obtained using FRODOSpec, a multipurpose integral-field unit spectrograph, at -8 d to +10 d relative to  $B$ -band maximum, see table 4.1. FRODOSpec consists of blue and red arms which cover 3900-5700 Å and 5800-9400 Å respectively. The FRODOSpec pipelines were used to reduce the spectra, the first one L1 performs bias subtraction,

overscan trimming and CCD flat fielding, and the second, L2, includes production of sky subtracted row stacked spectra which is specific to FRODOSpec (Barnsley et al., 2012). No host galaxy subtraction was performed with the spectra, as no images were available. However, the sky subtraction routine in the FRODOSpec pipeline removes most of the flux from M82, meaning that any flux which has not been subtracted should be negligible.

Photometric observations were obtained using IO:O, an optical imaging camera which has a field of view (FOV) of 10 arcmin<sup>2</sup>. Three filters were used to obtain the light curves of the SN, SDSS  $g'r'i'$ . The IO:O pipeline, which consists of bias subtraction, trimming of the overscan regions and flat fielding, carried out the data reduction.

There are also two spectra at the 2.5m Isaac Newton Telescope (INT), located at ORM on La Palma. The Intermediate Dispersion Spectrograph (IDS) is a long-slit spectrograph on the INT. The IDS was used with a set up of R1200Y grating and RED+2 camera.

## 4.4 Extinction

The foreground Galactic extinction of SN 2014J is  $E(B - V)=0.05$  mag ( $R_V=3.1$ ) (Amanullah et al., 2014; Foley et al., 2014). Due to the large amount of star formation and therefore dust in M82 SN 2014J is highly and unusually reddened; it does not follow the average Galactic extinction law of  $R_v=3.1$ . Detailed investigations into the extinction of SN 2014J have been carried out by Foley et al. (2014) and Amanullah et al. (2014). Foley et al. (2014) present HST spectroscopic and photometric data, and attempt to derive the correct extinction of SN 2014J. Their preferred model is one with variable extinction where  $E(B - V)$  changes by 0.4 mag one month after  $B$ -band

Table 4.1: Log of spectroscopic observations of SN 2014J.

Epoch	MJD <sup>a</sup>	Phase <sup>b</sup> (d)	Exp time (s)	Instrument
2014-01-26	56684.12	-8	500	FRODOSpec
2014-01-27	56685.12	-7	500	FRODOSpec
2014-02-03	56692.01	+0	600	FRODOSpec
2014-02-04	56692.90	+1	600	FRODOSpec
2014-02-04	56693.13	+1	3×120	INT
2014-02-05	56693.89	+2	600	FRODOSpec
2014-02-06	56694.96	+3	600	FRODOSpec
2014-02-07	56695.89	+4	500	FRODOSpec
2014-02-07	56696.13	+4	3×120	INT
2014-02-08	56696.92	+5	500	FRODOSpec
2014-02-09	56697.97	+6	500	FRODOSpec
2014-02-11	56699.88	+8	500	FRODOSpec
2014-02-13	56701.877	+10	500	FRODOSpec

<sup>a</sup> Observation in MJD date

<sup>b</sup> Relative to B-band maximum

maximum, and was determined by minimising the residuals between the spectra of SN 2011fe and SN 2014J. This approach uses a two-component circumstellar scattering and dust reddening model. They also analyse the extinction using other methods such as the colour excess. The values obtained for the colour excess using the CCM law (Cardelli et al., 1989) by Foley et al. (2014) were  $E(B - V)=1.24\pm 0.1$  mag and  $R_V=1.44\pm 0.06$ .

Amanullah et al. (2014) use HST photometric data to explore the extinction of SN 2014J by comparing it to SN 2011fe. They use a variety of extinction laws, and state that the best values are found using a power law extinction, with an  $R_V=1.4\pm 0.1$  and  $p = -2.1 \pm 0.1$ . Using the FTZ reddening law (Fitzpatrick & Massa, 1999) between -5 to +35 d relative to B-band maximum Amanullah et al. (2014) found an  $E(B - V)=1.29\pm 0.02$  mag and an  $R_V$  of  $1.3\pm 0.1$  with a  $\chi^2/dof = 3.3$ . It should be noted that the FTZ and CCM law are the same over the wavelengths used in this study.

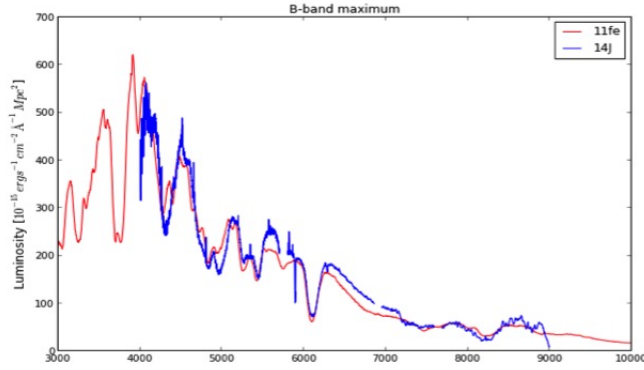


Figure 4.1: Maximum light spectra of 2014J and SN 2011fe.

However, the comparison between SN 2014J and SN 2011fe may not be the best way to determine the extinction law as they have different values of  $\Delta m_{15}(B)$ . SN 2011fe has a  $\Delta m_{15}(B)$  as high as 1.21 mag whereas SN 2014J has a value of 0.95 mag, or  $1.08 \pm 0.03$  mag when corrected for extinction. One can force SN 2014J to have the same LC shape as SN 2014J. However, one is then in a circular argument where extinction values are adopted to produce the appropriate decline rate. Furthermore, when the B-band maximum spectra are compared, Fig 4.1, it is found that there is a difference in the Fe  $\sim 4800 \text{ \AA}$  feature, which demonstrates a higher intrinsic temperature and different ionisation.

Due to the high quality of data used in Amanullah et al. (2014) and Foley et al. (2014) to calculate the extinction towards SN 2014J, no host galaxy extinction is derived in this work. The values used in this analysis are  $E(B - V) = 1.2$  with  $R_V = 1.38$ . These are adopted by optimising the published extinction values, colour excess and FTZ law from, which produce the modelled best-fits of SN 2014J from the spectra. It should be noted that the attenuation of the flux in  $B$  and  $V$  is similar with the values of Amanullah et al. (2014) and Foley et al. (2014).

## 4.5 Photometry

SDSS  $g'r'i'$  light curves were produced, see Figure 4.2. Photometric reduction was carried out using the IRAF<sup>1</sup> package DAOPHOT. Instrumental magnitudes of SN 2014J and stars within the field were obtained. In order to produce the calibrated magnitudes of the supernova, the colour terms and zero points were required. For the  $g'r'i'$  filters, the colour terms were obtained by using the standard star images, taken on the same night as the observations, and comparing their instrumental magnitudes to the APASS catalogue magnitudes<sup>2</sup>. IO:O typically requires an exposure time of over 10 s for good photometry, due to the amount of time it takes for the shutter to open and close. The typical exposure time in the photometric images was 2 s. Therefore stars at the edge of the FOV will be exposed for a shorter period of time than ones in the centre of the field. To overcome this, the zero points were calculated using a single star, RA=9:55:35 Dec=69:38:55 (J2000), close to SN 2014J. This star is a G type star and shows no sign of being a variable star. This star was observed four times over the course of a month for the APASS catalogue. It was also observed for the Tycho-2 catalogue (Høg et al., 2000). The magnitudes obtained with the Tycho-2 and APASS catalogues were within 0.03 mag in the  $B$  band and 0.02' mag in the  $V$  band. This is less than the errors on the photometry. The main source of error in the photometry was calculating the zero points; if the calibration star was saturated the magnitude was ignored. As there are not pre-explosion images of M82 using the LT, the host galaxy has not been subtracted from the photometry. To calculate how much this host galaxy flux affects the photometry the SDSS images of M82 were used. Aperture photometry was carried out, using the same aperture size as the LT images, on the location of the SN pre-

---

<sup>1</sup> IRAF is distributed by the National Optical Astronomy Observatories, which are operated by the Association of Universities for Research in Astronomy, Inc., under cooperative agreement with the National Science Foundation.

<sup>2</sup> <http://www.aavso.org/apass>

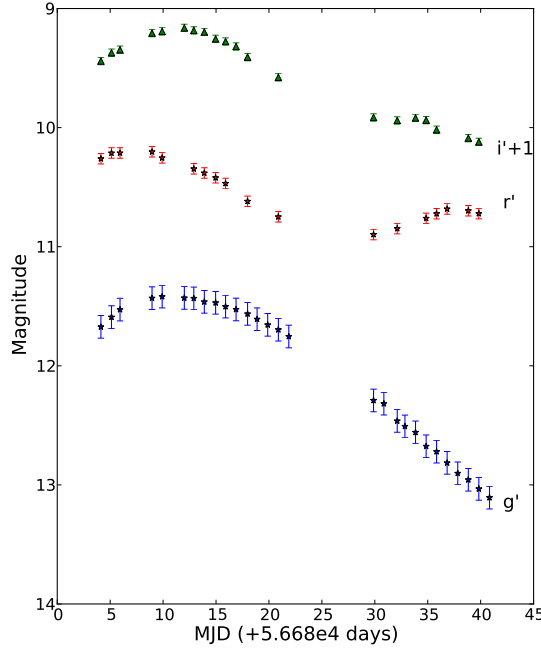


Figure 4.2: Aperture photometry light curves, produced using LT data. SDSS  $g'r'i'$  light curves are presented. The errors on the photometry appear to be constant; this is due to the catalogue error on the zero point star dominating.

explosion and a standard star in the FOV. From this I found that the highest value the photometry can deviate by, owing to the missing host galaxy subtraction, is 8% in the  $i'$ -band, 5% in the  $r'$ -band and 5% in the  $g'$ -band.

SN 2014J was observed at an almost daily cadence from MJD 56684.12 to 56720.83.  $g'r'i'$  light curves were produced (Figure 4.2). There was a gap in observations between 13<sup>th</sup> Feb 2014 and 21<sup>st</sup> Feb 2014, due to poor weather conditions on La Palma.  $g'$ -band maximum occurred on 03-Feb, which is consistent with the maximum in the  $B$  passbands (Tsvetkov et al., 2014). It was found that  $g'$ -band maximum was  $11.42 \pm 0.09$  mag,  $r'$ -band maximum was  $10.16 \pm 0.03$  mag and  $i'$ -band maximum was  $10.20 \pm 0.05$  mag. The distance modulus used for M82 was taken from NED,  $\mu=27.86$  mag. Therefore, at maximum, SN 2014J had an absolute  $g'$ -band magnitude of  $-16.44$  mag, an

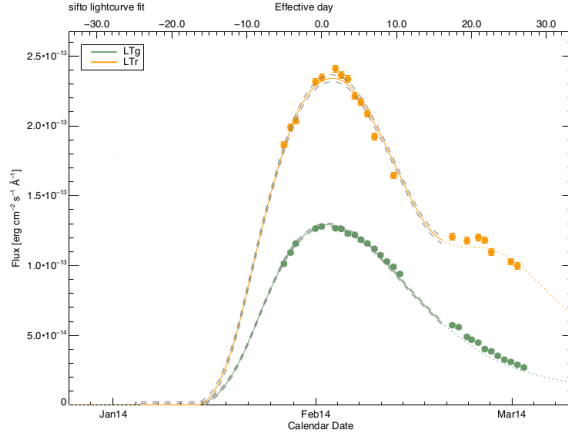


Figure 4.3: SIFTO SN 2014J light curve fits

$r'$ -band magnitude of  $-17.68$  mag and an  $i'$ -band magnitude of  $-17.66$  mag, before correction for extinction.

Foley et al. (2014) and Marion et al. (2015) have published photometric and spectroscopic observations of SN 2014J. They report  $\Delta m_{15}(B)$  to be 1.01 and 1.08 mag respectively when corrected for host galaxy extinction, and Foley et al. (2014) report  $1.95 \pm 0.02$  mag when not corrected for host galaxy extinction. We analysed the LT SDSS  $g'$  and  $r'$ -band photometry with the SiFTO (Conley et al., 2008) light curve fitter to obtain the stretch,  $V$ -band maximum and  $t_{Bmax}$ , see Figure 4.3. Using the  $g'$  and  $r'$  bands we obtained a stretch of  $1.083 \pm 0.06$ , which corresponds to a  $\Delta m_{15}(B) = 0.88 \pm 0.08$  using the relation from Conley et al. (2008). However using only the  $r'$  band light curve produces a stretch of  $1.035 \pm 0.08$  and therefore a  $\Delta m_{15}(B)$  of  $0.95 \pm 0.12$ . When corrected for host galaxy extinction,  $E(B - V) = 1.2$  ( $R_V = 1.38$ ), using the relation from

Phillips et al. (1999), the  $B$ -band decline rate is found to be  $1.00 \pm 0.06$  or  $1.07 \pm 0.08$  for  $g'$  and  $r'$  bands and  $r'$  band respectively. These decline rates are consistent with those of Foley et al. (2014). However the correction of Phillips et al. (1999) for obtaining “reddening-free”  $\Delta m_{15}$  values from the observed values was derived assuming

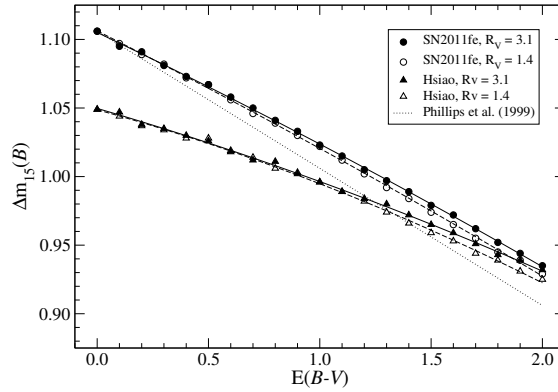


Figure 4.4: Dependence of  $\Delta m(B)_{15}$  on  $E(B - V)$  for different values of  $R_V$ , using SN 2011fe spectrophotometry and the Hsiao template.

an  $R_V = 3.1$ . To check the sensitivity of this correction to  $R_V$ , we carried out our own calculation of the effect of dust reddening on  $\Delta m_{15}(B)$  for  $R_V=3.1$  and  $R_V=1.4$  using the published optical spectrophotometry of SN 2011fe (Pereira et al., 2013) and the Hsiao SN Ia spectral template (Hsiao et al., 2007). The spectra were reddened for values of  $E(B - V)=0.0-2.0$  using the IRAF DEREDDEN task, which implements the CCM law. Synthetic magnitudes were calculated using the Bessell (1990)  $B$  pass-band, and the  $B$ -band decline rate was measured for each value of  $E(B - V)$ . Figure 4.4 shows the results, including a comparison with the approximate relation given by Phillips et al. (1999). As is seen, the effect on  $\Delta m_{15}(B)$  of changing the value of  $R_V$  from 3.1 to 1.4 is small. For  $E(B - V)=1.2$  and  $R_V=1.38$  application of these calculations to our SIFTO-measured decline rates gives  $\Delta m_{15}(B)=0.98\pm 0.08$  for the  $g'$  and  $r'$  bands, and or  $1.05\pm 0.12$  when for the  $r'$  band, when the 2011fe spectra were used; and  $\Delta m_{15}(B)=0.95\pm 0.08$  or  $1.02\pm 0.12$  using the Hsiao template. Foley et al. (2014) state that the  $V$ -band maximum was  $10.61\pm 0.05$ , whereas our fitting obtains this to be  $10.66\pm 0.02$ . We obtain a  $t_{Bmax}$  which is consistent with the values found by Foley et al. (2014).

## 4.6 Spectroscopy

The LT data spectroscopic reduction was done in two halves, corresponding to the blue and red arms of FRODOSpec. Each spectrum was manually searched through to select fibres which had signal. An appropriate top threshold was applied, to ensure cosmic rays were not affecting the spectrum. The signals from these fibres were combined; the spectra were formed using the ONEDSPEC IRAF package. The SN spectra were calibrated in flux using spectra of Feige34. The accuracy of the flux calibration process was confirmed by a successful calibration of the star back onto itself. This was done by running the calibration process on the observations of the standard star, and checking this against the IRAF data for the star, see Figure 4.6. The INT data were reduced using the STARLINK software (Disney & Wallace, 1982). The spectrophotometric standard used to reduce the INT data was Feige66.

A full plot of a SN 2014J spectrum with the main absorption lines labelled is found in Figure 4.7 and the early time spectral evolution of SN 2014J is plotted in Figure 4.5. The spectra have a very strong Si II 6355 Å absorption line. They also have high velocity features at early epochs; the main high velocity feature is exhibited by the Ca II IR triplet around  $\sim 7900$  Å. Furthermore, at even earlier times up to  $-12$ d Goobar et al. (2014) have found a strong high velocity feature of Si II 6355 Å. Figure 4.5 demonstrates the extent of the reddening, which means that the flux in the blue arm is extremely suppressed. The evolution of the Si II 6355 Å line can be seen in Table 4.2. As expected, as the photosphere recedes, the velocity of the ejecta decreases and hence the wavelength of the absorption line increases, although this may not always be apparent over smaller intervals. This is due to the resolution of the spectra and the errors on the velocity. The velocity gradient from the Si II 6355 Å line between  $+0$  to  $+9$ d relative to  $B$ -band maximum is  $58.8 \text{ km s}^{-1} \text{ day}^{-1}$ . This makes SN 2014J a Low Velocity Gradient (LVG) SN Ia (Benetti et al., 2005). It can be seen in the LT post

Table 4.2: Log of the Si 6355Å absorption line velocities. The resolution of the spectra is  $\sim 9\text{\AA}$ , this value has been used to calculate the error on the velocity of the Si II line.

Epoch	MJD <sup>a</sup> (d)	Phase <sup>b</sup> (d)	velocity <sup>c</sup> (kms <sup>-1</sup> )
2014-01-26	56684.12	-8	12973±424
2014-01-27	56685.12	-7	12643±424
2014-02-03	56692.01	+0	11758±424
2014-02-04	56692.9	+1	11697±424
2014-02-05	56693.89	+2	11686±424
2014-02-06	56694.96	+3	11552±424
2014-02-07	56695.89	+4	11640±424
2014-02-08	56696.89	+5	11412±424
2014-02-09	56697.97	+6	11529±424
2014-02-11	56709.87	+8	11408±424
2014-02-13	56701.877	+10	11228±424

<sup>a</sup> Modified Julian Day number

<sup>b</sup> relative to *B*-band maximum (days)

<sup>c</sup> velocity of the Si 6355Å absorption line

maximum spectra at +6, +8 and +10d that P-Cygni re-emission redwards of the Si II 6355 Å absorption has a flat top, which is also visible in the HST data at +11.3 d (Foley et al., 2014).

By using the correlation between the ratio of the depth of the silicon lines, 5972 and 6355 Å, and absolute magnitude and therefore  $\Delta m_{15}(B)$  (Nugent et al., 1995) a photometry-independent approximation for the  $\Delta m_{15}(B)$  of SN 2014J can be obtained. The INT spectra from +1d are used to do this, as the INT data cover the 5972 Å feature. The value derived is  $\Delta m_{15}(B)=1.11\pm 0.02$ , which is consistent with the values found by Marion et al. (2015) and Foley et al. (2014). Furthermore it is possible to use the EW of the Si II 5972 Å to estimate the  $\Delta m_{15}(B)$  (Hachinger et al., 2006). Using this method  $\Delta m_{15}(B)$  was found to be  $1.27\pm 0.15$ .

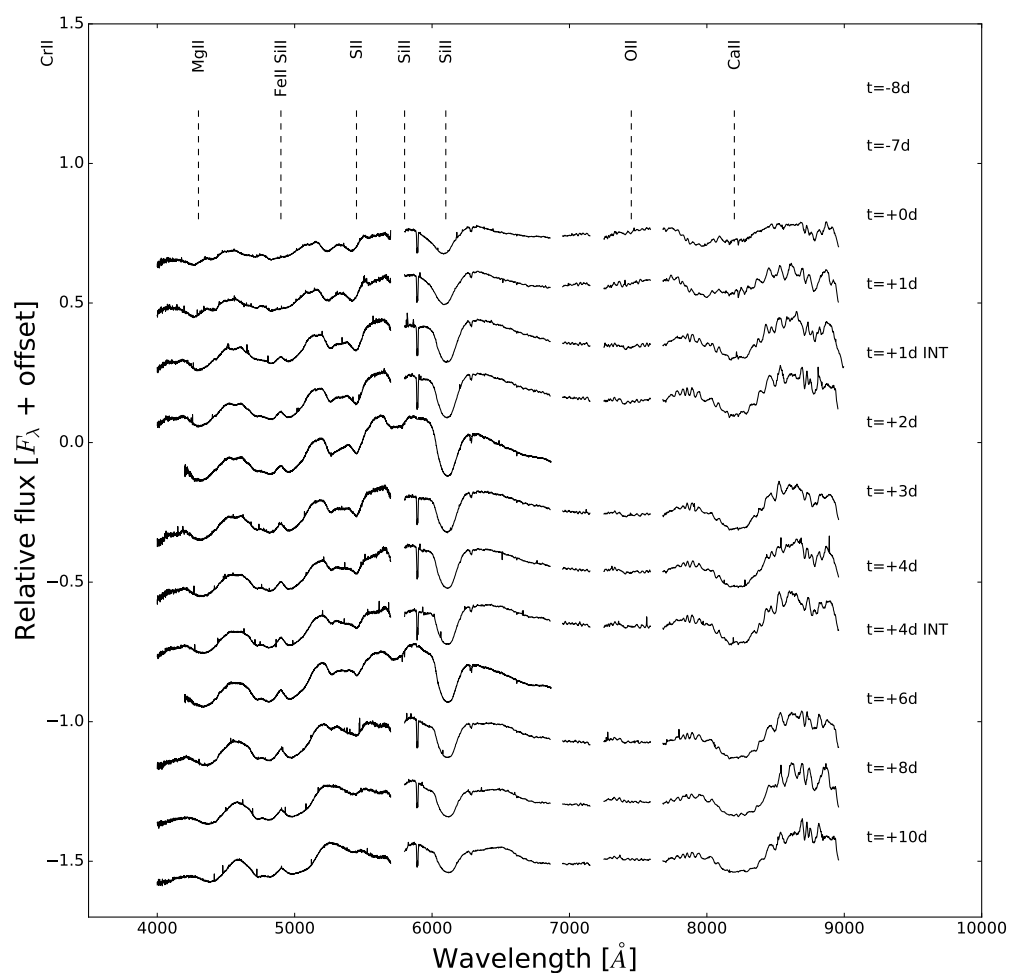


Figure 4.5: All spectral observations of SN 2014J, LT and INT. The time is given relative to rest-frame  $B$ -band maximum. The spectra have not been corrected for reddening. There were no data collected between 5700-5800  $\text{\AA}$  for the LT observations and the two atmospheric absorption lines have been removed. All of the plots have been offset by an arbitrary amount for the purpose of presentation.

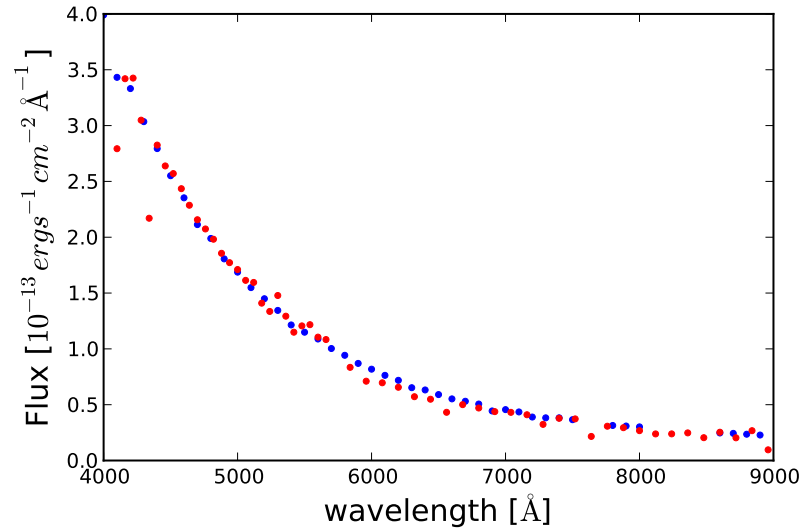


Figure 4.6: A check of the flux calibration process of Feige34 back on to itself. The blue points are the catalogue data, and the red the data from the observations.

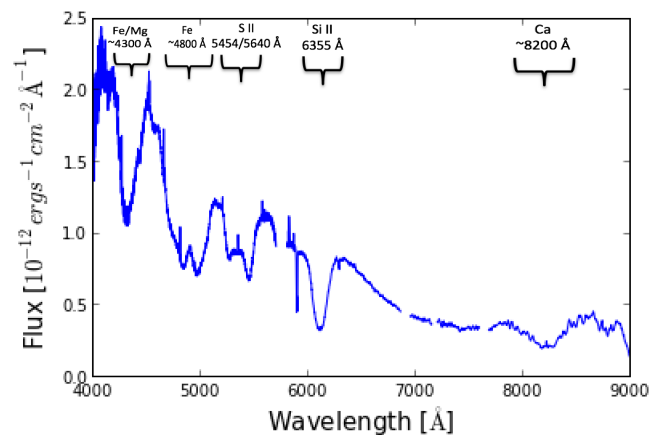


Figure 4.7: An overview of the features of SN 2014J. This spectrum has been dereddened and was taken at B-band maximum.

## 4.7 Models

Ten epochs of LT data have been modelled using the abundance tomography technique. All of the spectra have been dereddened using the CCM law. A host galaxy extinction of  $E(B - V) = 1.2$  mag ( $R_V = 1.38$ ) is used. These values are where the model produce the best fits, and are also consistent with the values of Amanullah et al. (2014) and Foley et al. (2014). The MC radiative transfer code is successful at modelling a variety of SN, therefore the models of SN 2014J are a good indication that the derived reddening values are correct. One-shell models were produced with different values of  $E(B - V)$ , and it was found that if this value was increased the input luminosity of the model had to be increased. This meant there was too much flux in the model and it peaked in the UV rather than the optical.

The time since explosion is one of the input parameters needed for the modelling process, therefore the rise time of SN 2014J is needed. There are pre-discovery images of SN 2014J, in which it first appears at Jan. 14.75 UT (Zheng et al., 2014) which gives it a bolometric rise time of  $\sim 20$  days. The main input parameters can be found Table 4.3.

Choosing a reasonable density profile is important in producing a physically meaningful and well-fitting model. The density distribution chosen for SN 2014J is the W7 model (Nomoto et al., 1984). The W7 model was selected as SN 2004eo, SN 2003du and SN 2002bo can all be reasonably modelled with this density profile. Therefore I can see if there is continuity in results. A higher density can lead to enhanced absorption lines, therefore it is important to select the appropriate one for the explosion. The most marked effects of the density on photospheric spectra occur at the earliest epochs, when the density of the outermost layers strongly modulates (e.g. the UV flux (Mazzali et al., 2014)). Therefore, moderate deviations in the outer density profile will not affect the results obtained from the regions explored in this work, as the modelling

Table 4.3: Input parameters and calculated converged temperature.

Epoch <sup>a</sup>	Epoch <sup>b</sup>	Velocity	Bol. Lum	Temp
$t_B$ (d)	$t_{exp}$ (d)	$v_{ph}$ (km s <sup>-1</sup> )	log(L <sub>⊙</sub> )	T <sub>BB</sub> (K)
-8	12	12300	9.295	10200
-7	13	11990	9.408	10100
+0	20	9480	9.455	9200
+1	21	8970	9.46	9000
+2	22	8440	9.43	8900
+3	23	7930	9.39	8800
+4	24	7480	9.355	8600
+6	26	6500	9.32	8400
+8	28	5450	9.250	8100
+10	30	4400	9.22	7800

<sup>a</sup> Relative to *B*-band maximum

<sup>b</sup> Days after the explosion

begins at an epoch of  $-8$  days relative to *B*-band maximum.

The main limitations of the analysis concern the high velocity outer layers of the ejecta, the extinction values, the distance to SN 2014J and the lack of UV data.

This section will analyse each epoch of the models and observations. In the models the iron-group content is parameterised in terms of two quantities, Fe and <sup>56</sup>Ni at the time  $t = 0$ . This gives us the abundance of Fe, <sup>56</sup>Co and <sup>56</sup>Ni at any point of time, assuming that the abundances of directly-synthesised Co and Ni are negligible. It should be noted that any Fe discussed in this section is stable iron.

### 4.7.1 Day $-8$

The first spectrum was observed 8 days before B-band maximum,  $t_{exp} = 12$  days, see Figure 4.8. As this spectrum is before *B*-band maximum it has a high photospheric velocity,  $v_{ph} = 12300$  km s<sup>-1</sup>, the effective temperature is 10200 K and the bolometric luminosity is  $10^{9.295} L_{\odot}$ . The strongest photospheric absorption lines, which are indi-

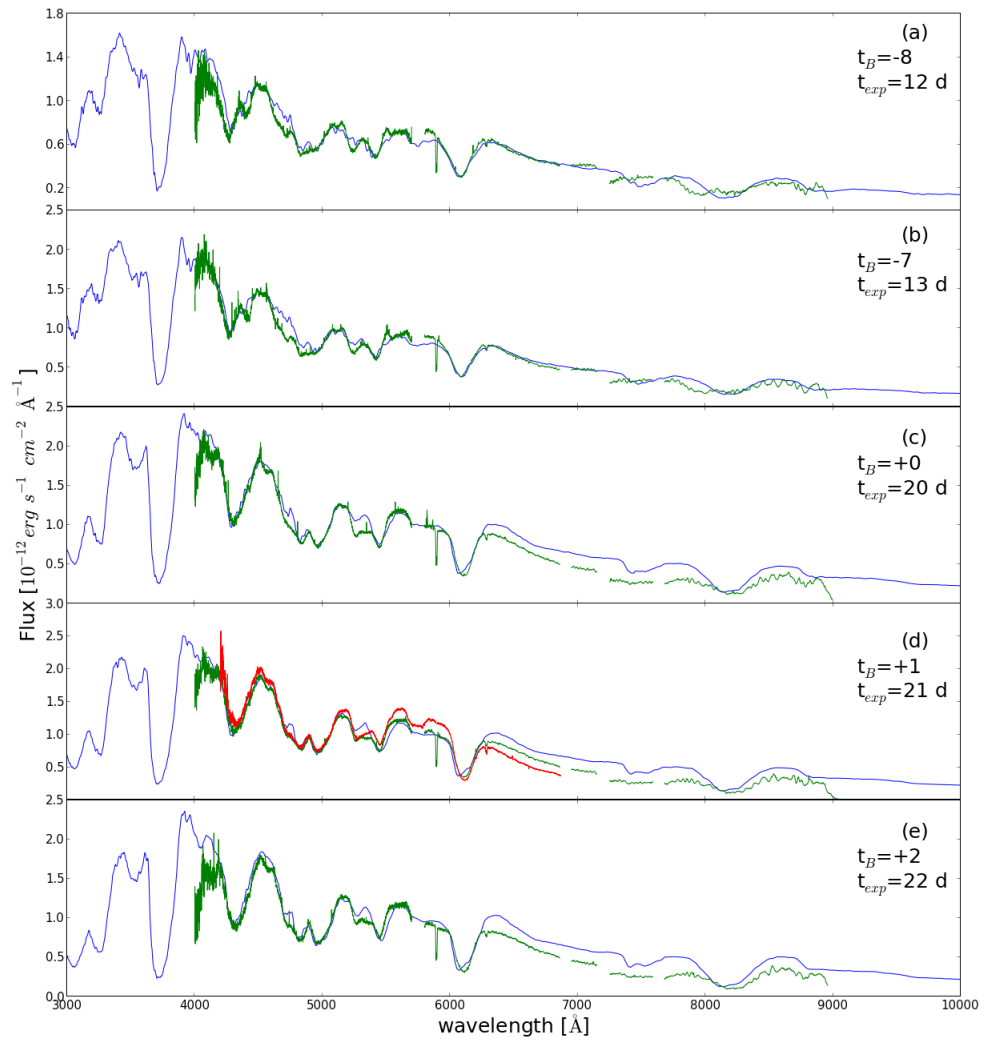


Figure 4.8: Modelled (blue) and observed spectra (green) of SN 2014J. Plot (a) is from -4d, (b) is from -3d, (c) is +0d maximum, (d) is +1d and (e) is +2d. All of the dates are relative to B-band maximum. All spectra have been dereddened. The red spectrum at +1 d is from the INT.

cated in Figure 4.7 , are dominant from the beginning of the time series to at least a week after maximum.

There are strong Si II 6355 Å, S II 5454 Å and 5640 Å features. Due to this the model requires a photospheric abundance of 12% Si and 9% S by mass, with 13% Mg to produce the Mg II 4481 Å line. The Mg II 4481 Å line is the dominant line in the 4300 Å feature. The O abundance is 60% and the Ca is 1%. There are strong Ca II features in this modelled spectrum, including a large absorption line in the H&K feature in the near UV (3934, 3968 Å). This absorption line is produced by the models in a strength consistent with the HST data (Foley et al., 2014). Although this NUV Ca line region is not covered our observations, the Ca II IR triplet is present from which Ca abundances can be inferred. The photospheric Ca II IR triplet is modelled successfully, but there is no attempt to model the high velocity feature. An iron abundance of 4% is required to produce the Fe III 5150 Å absorption line. The  $^{56}\text{Ni}$  abundance is at 0%, because the ejecta at this epoch are still in the high velocity outer layers of the photosphere. Ti+Cr are at a photospheric abundance of 0.3% by mass. There is a low abundance of C at this high velocity as there are no C spectral features in the optical data, suggesting that all the carbon may be in earlier time spectra, although Marion et al. (2015) do find C I at 1.0693  $\mu\text{m}$ . However, if is added into the models it is found that the C feature is stronger than observed . Therefore the C found in the NIR must be due to a very small abundance. There is a small absorption line in the optical observed at  $\sim 6200$  Å, where one would expect C, however this line is too narrow and probably not a C feature. The model at this epoch produces a particularly good match for the Fe II/Mg II 4200 Å, S II 5640 Å and Si II 6355 Å features.

### 4.7.2 Day -7

The second spectrum was taken  $-7$ d from  $B$ -band maximum,  $t_{exp}=13$  days. The luminosity at this epoch is  $10^{9.408} L_{\odot}$  and  $v_{ph}=11990$  km s $^{-1}$ . There is very little variation between the first two epochs as they are only taken 1 day apart. The main chemical changes from the previous epoch are that Si has increased to a photospheric mass abundance of 15% and S to 10%. The  $^{56}\text{Ni}$  has also increased to 3%. The  $\sim 4200$  Å feature is predominantly Mg II 4481 Å with smaller contributions from Fe III 4419 Å. The Mg abundance is 10% and the O abundance has decreased to 56%. The Si III 4550 Å line is successfully modelled, and this is the last FRODOSpec spectrum with a prominent Si III feature.

### 4.7.3 Day+0

The third spectrum was taken on the night of  $B$ -band maximum,  $t_{exp}=20$  days, as is shown in Figure 4.8. The luminosity is  $10^{9.455} L_{\odot}$  and photospheric velocity  $v_{ph}=9480$  km s $^{-1}$ . The Si and S abundances have increased relative to the previous epoch to photospheric mass abundances of 17% and 12% respectively, and the  $^{56}\text{Ni}$  has stayed constant at 3%.  $^{56}\text{Fe}$  has also increased by 2% to 6%. Conversely, the Mg and O abundances have decreased to 5% and 55% respectively. There is now a notable excess in flux in the red side of the spectrum due to the black body approximation. The  $B$ -band modelled absolute unreddened magnitude is  $-18.79$ . At this epoch the modelled Si III 4550 Å absorption line is not as strong as the previous epochs. Furthermore, in the previous spectrum the 4800 Å feature which have dominant Si II 5056 Å and Fe II 5169 Å absorption lines are merged into one, whereas at this epoch they have two distinct minima. Ca absorption is now more prominent in both the model and the observations, and is seen in the Ca II IR triplet at  $\sim 8200$  Å.

#### 4.7.4 Day+1

The next spectrum in the series was observed on +1 d relative to *B*-band maximum,  $t_{exp}=21$  days. It has a luminosity of  $10^{9.460} L_{\odot}$  and a photospheric velocity of  $v_{ph}=8970$  km s<sup>-1</sup>. This spectrum is at maximum bolometric luminosity, which is consistent with it being between *B*-band and *V*-band maximum. Although the INT and LT spectra differ slightly, predominantly in the red side of the spectrum, the main absorption lines in the blue side of the optical are similar between the spectra. Due to this, the abundances obtained in our analysis would not change if just the INT or LT spectra were modeled. The abundances derived from this spectrum are very similar to the previous epoch; the Si decreases to 15%, the S to 10% the O to 57%. <sup>56</sup>Ni has increased to 11% and <sup>56</sup>Fe is constant at 6%. The effective temperature at this epoch is 9000 K, which is 200 K lower than the previous spectrum. The Mg abundance has decreased to 0%. The S II 5454 Å feature is not as strong in the model as the observed spectrum, however increasing S abundance would enhance the S II 5640 Å line. There is excess strength of O I and Mg II at 7773 Å and 7896 Å which could be an indication that there is excess mass at this velocity. This feature occurs in most of the epochs in the model, and is more dominant in late time spectra.

#### 4.7.5 Day +2

The fifth spectrum was observed on  $t_{exp}=22$  d, see Figure 4.8. Its luminosity is  $10^{9.430} L_{\odot}$  and photospheric velocity is  $v_{ph}=8440$  km s<sup>-1</sup>. The effective temperature is 8900 K. The abundances at this epoch are very similar to the previous one, except for <sup>56</sup>Ni which begins to increase dramatically to 36%, and S which decreases to 4%; Si and O also decrease to 10% and 43% respectively. At this epoch Ca stays constant at 2%. The *B*-band unreddened modelled absolute magnitude of this spectra is -18.85. At

this epoch the  $\sim 4200 \text{ \AA}$  feature is still dominated by the Fe III 4419  $\text{\AA}$  and Mg II 4481  $\text{\AA}$  lines.

### 4.7.6 Day +3

The next spectrum was observed on  $t_{exp} = 23$  days, refer to Figure 4.9. The luminosity at this epoch is  $10^{9.390} L_{\odot}$ , the photospheric velocity is  $v_{ph} = 7930 \text{ km s}^{-1}$ , the effective temperature is 7900 K and the *B*-band modelled absolute magnitude is  $-18.62$  mag. The modelled S II 5640  $\text{\AA}$  feature is stronger than the observed one; this is a problem which consistently occurs in the model. To make the S II the same strength as the observed one it would require the abundance of S to be reduced in the early-epoch models. However the early-time spectra rather than the late time ones were chosen to be fit, as these can lead us to more information about the high velocity abundances. At this epoch the O has a photospheric abundance of 0%. The Si and S have also decreased to an abundance of 4% and 2% by mass respectively. The Fe II 4420  $\text{\AA}$  and Si II 6355  $\text{\AA}$  lines are modelled successfully. The wide deep absorption line at 8200  $\text{\AA}$  is the Ca II IR triplet absorption line, and the calcium abundance has been reduced to 1% to decrease the strength of this line. At this epoch  $^{56}\text{Ni}$  begins to dominate and is at 88%.

### 4.7.7 Day +4

The spectrum from +4 d has a luminosity of  $10^{9.345} L_{\odot}$  and photospheric velocity of  $v_{ph} = 7480 \text{ km s}^{-1}$ . There is a similar discrepancy between the INT and LT data as in the +1 d plot, however once again this does not affect the abundances obtained from our fits. From this epoch the absorption lines are beginning to be stronger than the observed ones. This includes, the modelled Fe/Mg 4300  $\text{\AA}$  and Fe 4800 $\text{\AA}$  features, which are produced by dominant Fe III 4419  $\text{\AA}$  and Fe II 5018  $\text{\AA}$  absorption lines. However,

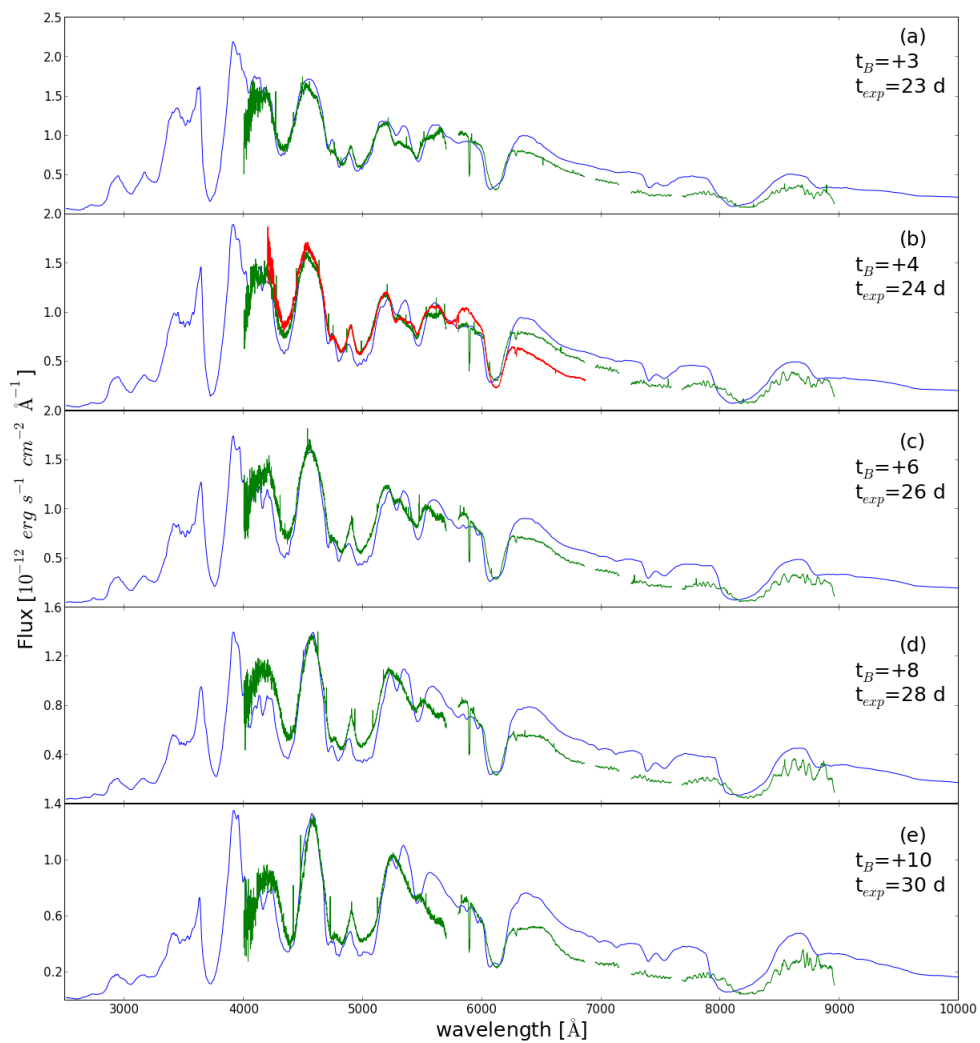


Figure 4.9: Modelled (blue) and observed spectra (green) of SN 2014J. Plot (a) is from +3d, (b) is from +4d, (c) is +5d, (d) is +6d and (e) is +8d. All of the dates are relative to B-band maximum. All spectra have been dereddened. The red spectrum of +4 d is from the INT.

to refine this fit requires the abundances of these lines at high velocity epochs to be reduced, affecting the early time spectra. Therefore, it can be suggested that the excess absorption could be due to too much mass at  $v_{ph}=7480 \text{ km s}^{-1}$ . Part of the excess in strength of the  $^{56}\text{Fe}$  lines could also be due to the decay of  $^{56}\text{Ni}$ . Due to this excess strength in Fe, its photospheric abundance has been reduced to 0.1%. The Si and S abundances have decreased to 0%, and the  $^{56}\text{Ni}$  is at 99%. The effective temperature at this epoch is 8600 K.

#### 4.7.8 Day +6

The eighth spectrum was taken 26 days after explosion. It has a luminosity of  $10^{9.32} L_{\odot}$ , a photospheric velocity of  $v_{ph}=6500 \text{ km s}^{-1}$  and an effective temperature of 8400 K. The  $^{56}\text{Ni}$  photospheric abundance is at 99%. The Fe II 4340 Å, S II 5606 Å and Fe III 4419 Å absorption lines are much deeper in the model than the observations. The unreddened modelled *B* and *V* magnitudes are 9.5 mag and 9.1 mag respectively.

#### 4.7.9 Day +8

The next spectrum has a luminosity of  $10^{9.250} L_{\odot}$  and photospheric velocity is  $v_{ph}=5950 \text{ km s}^{-1}$ . The  $^{56}\text{Ni}$  abundance has stayed constant. The difference between the model and observation becomes larger, as shown by the Fe II 4549 Å line in the 4800 Å feature. At this epoch there is a significant amount of  $^{56}\text{Ni}$  above the photosphere. Therefore it is not unexpected that the difference between the models and observed spectra begins to increase.

### 4.7.10 Day +10

The final epoch that was modelled is from +10 d from *B*-band maximum. It has a luminosity of  $10^{9.22} L_{\odot}$ , a photospheric velocity of  $v_{ph}=5450 \text{ km s}^{-1}$  and an effective temperature of 7800 K. At this epoch there is no Si or S abundance, and the  $^{56}\text{Ni}$  abundance is the most dominant, at almost 100%. The Ca abundance has now decreased to 0%.

## 4.8 Abundance stratification

An abundance stratification distribution plot for the photospheric layers of the ejecta is shown in Figure 4.10. This plot demonstrates how the abundances of SN 2014J develop at early times, from  $-8$  d to +10 d. The abundance distributions of the outermost layers can not be fully determined in the ejecta as I do not have spectra before  $-8$ d. The abundances in the outer shell are slightly unusual, in that there is no carbon abundance. This implies that if any C is present in the ejecta it had to be at the very highest velocities. The other notable abundance is Fe which begins at 0.1% and rises to 6%. I have attempted to increase this, but doing so dramatically strengthens the Fe 4800 Å feature at all epochs. Therefore the initial abundances of the outer shell, which has a velocity of  $14800 \text{ km s}^{-1}$ , are Si 10%, O 78%, S 4%,  $^{56}\text{Ni}$  0%, Mg 7%, C 0.0%,  $^{56}\text{Fe}$  0.1%, with heavier elements making up the remaining abundance.

At high velocities, between  $8440\text{-}14800 \text{ km s}^{-1}$ , there is a large oxygen abundance which starts at 78%. The Si distribution starts at 10% due to the strong Si II 6355 Å feature, and it increases to 17% at  $9480 \text{ km s}^{-1}$  before decreasing to 0% at  $7480 \text{ km s}^{-1}$ . Sulphur also follows a similar distribution with respect to velocity, although it always has a smaller abundance than Si. The sulphur distribution starts at 3.5% before peaking at 12%. The basic abundance evolution of the ejecta involves O dominating

followed by the IME and then by the heavy elements. In the abundance distribution plot, Figure 4.10, the Fe starts at 0.1% and rises to 6%. In Figure 4.10 the IME elements are significant at high velocities. From this it can be inferred that the lighter elements may be at even higher velocities. Therefore earlier spectra are needed to gain information about these lighter elements. As expected from a normal SN Ia explosion  $^{56}\text{Ni}$  dominates the abundance. This happens between 8440-7930  $\text{km s}^{-1}$ , where the  $^{56}\text{Ni}$  goes from a photospheric mass fraction of 36% to 83%. The Ti+Cr abundances stay at a constant level throughout the whole explosion at 0.3%. Calcium starts at 2% at 12300  $\text{km s}^{-1}$  and it decreases to 1% at 5450  $\text{km s}^{-1}$ .

The integrated abundances of the most important elements in the photospheric ejecta, which is at a velocity above 4400  $\text{km s}^{-1}$ , are  $M(\text{Mg})=0.07 M_{\odot}$ ,  $M(\text{Fe})=0.03 M_{\odot}$ ,  $M(\text{O})=0.40 M_{\odot}$ ,  $M(\text{S})=0.058 M_{\odot}$ ,  $M(\text{Si})=0.09 M_{\odot}$  and  $M(^{56}\text{Ni})=0.47 M_{\odot}$ . When the nebular phase spectra are available the  $^{56}\text{Ni}$  could increase to a total integrated abundance of 0.72  $M_{\odot}$ . The final total integrated abundances can be confirmed when late time spectra of SN 2014J are observed. Due to ground based telescopes not being able to observe the UV part of the spectra, the iron group element abundances of SN 2014J I have given here are subject to 20% uncertainty, which nebular modelling will allow us to approve upon.

SN 2011fe and SN 2014J are apparently photometrically similar. SN 2011fe has been used to determine the extinction of SN 2014J (Amanullah et al., 2014), and it has also been modelled using the same MC radiative transfer code (Mazzali et al., 2014). The total  $^{56}\text{Ni}$  abundance of SN 2011fe (Mazzali et al., 2014) and SN 2014J are very similar (0.4-0.7  $M_{\odot}$  and 0.47-0.72  $M_{\odot}$  respectively, the large range is due to not knowing abundance distribution in the nebular phase) Furthermore, the abundances in the photospheric region of the SN 2011fe ejecta are remarkably similar to those of SN 2014J. Changing the density profile in the models is not likely to qualitatively affect

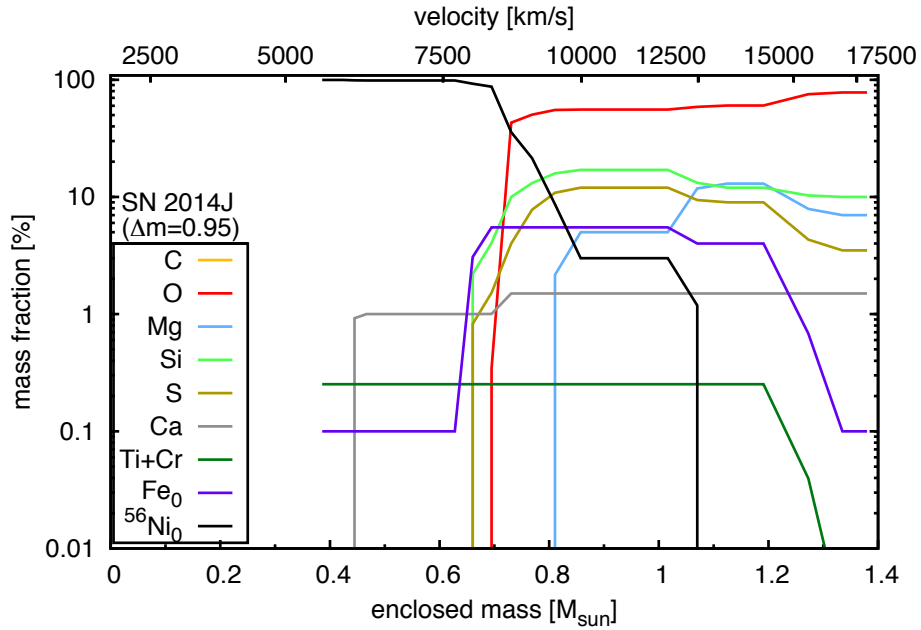


Figure 4.10: The abundance distribution of SN 2014J. The Ni/Co/Fe abundances are given in terms of mass fractions of  $^{56}\text{Ni}$  ( $^{56}\text{Ni}_0$ ) and stable Fe ( $\text{Fe}_0$ ) at  $t = 0$ . In the spectral models no stable Ni or Co and no radioactive Fe are assumed to be present.

the abundance pattern in the regions of the ejecta explored by the spectra.

## 4.9 Work carried out after this

Since I have carried out this project on SN 2014J a number of other papers have been published on it. These include high resolution and high cadence optical photometry and spectroscopy. Jack et al. (2015) found that spectra show several very sharp Na ID doublet absorption components. This was interpreted as M82 have interesting sub-structures. Graham et al. (2015) found that the spectra of SN 2014J shows several of the common diffuse interstellar bands. There have also been mid-IR observations. Telesco et al. (2015) obtained the first ever mid-IR time series of a SNe Ia. They found a  $^{56}\text{Ni}$  mass of 0.6, which is in line with my work, and also agree that this explosion was from a Ch-mass WD. Srivastav et al. (2016) present both NIR and optical observations

of SN 2014J. They also conclude that this SNe has a  $^{56}\text{Ni}$  mass of 0.6 and a  $\Delta m_{15}(B)$  of 1.08 mag. Furthermore, they claim that the low Fe ratio in the nebular spectra of SN 2014J hints towards clumpiness in the ejecta. However, Porter et al. (2015) present spectropolarimetric observations of SNe 2014J and conclude that the ejecta showed no asymmetry. Bikmaev et al. (2015) presented nebular observations of SN 2014J, they conclude that the location of the SNe Ia must have been of solar metallicity, due to the Fe abundance. This is not dissimilar from the conclusions drawn from my work. Vallely et al. (2016) performed a synthetic spectral analysis on SN 2014J, using SNI+++. They claimed that there was no oxygen in the ejecta of SN 2014J. This is clearly wrong, and their results were contaminated by atmospheric absorption lines. The HST spectra of SN 2014J published by Foley et al. (2014) show a clear oxygen absorption profile. Furthermore, Vallely et al. (2016) claim that there is no Fe in the ejecta before 23 days past maximum light, this is also an erroneous result. It is the first time this has ever been claimed, as it disagrees with all SNe Ia models.

## 4.10 Summary

Photometric and spectroscopic observation of SN 2014J, the closest SN Ia in at least the last 28 years are presented. The observations were obtained with the LT and INT. SDSS  $g'r'i'$  light curves and a spectral time series evolution over 12 epochs from  $-8\text{d}$  to  $+10\text{d}$ , relative to  $B$ -band maximum, are presented. All of the spectra were calibrated in flux, and atmospheric absorption lines were removed. The spectra show a very deep Si II 6355 Å line and a Ca high velocity feature at  $\sim 7900$  Å. The  $\Delta m_{15}(B)$  of SN 2014J is  $0.88 \pm 0.08$  or  $0.95 \pm 0.12$  using the  $g'$  and  $r'$ -band or  $r'$ -band respectively, and by fitting them through SIFTO. When correcting for reddening this produced values of  $\Delta m_{15}(B) = 0.98 \pm 0.08$  or  $1.05 \pm 0.12$ , respectively, using the SN 2011fe spectra, and

$\Delta m_{15}(B)=0.95\pm 0.08$  or  $1.02\pm 0.12$  for the Hsiao template.

SN 2014J is a highly reddened SN Ia which does not follow the conventional Galactic reddening law ( $R_V=3.1$ ). I adopt the CCM law with a foreground galactic value of  $E(B - V)=0.05$  ( $R_V=3.1$ ) and host galaxy extinction of  $E(B - V)=1.2$  ( $R_V=1.38$ ).

SN 2011fe and SN 2014J were found to have a comparable Ni masses,  $0.4-0.7 M_\odot$  and  $0.47-0.72 M_\odot$  respectively, when modelled using the same MC radiative transfer code. However, due to their different in uncorrected decline rate I could expect these values to change. This could be revealed with the use of the UV data and the nebular spectra.

The spectra were modelled at 10 epochs, before and after  $B$ -band maximum, inferring a best-fit abundance stratification. As one would expect, at higher velocities ( $12400 \text{ km s}^{-1}$ ) there is a large abundance of oxygen. As the photosphere recedes ( $8440 \text{ km s}^{-1}$ ) the IME elements dominate, Si and S. Then at low velocities the radioactive Ni dominates below  $8000 \text{ km s}^{-1}$ . This leads to the prediction that the characteristic line width of the iron emission line in the nebular spectra (Mazzali et al., 1998) will be in the order of  $8000 \text{ km s}^{-1}$ .

Synthetic spectra reproduce the spectral evolution of SN 2014J, and the final integrated abundances of SN 2014J are  $M(\text{Mg})=0.07 M_\odot$ ,  $M(\text{Fe})=0.03 M_\odot$ ,  $M(\text{O})=0.40 M_\odot$ ,  $M(\text{S})=0.05 M_\odot$ ,  $M(\text{Si})=0.09 M_\odot$  and  $M(^{56}\text{Ni})=0.47-0.72 M_\odot$ . Our results are consistent with the current understanding of SN Ia reddening and early time abundance distribution. The observations and modelling in this work are of particular significance because of the close proximity of SN 2014J. Furthermore, SN 2014J is the typical example of a normal SN Ia, making our models a good basis for studying further objects.

## 5. SN 1986G

### 5.1 Preface

SN 1986G ‘bridges the gap’ between normal and sub luminous type Ia supernova. With the knowledge that transitional SNe Ia are interesting and the ability to model a SNe Ia, the data of SN 1986G was modelled. The abundance tomography technique is used to determine the abundance distribution of the elements in the ejecta. SN 1986G was found to be a low energy Chandrasekhar mass explosion. Its kinetic energy was 70% of the standard W7 model ( $0.9 \times 10^{51}$  erg). Oxygen dominates the ejecta from the outermost layers down to  $\sim 9000 \text{ km s}^{-1}$ , intermediate mass elements (IME) dominate from  $\sim 9000 \text{ km s}^{-1}$  to  $\sim 3500 \text{ km s}^{-1}$  with Ni and Fe dominating the inner layers  $< \sim 3500 \text{ km s}^{-1}$ . The final masses of the main elements in the ejecta were found to be, O= $0.33 M_{\odot}$ , IME= $0.69 M_{\odot}$ , stable NSE= $0.21 M_{\odot}$ ,  $^{56}\text{Ni}$ = $0.14 M_{\odot}$ . An upper limit on the carbon mass is set at C= $0.02 M_{\odot}$ . The spectra of SN 1986G consist almost exclusively of singly ionised species. SN 1986G can be thought of as a low luminosity extension of the main population of SN Ia, with a large deflagration phase that produced more IMEs than a standard SN Ia. Work from this project was published in Ashall et al. (2016). All of the early time spectral modelling, as well as the work on abundance distributions, was carried out by myself. Paolo Mazzali modeled the nebular spectra and produced the synthetic lightcurves, and Elena Pian calculated the

observed bolometric light curve.

## 5.2 SN 1986G

SN 1986G was the first object to lead to the questioning of Type Ia Supernovae as standard candles (Phillips et al., 1987). Its light curve was faster and dimmer than all of the previously discovered SNe Ia. It had a rapidly declining light curve at early phases and slow expansion velocities compared to a normal SN Ia (Phillips et al., 1987; Cristiani et al., 1992). SN 1986G was located in NGC 5128, also known as Centaurs A, which is at a distance of  $3.42 \pm 0.18$  Mpc (Ferrarese et al., 2007). This made it one of the closest SNe Ia ever discovered, until SN 2014J (Ashall et al., 2014). SN 1986G was observationally red, with a  $(B - V)_{Bmax} = 0.88 \pm 0.03$  mag. This could be interpreted as SN 1986G suffering from a large amount of extinction. However, SNe Ia suffer from a colour/extinction degeneracy. Recently, for normal SNe Ia, this colour/extinction degeneracy has been overcome (Saselli et al., 2016). For unusual SNe Ia this degeneracy still remains an issue, and values of host galaxy extinction can be very uncertain.

SN 1986G is a “transitional” SN Ia. “Transitional” in this case refers to SNe Ia that bridge the gap between 91bg-like and normal SNe Ia (Ashall et al., 2016). Figure 5.1 presents the  $B$ -band absolute magnitude light curves of four SNe Ia with a variety of decline rates,  $\Delta M_{15}(B)$  (2011fe, 2004eo, 1986G and 2005bl). SN 2011fe was a stereotypical normal SNe Ia with  $\Delta M_{15}(B) = 1.1 \pm 0.05$  mag, a broad LC shape, and a normal spectrum, see Figure 5.2. SN 2004eo had  $\Delta M_{15}(B) = 1.47 \pm 0.07$  mag, it was slightly less luminous than SN 2011fe, and had normal spectra. SN 1986G had  $\Delta M_{15}(B) = 1.81 \pm 0.07$  mag, a narrow LC and a cooler spectrum. SN 2005bl was a 91bg-like SN, with  $\Delta M_{15}(B) = 1.93 \pm 0.1$  mag. SN 1986G sits half-way between normal and subluminal SNe Ia.

The environment of SN 1986G is highly unusual and merits some discussion. The host system is the peculiar radio galaxy NGC 5128 which is generally classified in terms of its optical morphology as a lenticular or elliptical galaxy. This implies a dominant old stellar population, but this may well be misleading, as SN 1986G occurred in the middle of the strong dust lane which gives NGC 5128 its peculiar appearance, but well offset from the active galactic nucleus. The dust lane is generally considered to be the result of a merger with a smaller gas-rich galaxy (Baade & Minkowski, 1954; Tubbs, 1980), and it is associated with substantial ongoing star formation, which is indicated by strong, extended clumpy  $H\alpha$  emission throughout most of the dust lane (see e.g., Bland et al., 1987). Anderson et al. (2015) found the location of SN 1986G to be associated with detectable  $H\alpha$  emission, even though it is not coincident with a bright H II region, so there is clearly a young stellar population in the immediate vicinity. Transitional SNe Ia are often found in peculiar galaxy environments, and this is clearly the case with SN 1986G.

Figure 5.2 shows the spectroscopic differences between these SNe Ia. All spectra have been corrected for host galaxy extinction. A strong  $\sim 4450 \text{ \AA}$  Ti II feature is an indicator of a subluminous SN Ia. SN 1986G is one of the few SNe Ia with an intermediate strength Ti II feature. Furthermore, the ratio of the Si II features ( $\sim 5970 \text{ \AA}$  and  $6355 \text{ \AA}$ ) is a good temperature indicator (Nugent et al., 1995; Hachinger et al., 2006). It is however an indirect temperature indicator, as it results from the saturation of the Si II  $\lambda 6355$  line. Si II becomes more abundant with respect to Si III at lower luminosities and temperatures, so that the Si II  $\lambda 5970$  line becomes stronger with respect to the Si  $\lambda 6355$  line. SN 1986G had a larger Si II ratio compared to normal SNe Ia, but one not as strong as a 91bg-like SN Ia. Therefore it is a transitional object. SN 1986G is the only published SNe Ia with these properties and good observational data, which demonstrates that these objects must be rare. SN 2011iv may also be classified as a

transitional SN because of its rapidly evolving LC, but it was spectroscopically normal (Foley et al., 2012).

A detailed theoretical understanding of SN 1986G should help to determine the relationship between 91bg-like and normal SNe Ia. This can be done by examining a time series of spectra and analysing their evolution. Normal SNe Ia show properties that are matched by delayed detonation explosions, and can be modelled using the W7 density profile, which is similar to most delayed detonation models except in the outermost layers (Stehle et al., 2005; Mazzali et al., 2008; Ashall et al., 2014). SN 1991bg had a low central density (Mazzali & Hachinger, 2012), which favours a merger scenario in which the combined mass of the merging WDs is below the Chandrasekhar mass. Similarly, the density distribution in SN 2003hv, which had  $\Delta M_{15}(B)=1.61$  mag, indicates a Sub-Chandrasekhar mass (Mazzali et al., 2011). Subluminous SNe Ia tend to occur in old stellar populations and are at the end of the SNe Ia parameter space (Ashall et al., 2016). Therefore, as it has been shown that 91bg-like SNe Ia could be the result of a different progenitors/explosion mechanism than normal SNe Ia. The question is, at which point do SNe Ia begin to depart from the standard explosion models, and what causes them to be different? The answer may be found by analysing individual transitional SNe Ia in detail.

This project uses the abundance tomography technique to infer the properties of SN 1986G. It starts with a summary of the data used (Section 5.3). The quality of the flux calibration of the spectra is then presented (Section 5.4), followed by a description of the modelling technique (Section 5.5). Photospheric-phase models are then presented in Section 5.6, while Section 5.7 discusses nebular-phase models. After this the full abundance tomography is carried out (Section 5.8). In Section 5.9 the results are re-evaluated and a modified density profile is used to improve the fits. A synthetic light curve is presented in Section 5.10 and compared to the bolometric light curve of

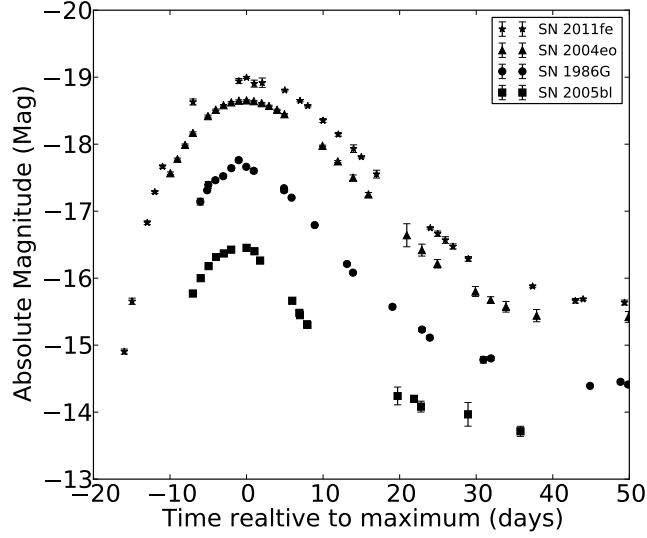


Figure 5.1: The  $B$  band absolute magnitude of four SNe Ia which have a variety of LC shapes.

Table 5.1: The  $\Delta M_{15}(B)$  and absolute  $B$  band magnitude of the SNe Ia used in Figures 5.1 and 5.2.

SN	$\Delta M_{15}(B)$	$M_B$	References
SN 2011fe	$1.1 \pm 0.05$ mag	-18.99	Munari et al. (2013)
SN 2004eo	$1.47 \pm 0.07$ mag	-18.65	Pastorello et al. (2007)
SN 1986G	$1.81 \pm 0.07$ mag	-17.76	Phillips et al. (1987); Taubenberger et al. (2008)
SN 2005bl	$1.93 \pm 0.1$ mag	-16.45	Taubenberger et al. (2008)

SN 1986G computed from the available photometry. Finally, the results are discussed and conclusions are drawn in Section 5.11.

### 5.3 Data

Abundance tomography modelling requires a time-series of spectra. The data in this work come from a variety of sources, which are listed in Table 5.2. Six spectra published by Cristiani et al. (1992) were used for the photospheric phase models. These spectra cover the range from  $-3$  d to  $+2$  d relative to  $B$ -band maximum. This is not ideal as it only covers a small range in velocity space, but information about the outer

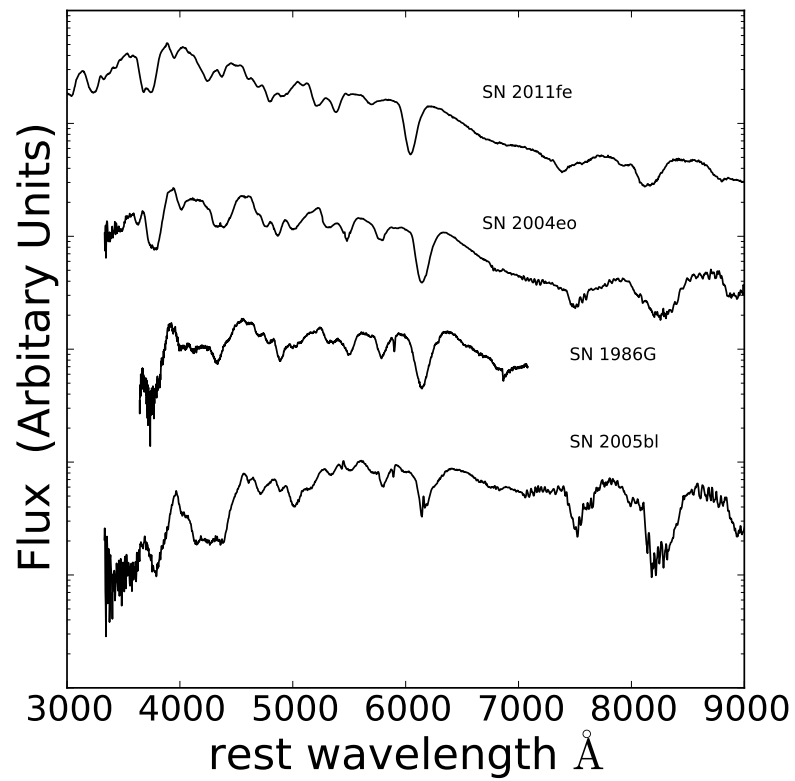


Figure 5.2: The spectra of four SNe Ia at *B* band maximum. The SNe correspond to the 4 SNe in Figure 5.1

Table 5.2: The spectra of SN 1986G.

Date	MJD	Phase (days)	source	telescope
7/5/1986	46557	-3	Cristiani et al. (1992)	ESO 2.2m B&C+CCD
7/5/1986	46557	-3	archive.stsci.edu/iue/	International Ultraviolet Explorer
8/5/1986	46558	-2	Cristiani et al. (1992)	ESO 2.2m B&C+CCD
9/5/1986	46558	-2	archive.stsci.edu/iue/	International Ultraviolet Explorer
9/5/1986	46559	-1	Cristiani et al. (1992)	ESO 1.5m B&C+IDS
10/5/1986	46560	+0	Cristiani et al. (1992)	ESO 1.5m B&C+IDS
11/5/1986	46561	+1	Cristiani et al. (1992)	ESO 1.5m B&C+IDS
12/5/1986	46562	+2	Cristiani et al. (1992)	ESO 1.5m B&C+IDS
22/1/1987	46817	+256	Cristiani et al. (1992)	EFOSC 3.6m

(but not the outermost) layers can still be inferred. Two near-UV spectra taken with the International Ultraviolet Explorer (IUE) are also used. Although these spectra have low signal-to-noise, they are important in that they allow us to determine the flux level in the NUV. The NUV flux level is important in determining the amount of line blanketing in the outer layers of the ejecta. To probe the inner layers of the SN ejecta a nebular phase spectrum is required. One such spectrum was obtained by Cristiani et al. (1992). The final stage of the modelling process involves modelling the bolometric light curve. The data used to construct the pseudo-bolometric light curve of SN 1986G are taken from a variety of sources (Cristiani et al., 1992; Frogel et al., 1987; Phillips et al., 1987).

## 5.4 Flux Calibration of spectra

Before a supernova can be modelled its spectra must be accurately flux calibrated. Getting accurate flux calibration from single split spectroscopy can be very difficult, therefore it is very useful if the spectra can be calibrated against multi-band photometric observation. For SN 1986G there is limited photometric coverage, and the spectra were calibrated against the  $V$  and  $B$  bands, taken from Phillips et al. (1987). A spectrum is accepted for modelling if it meets the minimum criteria, which is there should

Table 5.3: The  $B$  and  $V$  synthetic photometry ( $m_{spec}$ ) taken from the spectra, and real photometry ( $mB_{phot}$ ) obtained from Phillips et al. (1987).

Date	phase	$mB_{spec}$	$mV_{spec}$	$mB_{phot}$	$mV_{phot}$
7th May	-3	12.68	11.72	12.71	11.74
8th May	-2	12.62	11.65	12.65	11.67
9th May	-1	12.54	11.50	12.48	11.58
10th May	0	12.73	11.54	12.41	11.53
11th May	+1	12.52	11.38	12.51	11.48
12th May	+2	12.60	11.35	12.57	11.44

be a minimum accuracy level of 0.02 mag between synthetic photometry obtained from the spectra and the real photometry, this equates to  $\sim 1.8\%$  in flux. The real and synthetic photometry can be found in table 5.3 The original spectra are fitted through a function, which is determined by fitting a line between the ratio in flux between  $B$  and  $V$  photometric points obtained from the synthetic and observed photometry. The function takes the form,

$$F_{new} = F_{old} \left( \times \frac{\Delta F_V - \Delta F_B}{\lambda_V - \lambda_B} (\lambda - \lambda_B) + F_B \right) \quad (5.1)$$

where  $\lambda_B$  and  $\lambda_V$  are the effective wavelengths of the  $B$  and  $V$  passbands respectively.  $F_{new}$  is the correctly calibrated flux and  $F_{old}$  is the original flux from the spectrum, and  $\lambda$  is the wavelength of the spectrum ( i.e. 3700-7100Å).  $\Delta F_\psi$  from equation 5.1 is given by,

$$\Delta F_\psi = 10^{\frac{\Delta m_\psi}{-2.5}} \quad (5.2)$$

where  $\Delta m_\psi$  is the difference in  $V$  or  $B$  band magnitude between the real photometry and synthetic photometry from the observed spectra, (e.g  $\Delta m_V = mV_{phot} - mV_{spec}$ ).

Figure 5.3 shows the spectrum at maximum before and after correction for flux calibration, where it can be seen that the calibration correctly reduces the flux in the  $V$

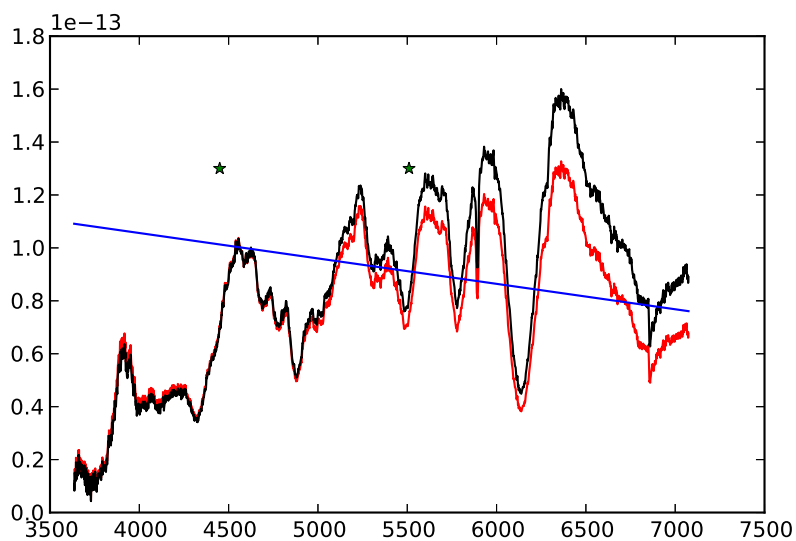


Figure 5.3: SN 1986G spectrum from 11th May. The back spectrum is the original and the red is the spectrum after flux calibration.. The stars are the center of the  $B$  and  $V$  bands.

Table 5.4: Synthetic photometry from the new spectra.

Date	phase	$\text{new}mB_{\text{spec}}$	$\text{new}mV_{\text{spec}}$
7th May	-3	12.70	11.74
8th May	-2	12.65	11.67
9th May	-1	12.49	11.58
10th May	+0	12.43	11.53
11th May	+1	12.51	11.48
12th May	+2	12.57	11.45

passband, and increases it in the  $B$ -band.

## 5.5 Modelling Techniques

### 5.5.1 Photospheric phase modelling technique

The photospheric phase modelling technique is described in chapter 3.

## 5.5.2 Nebular Phase modelling technique

The nebular spectrum was modelled using a 1D NLTE code similar to Mazzali et al. (2007). The code uses a Monte Carlo scheme to compute the propagation and deposition of the  $\gamma$ -rays, and positrons produced in the decay of  $^{56}\text{Ni}$  to  $^{56}\text{Co}$  and  $^{56}\text{Fe}$ , based on an assumed density profile, such as W7, and an abundance distribution. In the outer layers the abundances derived in the photospheric phase modelling are used, while inner layers are filled with the abundances that lead to a best match with the observations (Mazzali et al., 2007). The heating from the energy deposition is balanced by the cooling from line emission. Given a fixed distance and extinction, the mass of synthesised  $^{56}\text{Ni}$  in the explosion can be computed. Using a fixed density profile allows the abundance distribution in the inner layers to be determined. The ratio of the strongest [Fe II] and [Fe III] lines is a good indicator of the late time ejecta abundances. This analysis complements the early time spectra, and yields an abundance distribution throughout the whole ejecta.

## 5.5.3 Light curve code

A Monte Carlo code is used, with a fixed density profile and derived abundance distribution, to compute a synthetic bolometric light curve (Cappellaro et al., 1997; Mazzali et al., 2001). The code computes the emission and propagation of  $\gamma$ -rays and positrons as a function of time, and follows their propagation through the ejecta. When these thermalize, optical photons are produced, whose diffusion is also followed with a Monte Carlo scheme. The optical opacity is treated with a scheme which is based on the number of effective lines as a function of abundance (Mazzali et al., 2001). This is a good approximation, as line opacity dominates SNe Ia ejecta (Pauldrach et al., 1996)<sup>1</sup>.

---

<sup>1</sup> The nebular phase modelling and bolometric LC calculations were carried out by P. Mazzali.

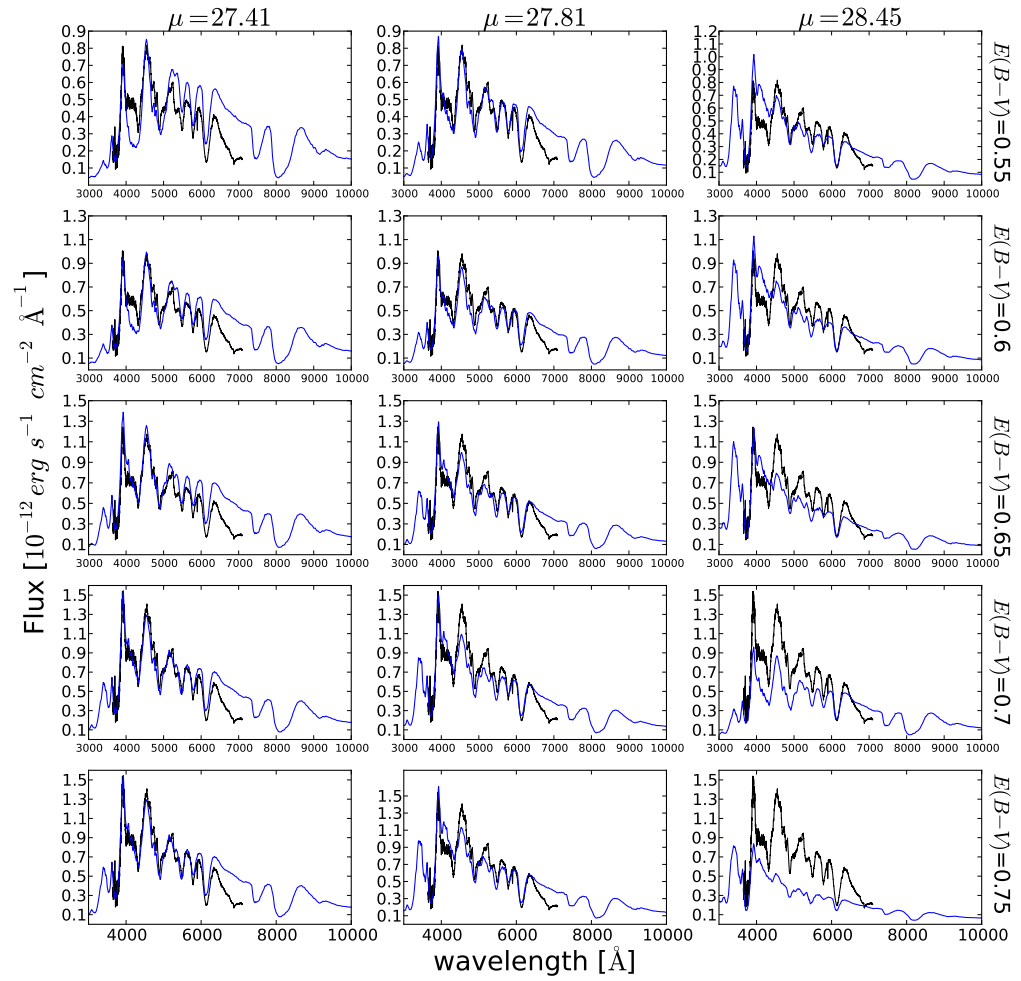


Figure 5.4: One-zone models of SN 1986G at  $B$  band maximum, using a variety of distance modulus and extinction values. The observed spectra are in black and the modelled in blue.

## 5.6 Photospheric models

### 5.6.1 Extinction and distance

The first step in modelling the photospheric spectra of a SN is to set the values for host galaxy extinction and distance. Both of these values are very uncertain for SN 1986G. A range of values have been published for the distance modulus of NGC 5128, ranging from 27.41-28.45 mag (see table 5.5). A large range of extinction values have also been quoted for SN 1986G, ranging from  $E(B - V)_{tot}=0.6$  to 0.9 mag (Nugent et al., 1995; Phillips et al., 1987), including  $E(B - V)_{tot}=0.78\pm0.07$  mag with a non standard  $R_v = 2.4$  (Taubenberger et al., 2008). Therefore, the distance to the SN and host galaxy extinction have been taken as free parameters. In the models there is some degeneracy between the distance and the extinction to the SN (Saselli et al., 2014). One-zone photospheric phase models of the spectrum at  $B$  band maximum were produced, with fixed abundances, to determine the most likely range of parameters. Figure 5.4 shows some of these one-zone models, at a range of distances from table 5.5. Extinction values range from 0.5 to 0.9 mag and were varied by intervals of 0.05 mag. The range of acceptable values was taken as  $E(B - V)_{tot}=0.6-0.7$  mag<sup>2</sup> and  $\mu = 27.41 - 27.81$  mag. For the modelling in this work a value of  $E(B - V)_{tot} = 0.65 \pm 0.5$  mag and  $\mu = 27.61 \pm 0.4$  mag were used, as these values yield the best fits. The extinction is consistent with that of Nugent et al. (1995). The distance value is in good agreement with the Cepheid distance from Ferrarese et al. (2007), who derive a distance modulus of  $27.67\pm0.12$  mag. In the modelling process it is most important to obtain the correct line ratios, line strengths, ionizations and velocities, as these are independent of extinction and yield information about the SN. It is found that other values of extinction and distance produce worse fits, even if the abundances are varied.

---

<sup>2</sup> 0.12 mag of this is from foreground galactic extinction (Schlafly & Finkbeiner, 2011)

Table 5.5: Published distances to SN 1986G.

Distance modulus ( $\mu$ )	Method	Source
$28.45 \pm 0.8$	Tully Fisher	<sup>a</sup>
$27.81 \pm 0.2$	TRGB	<sup>b</sup>
$27.67 \pm 0.12$	Cepheid	<sup>c</sup>
$27.41 \pm 0.04$	Brightest Stars	<sup>d</sup>

<sup>a</sup> Richter & Huchtmeier (1984)

<sup>b</sup> Soria et al. (1996)

<sup>c</sup> Ferrarese et al. (2007)

<sup>d</sup> De Vaucouleurs (1980)

## 5.6.2 Density profiles

Initially, SN 1986G was modelled using two density profiles, W7 and a Sub-Ch mass density profile. The W7 model was selected as SNe 2004eo, 2003du, 2002bo and 2014J can all be reasonably modelled with this density profile and variable amounts of  $^{56}\text{Ni}$ . The Sub-Ch mass density profile is an explosion with  $E_{\text{kin}} = 1.2 \times 10^{51}$  erg and a total mass of  $1.1 M_{\odot}$  (Shigeyama et al., 1992). It has a larger density at high velocities but contains less mass in the inner part of the ejecta compared to W7.

## 5.6.3 Photospheric models

The photospheric phase spectra of SN 1986G are dominated by lines of intermediate mass elements, which is consistent with the low  $^{56}\text{Ni}$  mass and rapid LC decline of the SN, and may indicate a stronger deflagration phase. This section discusses the input parameters and the properties of the synthetic spectra at each epoch. Figure 5.5 presents the synthetic spectra for the photospheric phase of SN 1986G. For both the W7 and Sub-Ch mass models a rise time to  $B$  band maximum of 18 days is adopted. This is smaller than for normal SNe Ia (e.g., Mazzali et al., 1993), but is typical for a SNe Ia with a fast LC shape. This is because the ejecta of a low-luminosity SN have a smaller opacity and a shorter photon diffusion time as they contain less NSE material

(Mazzali et al., 2001). There is very little difference between the two density profiles within the velocity range sampled by the photospheric models (7000-10000  $km s^{-1}$ ). The main differences are in the inner part of the ejecta, which is sampled by nebular phase modelling.

Figure 5.5 shows the spectral evolution of SN 1986G between 3 days before and 2 days after  $B$  band maximum. The spectra are dominated by Si II, S II, Fe II, Mg II, Ti II and Cr II lines. Ti II  $\sim 4450 \text{ \AA}$  is not typical of normal SNe Ia, where Ti is normally doubly ionised. Most of the lines from Ti III are however in the UV,  $< 3500 \text{ \AA}$ .

#### 5.6.4 -3 days

The top spectrum in Figure 5.5 was observed 3 days before  $B$  band maximum. The synthetic spectrum has a photospheric velocity of  $10000 \text{ km s}^{-1}$ , and bolometric luminosity of  $\log_{10} L = 42.55 \text{ erg s}^{-1}$ . The converged temperature of the underlying blackbody is 8900 K for the W7 density profile and 9100 K for the Sub-Ch density profile. The effective temperature ( $T_{eff}$ ) is 8600 K for the W7 density profile and 8700 K for the Sub-Ch density profile. For the W7 density profile the composition is dominated by oxygen (61% by mass), but it also requires some unburnt carbon (2% by mass), IME (Si 26%, S 6%, Ca 2%, Mg 2%), and traces of heavier metals (Ti+Cr 0.36% and Fe 0.15%). Using the Sub-Ch density profile, the synthetic spectrum is dominated by O (52% by mass), with 2% unburnt carbon. IME make up a large fraction of the ejecta (Si 25%, S 15%, Mg 2%, Ca 2%), with the rest consisting of heavier elements (Ti 2%, Cr 2.5%, Fe 0.08%).

#### 5.6.5 -2 days

The second spectrum in Figure 5.5 was modelled at 16 days after explosion. There is very little spectral evolution compared to the previous epoch. Using the W7 den-

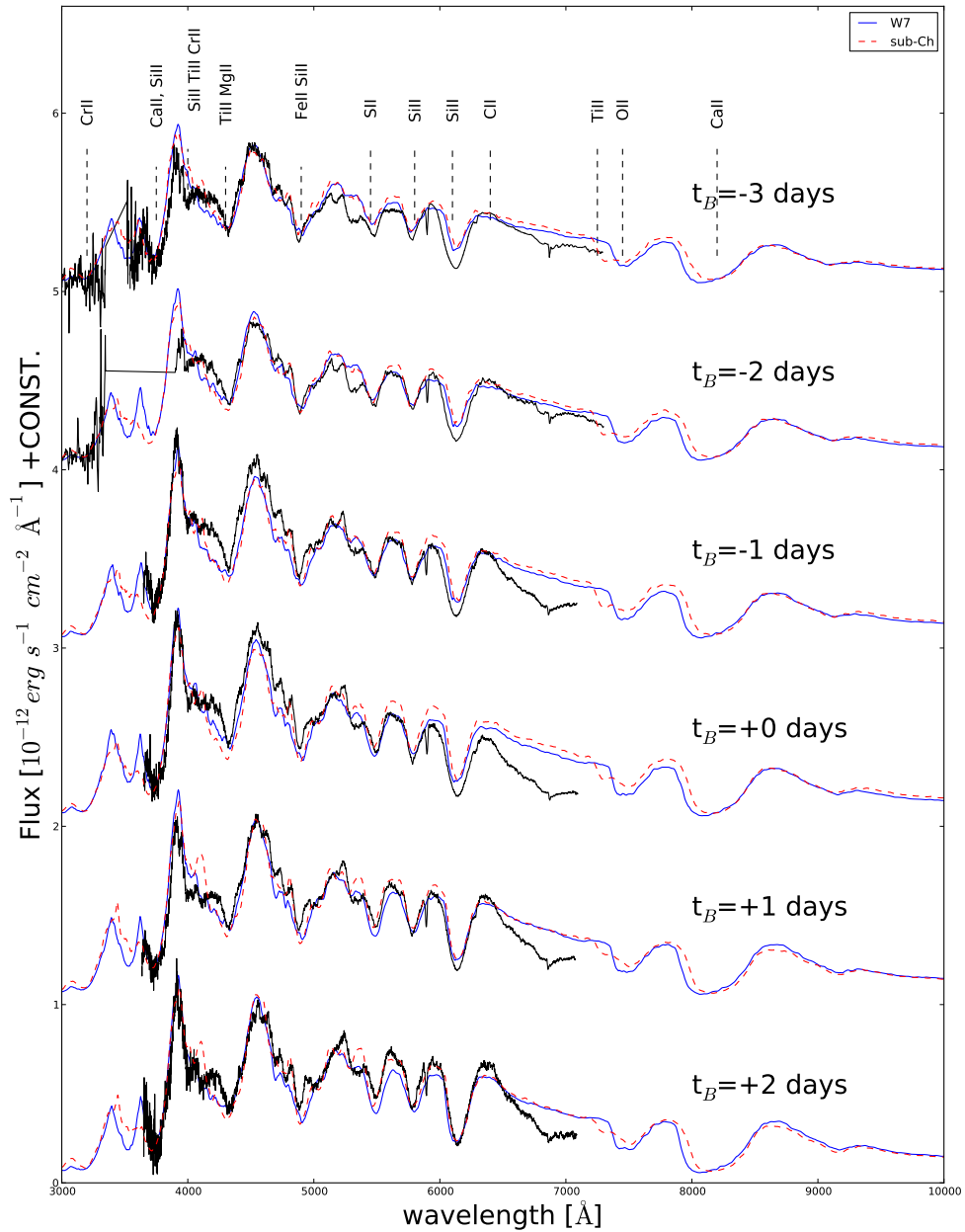


Figure 5.5: The photospheric phase models of SN 1986G, where the spectra have been shifted in flux by a constant for clarity. Models for both the W7 (blue solid) and Sub-Ch (red dashed) density profiles are shown. The spectra have been corrected for extinction.

Table 5.6: Input parameters and calculated converged black body temperatures for models from the W7 and Sub-Ch density profiles.

Epoch	velocity	Bol Lum	Temperature	velocity	Bol Lum	Temperature
$t_{rise}$	$v_{ph}$	L	$T_{BB}$	$v_{ph}$	L	$T_{BB}$
days	km s <sup>-1</sup>	logL <sub>⊙</sub>	K	km s <sup>-1</sup>	log(L <sub>⊙</sub> )	K
	W7	W7	W7	Sub-Ch	Sub-Ch	Sub-Ch
15	10000	8.960	8900	10000	8.96	9100
16	9400	8.990	9100	9200	9.00	9500
17	8800	9.040	9500	8900	9.040	9600
18	8100	9.060	10000	8500	9.070	9700
19	7800	9.050	9700	7200	9.050	10300
20	7600	9.050	9500	7000	9.050	10100

sity profile a photospheric velocity of 9500  $km s^{-1}$  is required, as well as a bolometric luminosity of  $\log_{10}L=42.57$ . The  $T_{eff}$  at this epoch is 8700 K. This spectrum is dominated by oxygen (61%), while IME make up 38% of the elements in this shell (Si 30%, S 6%, Ca, 2%). The Ti, Cr and stable Fe abundances have all increased (Ti+Cr 1.1%, Fe 0.2%), relative to the higher velocity spectrum. This is required as the Ti  $\sim 4450 \text{ \AA}$  feature progressively gets stronger over time. The IUE spectrum has been used to set the flux level in the UV and to constrain the Cr abundance.

The Sub-Ch density profile produces slightly different results. The effective temperature at this epoch is 9200 K, and the photospheric velocity is 9200  $km s^{-1}$ . This layer of the ejecta requires no carbon, and is dominated by oxygen (50%). In this shell the S abundance drops to 5%, whereas the Si abundance increases to 35%. This is unusual for a SN Ia as one would expect S to propagate to slightly lower velocities than Si as a consequence of the nucleosynthesis reaction chain described by Nomoto et al. (1984). However, the S II feature at 5640 $\text{\AA}$  is fit almost perfectly by the model at this epoch, and increasing the S abundance would worsen the fit. It should be noted that in the abundance distributions of SNe 2004eo and 2011fe the S abundance does not propagate as deep as that of Si (Mazzali et al., 2008, 2015). Using the Sub-Ch density profile the abundances of Ti+Cr (8%) and Fe (1.3%) are higher than those needed for

the W7 model. The Ti +Cr abundance is required to be this high to fit the blue edge of the 4200Å feature. Without this high abundance there is no absorption at 4100Å .

### 5.6.6 -1 days

The third spectrum in Figure 5.5 was taken at -1 day relative to *B* band maximum. This spectrum was modelled as 17 days after explosion. The synthetic spectrum produced using the W7 density profile is a very good fit to the observed one. The feature at  $\sim 4900\text{\AA}$  has resolved into separate Fe II lines, and the W7 density profile fits all of these lines at the correct velocities. The photospheric velocity at this epoch is  $8900\text{ km s}^{-1}$ , with a bolometric luminosity of  $10^{42.63}\text{ erg s}^{-1}$  and a  $T_{eff}$  of 9200 K. This shell is still dominated by oxygen, however at this epoch the abundance of oxygen is starting to decrease. The oxygen fraction is 50% by mass. The Si abundance has increased to 35%, and that of Ti+Cr to 1.5%.

The Sub-Ch model has  $v_{ph} = 8900\text{ km s}^{-1}$  and a bolometric luminosity of  $\log_{10}L=42.60$ . At this epoch oxygen still dominates at 44%, but IMEs also significantly contribute to the spectrum (Si 37%, S 5%, Ca 2%). Relative to the previous epoch the Ti+Cr abundance has decreased to 6.5%, but the Fe abundance has increased to 5%. The effective temperature at this epoch is 9400 K.

### 5.6.7 +0 days

IMEs begin to dominate the ejecta at this epoch, which is at *B* band and bolometric maximum. For the W7 model, the Si and S abundances are 65% and 13%, respectively. This spectrum was computed with a photospheric velocity of  $8100\text{ km s}^{-1}$  and a bolometric luminosity of  $\log_{10}L=42.65$ . The effective temperature at this epoch is 9700 K, while the combined Ti+Cr abundance has increased to 1.8%.

The Sub-Ch model for this spectrum has a  $\log_{10}L=42.66$  a  $v_{ph} = 8500\text{ km s}^{-1}$

and an effective temperature of 9600 K, the photospheric velocity has hardly changed compared to the previous epoch. IMEs also begin to dominate the Sub-Ch model (Si 40%, S 5%, Ca 8%).

### 5.6.8 +1 days

This spectrum was observed at +1 day relative to *B* band maximum. The photospheric velocity ( $7800 \text{ km s}^{-1}$ ) has only slightly decreased (by  $300 \text{ km s}^{-1}$ ) compared to the previous epoch. The model at the epoch has a luminosity of  $\log_{10} L = 42.64$ . Because of the small change in photospheric velocity from the previous epoch there is practically no spectral evolution. Therefore the abundances have not changed significantly. The effective temperature of this shell is 9600 K.

The Sub-Ch model at this epoch contains no S near the photosphere, although there is still 34% of oxygen left in the ejecta. This may indicate that the Sub-Ch density is not a good solution and cannot explain the mechanism and progenitor of SN 1986G. There is an increase in Fe abundance at this epoch (7%), and the Ti+Cr abundance is 4%. The effective temperature of the Sub-Ch model is 10200 K. The model at the epoch has a luminosity of  $\log_{10} L = 42.64$ , and a photospheric velocity of  $7200 \text{ km s}^{-1}$ .

### 5.6.9 +2days

The last W7 photospheric model for the spectrum at +2 days (20 days from explosion). It is shown in Figure 5.5. It has a  $v_{ph} = 7600 \text{ km s}^{-1}$ ,  $T_{eff} = 9300 \text{ K}$  and  $\log_{10} L = 42.62 \text{ erg s}^{-1}$ . This shell has 75% Si and 10% S. The Ca at this epoch is 0.3%.

The final Sub-Ch model still has a large mass of oxygen (30%), but this epoch is dominated by Si (56%). The Ti and Cr abundances have stayed constant, but the Fe abundance has increased to 8%. The effective temperature at this epoch is 10100 K.

There are some doubly ionized species in the spectrum at this time, Fe III and Cr III indicated by the features at  $\sim 5000\text{\AA}$  and  $\sim 3700\text{\AA}$  respectively. These doubly ionized species correspond to the effective temperature increase, compared to the +1 days model. The W7 model has fewer doubly ionized species.

At every epoch in the Sub-Ch model there is a deep Ti II absorption at  $\sim 7300\text{\AA}$ . This feature is not seen in the W7 models, nor in the observed spectrum, and it is produced because the Sub-Ch model has more mass at high velocities. It is another indication the Sub-Ch density profile is a poor solution compared to the W7 model. However, apart from this feature, it could be argued that the Sub-Ch density profile produces better fits. The full input parameters for the photospheric models can be found in Table 5.6. The photospheric velocity of SN 1986G is lower than would be expected for a normal SNe Ia. The photospheric phase models probe layers above  $7000\text{ km s}^{-1}$  in velocity. The bolometric luminosity of the models peak at +0 days compared to  $B$  band maximum, which is expected from a SN with a steep light curve.

## 5.7 Nebular phase models

A single nebular spectrum of SN 1986G is available, which was published by Cristiani et al. (1992) and was obtained  $\sim 256$  days after maximum. The spectrum shows the usual nebular SNIa features, strong Fe II and Fe III lines in the blue and a mix of Ca II and Fe II lines in the red. It is significantly affected by reddening, to the point of showing self-absorption in the NaID line as well as a narrow  $H\alpha$  absorption in the middle of a weak Fe II emission complex.

The abundance tomography experiment has been completed by modelling the nebular spectrum using two different density distributions: the original W7 model and the Sub-Ch model discussed above.

The nebular spectrum code which has been used in the past to model both SNe Ia (e.g. Mazzali et al., 2015) and SNe Ib/c has been used (e.g. Mazzali et al., 2007, where a more detailed description of the code can be found). The code computes the diffusion and deposition of gamma-rays and positrons produced by the radioactive decay of  $^{56}\text{Ni}$  and  $^{56}\text{Co}$  in the SN ejecta using gray opacities in a Monte Carlo scheme. The ensuing collisional heating of the SN ejecta is then balanced by cooling via line emission, following Axelrod (1980). The balance between radiation and gas properties is computed in non-local thermodynamic equilibrium (NLTE). The abundances in the ejecta were adjusted to optimise the fit, except at the velocities where abundances were determined from early-time spectral modelling. These are regions with velocities above  $7000 \text{ km s}^{-1}$ , which are not sampled by the nebular emission lines. A simple one-zone fit to the spectrum yields a model line velocity of  $5600 \text{ km s}^{-1}$ , which is also in line with the fast evolution of the light curve of SN 1986G (Mazzali et al., 1998, 2007).

The two best-fit models are shown in Figure 5.6. Although the models are overall quite similar in the kind of emission lines that are predicted, there are significant differences which can help us discriminate between them. The individual models are discussed in turn.

The W7 model (dashed/blue line) produces a good match in particular to the blue part of the spectrum. A  $^{56}\text{Ni}$  mass of  $0.13 M_{\odot}$  is required. Because the inner region in W7 is quite dense, material other than  $^{56}\text{Ni}$  must be used to fill it. Stable Fe-group elements are produced in the centre of Chandrasekhar-mass explosions, and it is found that a total mass of about  $0.11 M_{\odot}$  is required. This is dominated by stable Fe. Stable Fe-group material is important as it acts only as a coolant, so its presence contributes to balancing the heating from radioactive decay and to keeping the ionization ratio (in particular Fe III/Fe II) close to the observed value. The mass included within a velocity of  $5600 \text{ km s}^{-1}$  in W7 is  $\sim 0.4 M_{\odot}$ , and NSE material does not reach this

value. The remaining mass is attributed to intermediate-mass elements, in particular Si, which leads to a strong predicted emission in the NIR, near  $1.6\mu\text{m}$ . The line near  $5900\text{ \AA}$  is predominantly NaID. The strong emission near  $7300\text{ \AA}$  is well reproduced as a combination of Fe II and Ca II with a minor contribution from Ni II. The narrowness of the emission lines leads to the observed split between the two features. In fact, a hint of a split can be seen even in the emission feature near  $5200\text{ \AA}$ . This is due just to lines separating out, as in, e.g., SN 2003hv (Mazzali et al., 2011), and not to double peaks caused by the morphology of the explosion. Other Fe II lines are not well reproduced, however. In particular, the feature near  $6600\text{ \AA}$  is too weak in the model, while the broad blend near  $9000\text{ \AA}$  is too strong. These shortcomings are seen in most of the SN Ia models produced with this code, but to a much lesser degree (e.g. Mazzali et al., 2015). They may partially depend on uncertain collisional rates, and they indicate that the  $^{56}\text{Ni}$  mass may be slightly overestimated. On the other hand, the extreme deviation of the redder lines in SN 1986G may also indicate problems with the density structure (see e.g. Mazzali et al., 2011), or issues with the red part of the observed spectrum. Note that in a well-observed SN Ia like SN 2011fe the ratio of the Ca-Fe emission near  $7300\text{ \AA}$  and that of the Fe complex near  $9500\text{ \AA}$  is  $\sim 1$ . In the spectrum of SN 1986G, after correcting for reddening, the ratio is  $\sim 2$ , but our model has a ratio of  $\sim 1$ . Unfortunately no other nebular spectrum is available of either SN 1986G or of SNe that closely resemble it, so this cannot be verified.

The Sub-Ch model (green line) shown in figure 5.6, has several problems, compared to the W7 one. Primarily, the ionization of Fe is too high. This is shown by the excessive strength of the emission near  $4700\text{ \AA}$  when the model matches that at  $5200\text{ \AA}$ . Note that the model displayed is reddened, which depresses the bluer feature significantly. This behaviour was seen in a peculiar SN, SN 2003hv (Mazzali et al., 2011), and was interpreted there to indicate low densities at low velocities, which is

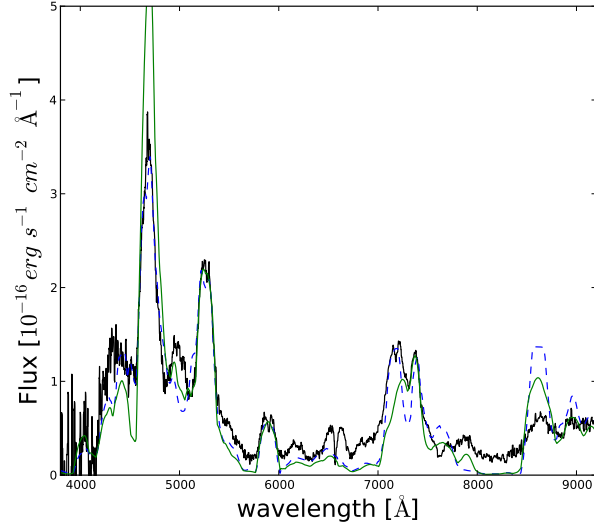


Figure 5.6: The nebular phase models of SN 1986G. The blue spectrum was obtained using a W7 density profile and the green spectrum using the Sub-Ch profile. The black line is the observed spectrum. The spectra have been corrected for extinction.

exactly what a Sub-Ch model predicts, and a consequent lack of stable NSE material, leading to insufficient cooling and hence recombination. The Fe II lines in the red are actually depressed relative to the line at 5200 Å. The model contain an ejecta mass of only  $\sim 1 M_{\odot}$ . Most of the missing mass is stable NSE material, the mass of which has gone down to  $0.1 M_{\odot}$ , mostly stable Fe at intermediate velocities. Intermediate-mass elements just above the  $^{56}\text{Ni}$  zone again lead to strong Si emission in the NIR. The incorrect ratio of the optical Fe lines is a strong argument against this model, which is not favoured.

## 5.8 Abundance tomography

Figures 5.7 and 5.8 show the abundance distributions of SN 1986G as a function of velocity and enclosed mass. At velocities below  $7000 \text{ km s}^{-1}$  the nebular modelling determines the distribution, and at velocities above  $7000 \text{ km s}^{-1}$  the photospheric mod-

els determine the distribution. Above  $\sim 12000 \text{ km s}^{-1}$  certain aspects of the distribution can be inferred, but this is where the results are most uncertain because early data are not available. However, incorrect abundances in the outer layers can make it impossible to produce a good synthetic spectrum in the inner layers, so it can be assumed that the description of the outer layers is not completely unreasonable.

Figure 5.7 is the abundance distribution produced using the W7 density profile. An upper limit to the abundance of carbon is set to a mass of  $0.02 M_{\odot}$ . All of this progenitor carbon is at high velocities,  $> 10000 \text{ km s}^{-1}$ . The outer layers of the ejecta are dominated by oxygen, which is seen throughout the whole of the photospheric phase, but the part of the observed spectra where the oxygen would be expected to be,  $\sim 7500 \text{ \AA}$ , was not observed. It is reasonable to infer a high oxygen abundance in SN 1986G, because of its similarities with 91bg-like SNe, which show a strong oxygen feature. Furthermore, the fact that carbon is detected in the spectra is a good indication that oxygen will be present between layers where the carbon and IME dominate. The final masses from the W7 abundance distribution can be found in Table 5.7. Masses have been quoted to the second decimal place, but does not mean accuracy to this degree. It is required as there are elements which do not have a mass greater than  $0.1 M_{\odot}$ . IMEs dominate the abundance distribution of the SN at intermediate velocities. The S distribution follows the Si distribution at velocities down to  $\sim 7000 \text{ km s}^{-1}$ , with a lower ratio than traditionally would be expected. The typical ratio of Si to S is 3 to 1. The S abundance drops to 0 at  $v \sim 6000 \text{ km s}^{-1}$ . The enclosed mass range in which Si dominates is from  $0.75 M_{\odot}$  to  $0.19 M_{\odot}$ . This is very different from SN 1991T, which sits at the opposite end of the ‘Phillips Relation’, where Si dominates only in the enclosed mass range of  $\sim 1.05 M_{\odot}$  to  $1.07 M_{\odot}$  (Saselli et al., 2014). The large amount of Si in SN 1986G corresponds to a small amount of  $^{56}\text{Ni}$  being produced in the explosion (Mazzali et al., 2007). This agrees with SN 1986G having a low luminosity and partial

burning. There is no evidence for mixing of  $^{56}\text{Ni}$  to high velocities for SN 1986G. A  $^{56}\text{Ni}$  mass of  $0.13 M_{\odot}$  is obtained from the abundance distribution. Most  $^{56}\text{Ni}$  is located in the denser inner layers. At velocities between  $1000 \text{ km s}^{-1}$  and  $\sim 3500 \text{ km s}^{-1}$  Fe and  $^{56}\text{Ni}$  dominate the ejecta. The innermost layers of the SN 1986G W7 density profile model are dominated by stable Ni, and  $^{56}\text{Ni}$  is further out in the ejecta, between an enclosed mass of  $\sim 0.1$  and  $\sim 0.55 M_{\odot}$ . This is consistent with the burning that a fast deflagration such as that of a W7-like model predicts. The Ti+Cr abundances peak in the velocity range  $8000\text{-}9000 \text{ km s}^{-1}$ . Their combined integrated mass is of the order of  $0.01 M_{\odot}$ .

The abundance distribution produced using the Sub-Ch density profile is dramatically different from that of the W7 density profile, as shown in Figure 5.8. The total C mass is  $0.04 M_{\odot}$ . There is evidence for carbon down to an enclosed mass of  $\sim 0.7 M_{\odot}$ . The outer layers consist almost entirely of oxygen. The oxygen zone is large compared to a normal SN Ia. Oxygen dominates down to  $6000 \text{ km s}^{-1}$ , and is present down to velocities as low as  $4000 \text{ km s}^{-1}$  with abundances of the order of 20%. Between  $6000 \text{ km s}^{-1}$  and  $4000 \text{ km s}^{-1}$  IMEs dominate, and NSE material dominates the inner layers of the ejecta. The total amount of  $^{56}\text{Ni}$  in the ejecta of SN 1986G, assuming a Sub-Ch density profile, is  $0.11 M_{\odot}$ . The abundance distributions produced using the Sub-Ch model imply that this explosion scenario is not a valid one for SN 1986G. Oxygen probes to deeper layers of the ejecta than sulphur, which is in direct conflict with nucleosynthesis calculations and expected results. The zone where IMEs dominate has an unusually small velocity range of  $500 \text{ km s}^{-1}$ . Overall, the abundance yields and distribution from the Sub-Ch model do not agree with nucleosynthesis and explosion models.

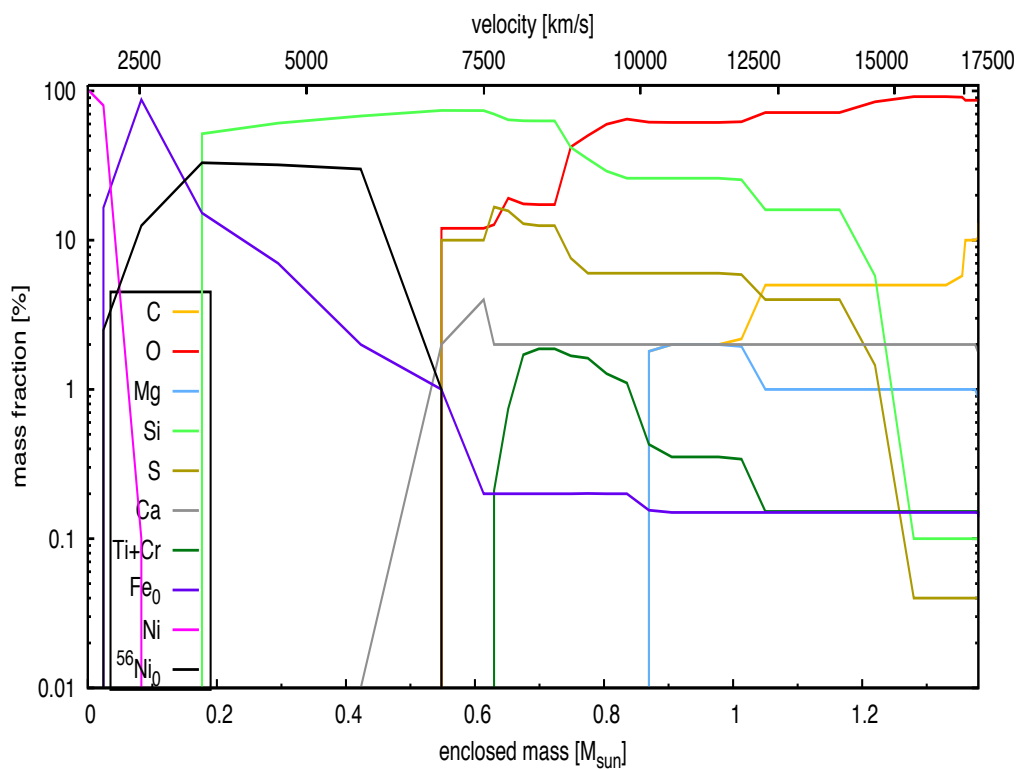


Figure 5.7: The abundance distribution of SN 1986G obtained with the W7 density profile.

Table 5.7: Integrated abundances from the full abundance tomography modelling of SN 1986G. The errors on the masses are  $\pm 25\%$ , except for  $^{56}\text{Ni}$  which has an error of  $\pm 10\%$ .

Element	W7	Sub-Ch
	$M_{\odot}$	$M_{\odot}$
C	0.02	0.04
O	0.49	0.51
Mg	<0.01	<0.01
Si	0.50	0.26
S	0.05	0.04
Ca	0.02	0.01
Ti+Cr	0.01	0.02
Fe	0.11	0.09
$^{56}\text{Ni}$	0.13	0.11
Ni	0.04	0.01
$M_{tot}$	1.38	1.11

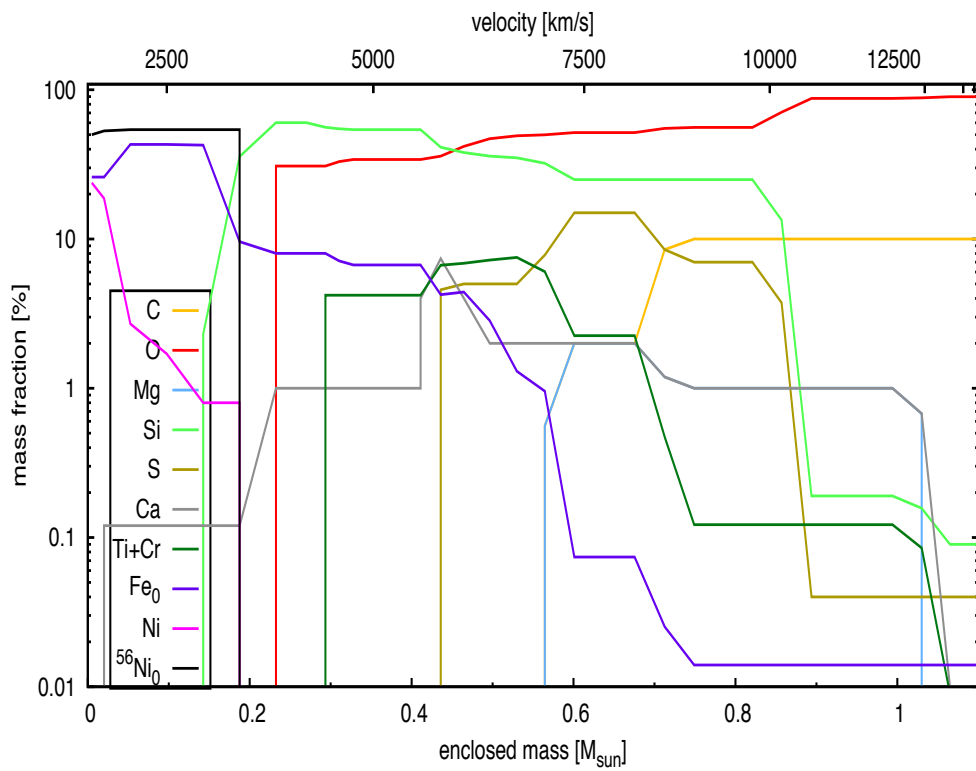


Figure 5.8: The abundance distribution of SN 1986G obtained with the Sub-Ch density profile.

## 5.9 A consistent, reduced-energy model

### 5.9.1 Energy estimates

With the integrated masses obtained from the abundance tomography modelling, the kinetic energy of the explosion can be derived, using equation 1.2. It is found that the  $E_{\text{kin}}$  of the explosion is  $0.8 \times 10^{51}$  erg, using the masses derived by the W7 density profile model<sup>3</sup>. The  $E_{\text{kin}}$  calculated from the abundances obtained using the W7 density profile is smaller than the value for the standard W7 explosion, which has  $E_{\text{kin}} = 1.3 \times 10^{51}$  erg. Therefore, there is a discrepancy between the input density profile and the  $E_{\text{kin}}$  derived from the nucleosynthesis. This discrepancy is an issue if one wants to solve the progenitor scenario and explosion mechanism of SN 1986G. For the Sub-Ch density model,  $E_{BE} = 0.21 \times 10^{51}$  erg (Yoon & Langer, 2005), which equates to a  $E_{\text{kin}}$  of  $0.55 \times 10^{51}$  erg (the  $E_{\text{kin}}$  of the Sub-Ch explosion model that we used is  $1.2 \times 10^{51}$  erg), so again the model has a larger  $E_{\text{kin}}$  than that inferred from nucleosynthesis.

Therefore an attempt is made to develop a density profile that both fits the spectra and is consistent with nucleosynthesis. Given what is discussed above, this has to be a low energy density profile. In this section such a profile will be built and tested. This is done by scaling the W7 density profile to a lower  $E_{\text{kin}}$  using equations 5.3 and 5.4.

$$\rho' = \rho_{W7} \left( \frac{E'}{E_{W7}} \right)^{-\frac{3}{2}} \cdot \left( \frac{M'}{M_{W7}} \right)^{\frac{5}{2}} \quad (5.3)$$

$$v' = v_{W7} \left( \frac{E'}{E_{W7}} \right)^{\frac{1}{2}} \cdot \left( \frac{M'}{M_{W7}} \right)^{-\frac{1}{2}} \quad (5.4)$$

In these equations  $\rho'$  is the new density,  $\rho_{W7}$  is the W7 density,  $E'$  is the energy

---

<sup>3</sup> For a Chandrasekhar mass WD  $E_{BE} = 0.46 \times 10^{51}$  erg.

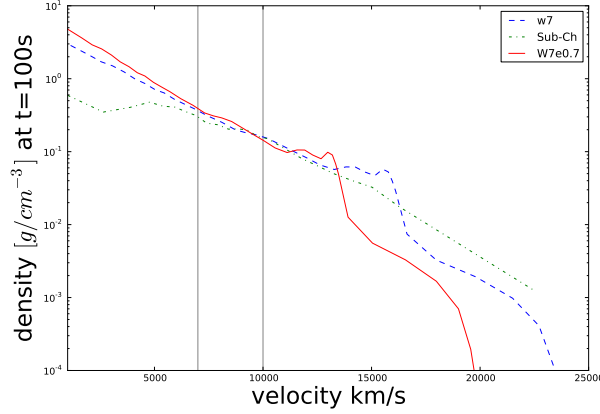


Figure 5.9: The W7, Sub-Ch and W7e0.7 density profiles as a function of velocity at  $t=100$  s after explosion. The vertical grey lines show the range in values  $v_{ph}$  can take, for the -3 d to +2 d models.

of the new density profile,  $E_{W7}$  is the energy of the W7 density profile,  $M'$  is the mass of the new density profile and  $M_{W7}$  is the mass of the W7 density profile,  $v_{W7}$  is the velocity of the W7 density profile, and  $v'$  is the velocity of the new profile.

The density profile was scaled keeping the mass at the Chandrasekhar mass and scaling the energy to 70% of that of the W7 density profile to match the  $E_{kin}$  inferred from the nucleosynthesis, and for convenience it is called W7e0.7. This rescaling has been shown to work well for SN 2005bl. However, this SN was only modelled in the photospheric phase (Hachinger et al., 2009), as late-time spectra were not available. Therefore, placing the mass in the inner layers may not have been the perfect solution (see Mazzali et al., 2011). In contrast, SN 1986G has good nebular data, so it is possible to tell if this increase in central density can be a realistic solution.

Figure 5.9 shows the W7, Sub-Ch and W7e0.7 density profiles at  $t=100$  s after the explosion. Compared to W7, the Sub-Ch density profile has more mass at higher velocities and a lower central density, whereas the W7e0.7 model has a higher central density and less material at high velocities, and hence a smaller  $E_{kin}$ . To decrease the energy in the W7 model, the mass which was removed from the high velocities was

redistributed to the inner part of the ejecta.

### 5.9.2 Photospheric-epoch models

Figure 5.10 shows the synthetic spectra produced with all three density profiles at  $-3$  days relative to  $B$  band maximum. The green line is the W7e0.7 model. This model fits the data (black line) very well, the Si II line ratio is correct, and the sulphur and Fe features are fit almost perfectly. The fact that the W7e0.7 density profile produces a good fit is reason for the full abundance tomography analysis to be carried out using the W7e0.7 density profile, with the aim of getting a consistent model.

The full photospheric models obtained with the new, W7e0.7, density structure are presented in Figure 5.11. The models were remade using the same input parameters as those for the W7 model in Table 5.6. The only elements which changed in abundance, in velocity space, were Ti+Cr, with their mass fraction increasing to  $\sim 3\%$  at  $8000 \text{ km s}^{-1}$ . In the W7e0.7 spectra, the ratio of the strongest Si II features ( $6355$  and  $5970 \text{ \AA}$ ) has improved and the Ti  $4450 \text{ \AA}$  feature fits significantly better. These improvements could be caused by the bump in the density profile moving inwards in velocity space. This causes there to be an increase in density closer to the photosphere. This bump is still in the oxygen zone, but there is also an increase in the Si abundance. The improvements are also due to a lack of material at high velocities. It is apparent that a steeper density than the standard W7 model is required above  $12500 \text{ km s}^{-1}$ .

### 5.9.3 Carbon

From Figure 5.5 it is apparent at  $-3$  and  $-2$  days that there is some C II in the spectra, at  $\sim 6350 \text{ \AA}$ . As there are no observed spectra before  $-3$  days it is not possible to put an exact constraint on the amount of unburnt carbon in the ejecta, therefore the next part of the analysis attempts to constrain an upper limit on the C abundance. The synthetic

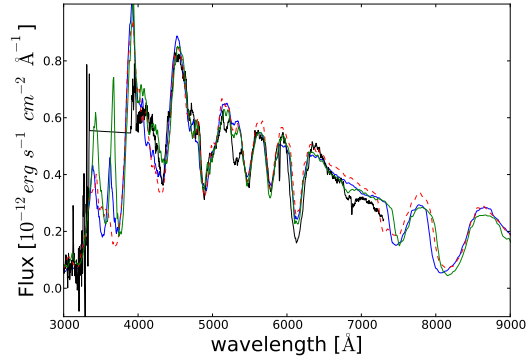


Figure 5.10: One-zone models at -3 days relative to  $B$  band maximum. The synthetic spectra were produced using the W7 (blue), W7e0.7 (green) and Sub-Ch (red dashed) density profiles. The spectra have been corrected for extinction.

spectra produced using the W7e0.7 density profile has 3 synthetic shells based above the -3 days,  $10000 \text{ km s}^{-1}$ , outer shell. The purpose of having these synthetic layers is to produce a stratified abundance distribution. If the distribution is not stratified the model spectra will produce a poor fit. Figure 5.12 shows the -3 day spectrum over a wavelength range of  $6200\text{--}6600 \text{ \AA}$ , where unburnt carbon would be seen in the ejecta. In order to produce the best fit of this C II feature the W7e0.7 model requires a carbon abundance of 13% at  $23000 \text{ km s}^{-1}$ , 10% at  $17550 \text{ km s}^{-1}$ , 5% at  $12000 \text{ km s}^{-1}$  and 2% at  $10000 \text{ km s}^{-1}$ . Increasing the  $12000 \text{ km s}^{-1}$  layer to an abundance of 12% produces the green line in Figure 5.12, and having zero carbon in the ejecta produces the blue line in Figure 5.12, both of which yield a worse fit. When determining the best fit it is important to only examine the spectra between  $6300\text{--}6450 \text{ \AA}$  as this is where the C II  $\lambda 6578$  and  $\lambda 6582$  lines will be seen, blue-ward of this is Si II absorption and red-ward is continuum. The integrated carbon mass abundance from the best fit using the W7e0.7 density profile is  $0.02 M_{\odot}$ .

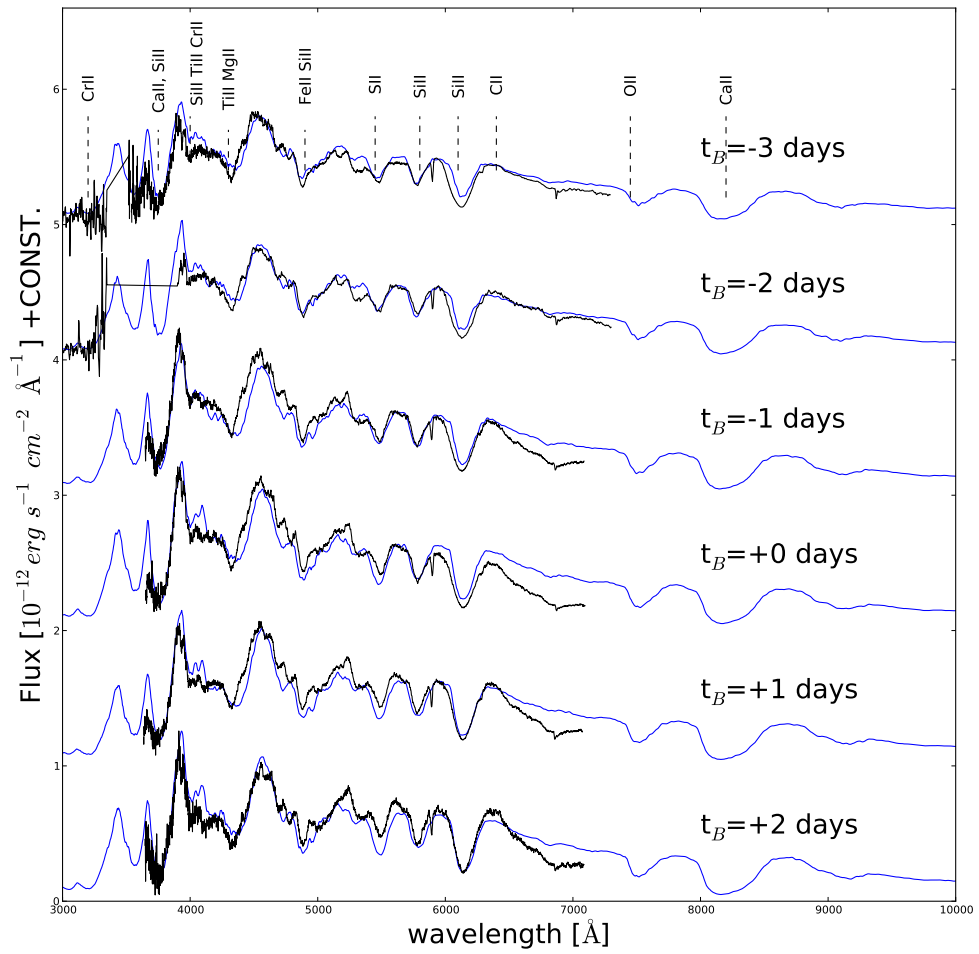


Figure 5.11: The photospheric phase models of SN 1986G, calculated using the W7e0.7 density profile. The blue line are the models and the black line the observed spectra. The spectra have been corrected for extinction.

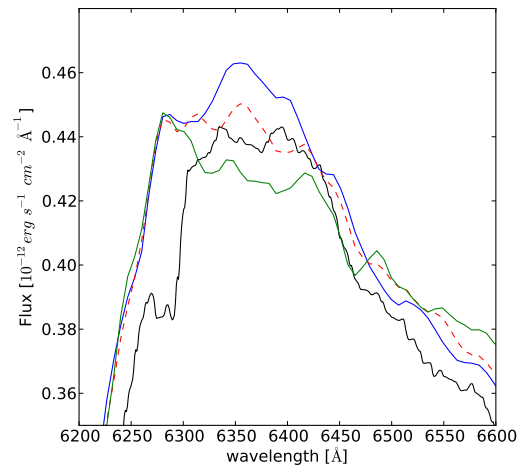


Figure 5.12: Synthetic spectrum at -3 days produced using the W7e0.7 density profile to constrain an upper limit on carbon. The blue line is the model with 0% of C, the red dashed line with the 2% C and the green line with 10% C at the photosphere. The black line is the observed spectra.

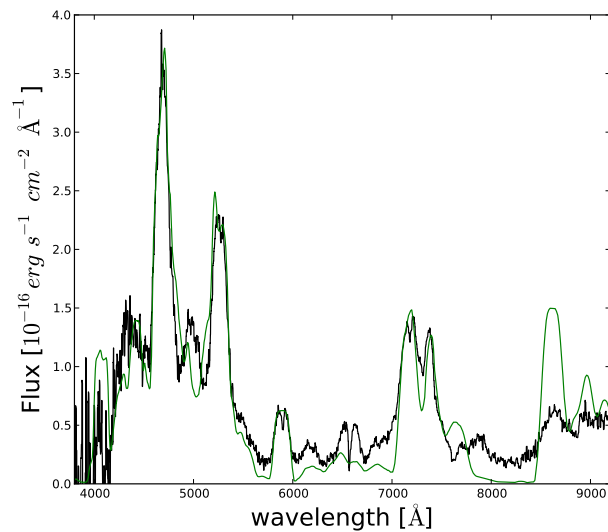


Figure 5.13: The nebular phase models of SN 1986G. The green line is the model calculated using the W7e0.7 density profile. The spectra have been corrected for extinction.

### 5.9.4 Nebular-epoch model

A nebular phase model was produced using the W7e0.7 density. It is shown as a green line in Fig. 5.13. This density profile has more mass at low velocity ( $\sim 0.50 M_{\odot}$  within  $5600 \text{ km s}^{-1}$  as opposed to  $\sim 0.40$  for W7). The  $^{56}\text{Ni}$  mass is now  $\sim 0.14 M_{\odot}$ , but the higher density at low velocities results in a larger mass of stable NSE material,  $\sim 0.21 M_{\odot}$ , most of which is stable Fe. This is in line with Mazzali et al. (2007). The additional cooling provided by the stable NSE material leads to the correct reproduction of the Fe II/Fe III line ratio in the blue, but it does not solve the problem of the excessive Fe II emission in the red, where the synthetic spectrum predicts excessively strong lines. As is argued above, there may be a problem with our model, but also with the redder part of the observed spectrum itself. Nebular-epoch observations of SN 1986G-like SNe are encouraged in order to assess the reality of the red flux.

### 5.9.5 Abundance stratification

The abundance stratification of the W7e0.7 model can be seen in Figure 5.14. The oxygen layer dominates the ejecta down to velocities of  $\sim 9000 \text{ km s}^{-1}$ . IMEs dominate the bulk of the ejecta at velocities between  $\sim 9000 \text{ km s}^{-1}$  and  $\sim 3500 \text{ km s}^{-1}$ . Below  $\sim 3500 \text{ km s}^{-1}$  NSE material dominates, with the ejecta consisting entirely of stable Ni in the innermost  $1000 \text{ km s}^{-1}$ .  $^{56}\text{Ni}$  is more evenly distributed than in the W7 model. The  $^{56}\text{Ni}$  abundance peaks at 40% in the velocity range  $4000 - 6000 \text{ km s}^{-1}$ . It is also seen in the ejecta down to a velocity of  $1000 \text{ km s}^{-1}$ . In the models produced using the W7 and Sub-Ch density profiles, oxygen probes to deeper layers of the ejecta than sulphur, which is in direct conflict with SNe Ia nucleosynthesis calculations and explosion models (Iwamoto et al., 1999). However, in the W7e0.7 model sulphur is re-

Table 5.8: Integrated abundances for the W7e0.7 models. The errors on the masses are  $\pm 25\%$ , except for  $^{56}\text{Ni}$  which has an error of  $\pm 10\%$ .

Element	W7 E70% $M_{\odot}$
C	0.01
O	0.33
Mg	<0.01
Si	0.58
S	0.09
Ca	0.01
Ti+Cr	0.01
Fe	0.18
$^{56}\text{Ni}$	0.14
Ni	0.02
$M_{tot}$	1.38

quired down to a velocity of  $\sim 4000 \text{ km s}^{-1}$ , and oxygen is only seen down to velocities of  $\sim 6000 \text{ km s}^{-1}$ , so the problem no longer exists.

The abundance distribution from the W7e0.7 model produces physically sensible results, as well as good fits between the observed and synthetic spectra. The integrated masses obtained using this density profile can be found in Table 5.8. The Ni mass is  $0.14 M_{\odot}$ , with IMEs making up  $0.69 M_{\odot}$  and  $0.34 M_{\odot}$  of unburnt material. Using equation 1.1 the kinetic energy of the ejecta can be calculated. The  $E_{\text{kin}}$  calculated using this method is  $0.97 \times 10^{51} \text{ erg}$ , which is consistent with the energy of the W7e0.7 density profile ( $0.9 \times 10^{51} \text{ erg}$ ).

## 5.10 Bolometric Light curves

### 5.10.1 Observed light curve

A bolometric light curve of SN 1986G in the range 3000-24000 Å has been constructed, using the optical and NIR photometry, and the well-monitored SN Ia 2004eo as a proxy.

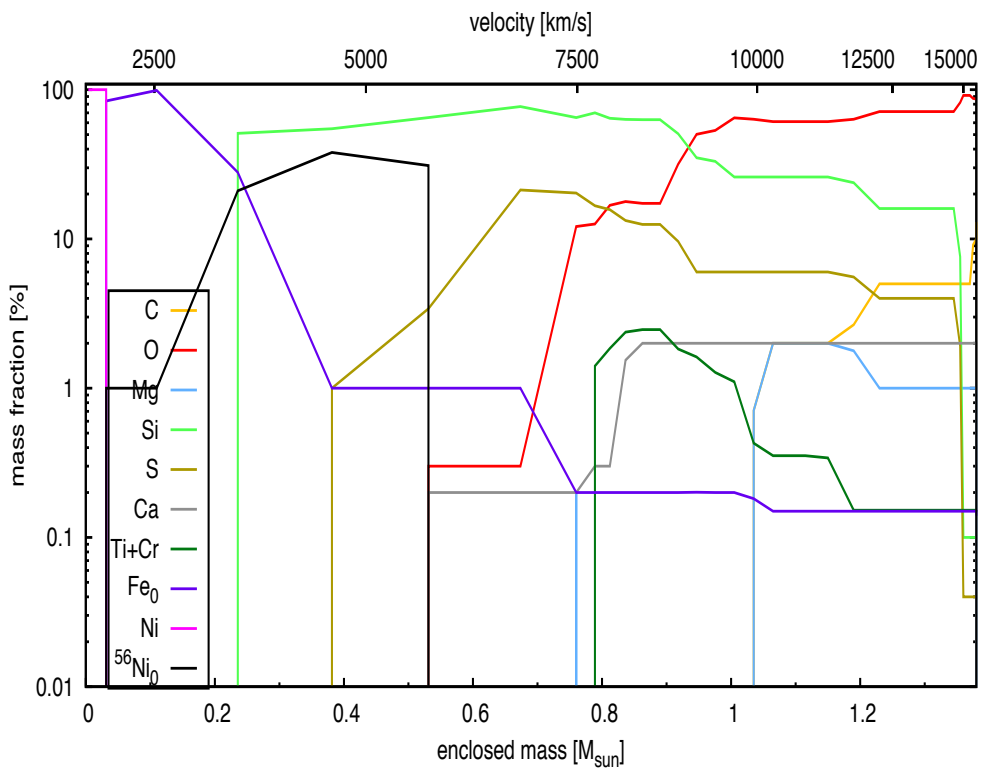


Figure 5.14: The abundance distribution of the ejecta of SN 1986G obtained using the W7e0.7 density profile.

As a first approach, the optical ( $UVB$ ) and NIR ( $JHK$ ) light curves of SN 1986G are dereddened using  $E(B - V)_{tot} = 0.65$  mag and the extinction curve of Cardelli et al. (1989). These points are then splined with a time resolution of 1 day and constructed daily spectral energy distributions in the above wavelength interval using the flux zero-points of Fukugita et al. (1995). For each epoch, the flux between the  $U$  and  $K$  bands is integrated after interpolating the flux between the central wavelengths of the filters, and added at the blue and red boundaries of the interval the fluxes obtained by extrapolating the spectrum with a flat power-law to 3000 and 24000 Å, respectively. The final bolometric LC is then resampled to the epochs of the actual V-band observations.

The lack of significant coverage in  $R$  and  $I$  bands (only a couple of points are available in each of these bands) represents a serious drawback, because the interpolation between  $V$  and  $J$  bands overestimates the  $R$  and  $I$  flux. Therefore, the final bolometric LC must be considered as an upper limit to the “real” one (which I will call ‘ $UL_{bol}86G$ ’). On the other hand, if I only integrate separately the flux in  $UBV$  and in  $JHK$  filters over the 3000-6000 Å and 10000-24000 Å ranges, respectively, and sum these two broad-band fluxes, I neglect completely the flux contribution in  $R$  and  $I$  bands, so that the resulting bolometric LC must be considered as a lower limit of the true one (‘ $LL_{bol}86G$ ’). Clearly, the real bolometric LC must be somewhere between  $UL_{bol}86G$  and  $LL_{bol}86G$ .

To evaluate the necessary bolometric corrections in the most rigorous way possible and thus to obtain a reliable estimate of the bol LC of SN 1986G, SN Ia 2004eo has been used, as it had good coverage in all bands between  $U$  and  $K$  (Pastorello et al., 2007; Mazzali et al., 2008), as is a plausible analogue of SN 1986G. Since  $U$  and  $JHK$  bands coverage for SN 2004eo is only available after maximum, the flux is reconstructed in these bands before maximum assuming that the  $U - B$ ,  $J - I$ ,  $H - I$  and  $K - I$  colours before maximum are constant and equal to the values they have at

maximum. The  $UBVRIJHK$  light curves of SN 2004eo, dereddened with  $E(B - V) = 0.109$ , were splined with a time resolution of 1 day, and spectral energy distributions were constructed and integrated over the range 3000-24000 Å, as for SN 1986G. This is the reference bolometric light curve, which will be called the ‘template’ bolometric LC.

Two more bolometric light curves were constructed for SN2004eo in the same wavelength intervals as ULbol86G and LLbol86G above, and ignoring the  $R$  and  $I$  bands: first I interpolated the spectral flux between  $V$  and  $J$  - this will be called ULbol04eo - and then summed the spectral flux in the  $UBV$  filters (3000-6000Å) and in the  $JHK$  filters (10000-24000Å). This bolometric LC will be called LLbol04eo. Bolometric corrections for SN 2004eo with respect to the ‘template’ were computed by simply differencing the template and its upper ( $UL_{bol04eo}$ ) and lower ( $LL_{bol04eo}$ ) limits. Then, these differences were applied, with their signs, to the limits obtained for SN 1986G,  $UL_{bol86G}$  and  $LL_{bol86G}$ , so that 2 ‘corrected’ bolometric LCs for SN 1986G were obtained. The ‘real’ bolometric LC of SN 1986G was obtained by averaging these 2 ‘corrected’ bolometric light curves <sup>4</sup>.

### 5.10.2 Synthetic light curve

In the spirit of abundance tomography, the density distributions and the abundances derived through synthetic spectra fitting are combined and a bolometric light curve is computed, which is compared to the one constructed based on the observed SN photometry. A Monte Carlo code (Cappellaro et al., 1997) is used which computes the emission of gamma-rays and positrons following the radioactive decay of  $^{56}\text{Ni}$  and  $^{56}\text{Co}$  and their deposition in the ejecta. The  $^{56}\text{Ni}$  distribution is derived from the spectral fitting. Gamma ray deposition is computed with a grey opacity of  $0.027 \text{ cm}^2 \text{ g}^{-1}$ ,

---

<sup>4</sup> The observed bolometric LC was computed by E. Pian.

and for positrons a grey opacity of  $7 \text{ cm}^2 \text{ g}^{-1}$  is used.

After deposition of the gamma-ray and positron energy, the resulting energy is assumed to be thermalised and energy packets representing photons are then followed as they propagate through the SN ejecta. The opacity they encounter is assumed to be dominated by line opacity and is parametrised according to the relative abundances at different depths according to the number of active lines as in Mazzali (2000):

$$\kappa = 0.25Ab(Fe - gp) + 0.025 \times (1 - Ab(Fe - gp))$$

The results for the different models are shown in Figure 5.15 along with the observationally derived bolometric light curve. At peak, the Sub-Ch model (red/dot-dashed line) reaches maximum within 12-13 days, which appears to be a short time compared to the observed light curve. The early declining part of the light curve also happens too early in this model, but then at epochs between 60 and 300 days this model follows the data reasonably well, although it underestimates the luminosity because of the low gamma ray depositions. At late times, the light curve matches the data at 275 days, and is again too low later on, but at these epochs the observed light curve declines unusually slowly.

Both Chandrasekhar-mass models, on the other hand, reach maximum after about 17-18 days, which is in line with the observed light curve and the results from spectroscopic modelling. These models also follow the early light curve decline quite well, but then are more luminous than the observed light curve by almost a factor of 2 after about day 60. At late times they finally rejoin the observed light curve, but they have a different slope. Looking in more detail, the low-energy model (purple/continuous line) is somewhat more luminous than the W7 model (green/dashed line) after day 60, because of the enhanced gamma-ray deposition resulting from the higher densities in the more slowly expanding ejecta. This difference is however quite small, such that neither model can be favoured over the other. The indications for a low energy from

spectral fitting are therefore not disproved by the light curve model.

The real issue is the behaviour of the light curve, first after 60 days and then at late times. The steep decline after day 60 is not in line with the behaviour of other SNe Ia, (Mazzali et al., 2007, e.g. SN 2004eo), which suggests that the IR contribution is not known. The range of possible corrections does in fact allow a much higher luminosity. At the latest times the decline is quite slow, possibly indicating incorrect background subtraction. The one point when spectra are available still suffers from the lack of IR information. Again, observations of a modern 1986G-like SN Ia would be needed to improve both the data coverage and the modelling results.

Overall, the results still indicate that a low-energy Chandrasekhar-mass model is favoured over an undermassive model, which may come somewhat as a surprise given that SN 1986G showed quite a rapidly evolving light curve. The rapid light curve evolution is the result of the low opacity, as a consequence of the low NSE element abundance ( $\sim 0.35M_{\odot}$ ).

## 5.11 Conclusions

A full theoretical spectral analysis of SN 1986G has been performed, using the ‘abundance tomography’ approach. SN 1986G bridges the gap between a normal and sub-luminous SN Ia. It is found that the ejecta of SN 1986G have a low temperature and are dominated by singly ionised IMEs. Three density profiles were tested, a standard Chandrasekhar mass fast deflagration (W7) density profile, a low energy Chandrasekhar mass deflagration (W7e0.7) density profile and a Sub-Chandrasekhar mass detonation density profile (Sub-Ch).

The Sub-Ch models produce good photospheric phase synthetic spectra, but this density profile can be ruled out owing to the unrealistic abundance distribution and

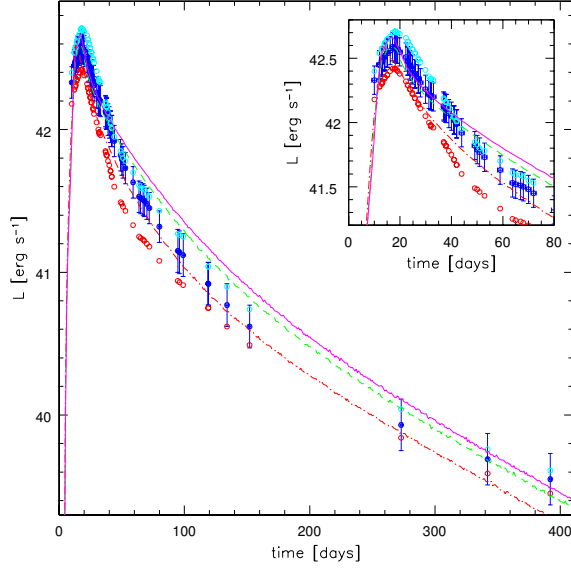


Figure 5.15: The observed (blue dots) bolometric light curve with the upper (cyan markers) and lower (red markers) limits. As well as the modelled LC using the derived abundance distribution from the W7 (green), Sub-Ch (red) and W7e0.7 (purple) density profiles.

poor synthetic nebular spectra. Furthermore, the W7 density profile is found to not be the ideal solution to explain the explosion of SN 1986G. There is no consistency between the  $E_{\text{kin}}$  implied by the density distribution ( $1.3 \times 10^{51}$  erg) and that calculated using the abundance distribution ( $0.8 \times 10^{51}$  erg).

It was found that a low energy W7 profile (W7e0.7) produced the best results. The fact that the W7e0.7 model yields a sensible abundance distribution and a consistent model demonstrates that any deviation from this mass should be minor. The final integrated masses of the various elements that were obtained from the W7e0.7 model are: O+C=0.34  $M_{\odot}$ , IME=0.69  $M_{\odot}$ , stable NSE=0.21  $M_{\odot}$  and  $^{56}\text{Ni}$ =0.14  $M_{\odot}$ . These abundances produce a  $E_{\text{kin}}$  of  $0.97 \times 10^{51}$  erg, which is consistent with the energy of the W7e0.7 density profile ( $0.9 \times 10^{51}$  erg).

In conclusion, SN 1986G is a low-energy Chandrasekhar mass explosion of a C+O WD, which produced a small amount of  $^{56}\text{Ni}$  and a large amount of IMEs. The spectra of SN 1986G show signs of progenitor C II as late as -3 days from  $B$  band maximum.

Although SN 1986G was a rapidly-declining SN Ia, there is no reason for it to deviate from a Chandrasekhar mass explosion. SN 1986G may be classified as the extreme end of the normal population of SNe Ia, rather than part of the sub-luminous population. It is even more peculiar in properties than SN 2004eo. However, like SN 2004eo its low luminosity can be interpreted as the explosion having a strong deflagration phase, which unbinds the expansion of the star, reducing the density and therefore the effectiveness of the successive supersonic burning phase. This led to the production of a large fraction of IMEs (Mazzali et al., 2008).

These findings raise the possibility that only SNe Ia with very large decline rates deviate from a Chandrasekhar mass. The uncertainties in the analysis lie in the value of host galaxy extinction and the gaps in spectral coverage. However, SN 1986G is the only SN Ia with properties falling in the gap between normal and subluminous SNe Ia that also has a good time-series of spectra. Thus our analysis of SN 1986G explores an important region in parameter space in the overall SNe Ia picture.

## 6. Conclusions

The aims of this thesis were to improve our understanding of SNe Ia physics and explosions. This is motivated by the fact that, although SNe Ia are known to come from a thermonuclear explosion of a C+O Chandrasekhar mass WD, their exact explosion scenario is one of debate, and their full diversity is not fully understood.

To fully explore the optical diversity of SNe Ia a large sample study of  $B$  and  $V$  band SN LC was performed. The SNe Ia were separated by host galaxy type. By using a new method of calculating host galaxy extinction, it was found that ‘normal’ SNe Ia from passive galaxies are intrinsically fainter than those from S-F galaxies. Furthermore, a bimodal distribution in  $\Delta m_{15}(B)$  was discovered. This bimodality highlighted the lack of data for ‘transitional’ SN. This project also discovered that only SNe Ia with a blue intrinsic colour follow the WLR. In reality SNe Ia as a class are far more diverse objects. Interestingly it was found that SN from passive galaxies are more likely to be unusual and not standard candles, and transitional objects tend to favour passive galaxies. SNe Ia from S-F and passive galaxies were found to be distinct. In the  $V$ -band, there is a difference of  $0.4 \pm 0.13$  mag between the median (peak  $M_V$ ) values of the ‘normal’ SNIa population from passive and S-F galaxies. This is consistent with ( $\sim 15 \pm 10$ )% of ‘normal’ SNe Ia from S-F galaxies coming from an old stellar population. This project made it apparent that transitional SNe Ia hold the key to understanding the link between subluminal SNe Ia and normal SNe

Ia.

One way to understand this link could be through radiative transfer modelling. Therefore the second project in this thesis was to observe and model SN 2014J. This SN is a close and interesting object, and was used as a good test for modelling a normal SNe Ia. SN 2014J was the closest SNe Ia in recent history. It was located in the starburst galaxy M82. It was confirmed that SN 2014J suffered from a large amount of host galaxy extinction, which did not follow the normal  $R_V$ . The extinction parameters of SN 2014J are  $R_V=1.38$  and  $E(B - V)=1.2$ . SN 2014J was a normal SNe Ia, with a  $\Delta m_{15}(B)$   $1.05 \pm 0.12$ , when corrected for extinction. SN 2014J was found to have a stratified abundance. It has unburnt material at the highest velocities followed by IME and a NSE core, which consists of  $M(^{56}\text{Ni})=0.47\text{-}0.72 M_\odot$ .

With the knowledge that transitional SNe Ia are interesting and having the ability to model a SNe Ia, the data of SN 1986G was modeled. SN 1986G is a low luminosity transitional SNe Ia. It is also highly reddened. It is found that SN 1986G follows a normal Milky-Way extinction law with an  $R_V=3.1$ . A range of extinction and distance values were tested for this SN, and it was found that SN 1986G had an  $E(B - V)=0.65 \pm 0.05$  mag, and was located at a distance modulus of  $27.61 \pm 0.4$  mag. The full abundance tomography analysis was performed with a selection of density profiles. SN 1986G was found to be a low energy Chandrasekhar mass explosion, which had an energy 70% of the standard W7 model. The final masses of the main elements in the ejecta were found to be,  $\text{O}=0.33 M_\odot$ ,  $\text{IME}=0.69 M_\odot$ , stable  $\text{NSE}=0.21 M_\odot$ ,  $^{56}\text{Ni}=0.14 M_\odot$ . An upper limit of the carbon mass is set at  $\text{C}=0.02 M_\odot$ . SN 1986G can be thought of as a low luminosity extension of the main population of SN Ia, with a large deflagration phase that produced more IMEs than a standard SN Ia.

Overall, it can be concluded that SNe Ia from passive galaxies are less likely to be ‘normal’, and understanding more about transitional SNe Ia will hold the key to

determining if sub-luminous SNe Ia are a separate population. It may be the case that only at very large decline rates does the mass of SNe Ia deviate from the Chandrasekhar mass.

## 6.1 Futurework

In terms of SN 2014J a full abundance tomography analysis could be performed using the HST spectra. I could also examine the nebular spectra of SN 2014J in more detail, including measuring the FWHM of the Fe emission lines to see if it matches the previous predictions. The photometry of SN 2014J could be improved, by using more standard stars. To do this a function should be made to correct for the difference in exposure times for the opening and closing of the shutter. This function could then be re-applied to the the images and ‘standard’ photometry could be performed. A study into the diffuse interstellar bands in the FRODOSpec spectra could also be carried out.

The importance of selection effects in the sample used in chapter 2 should be examined. Specifically, is there any ways to make the sample less bias. Furthermore, the effects of using spectra which have host galaxy contamination to calcaate host galaxy extinction needs to be quantified. For example, are there significant amounts of spectra in the sample with host galaxy contanination, and is this significant for caulctaing host galaxy extinction?

More recently work has been carried out on two SNe Ia (SN 2011iv and SN 2007on) both of which exploded in NGC 1404 (Gall et al., in prep). These SN are a very good test case to examine the intrinsic differences between SN, as they are both at the same distance. Furthermore, these SN are both transitional have very fast LCs but appear intrinsically hot. It might be that these SNe hold the key to understanding the diversity at the faint end of the SNe Ia population. Preliminary results form Gall

et al., has shown that the difference in distance derived to these SN is 15% (Mpc), when using modern luminosity vs colour and luminosity vs decline rate relation. This is very interesting as it highlights the problems with improving the use of SNe Ia as distance indicators. Interestingly, SN 2011iv sits above the standard WLR (even if sbv or stretch is used instead of  $\Delta m_{15B}$ ).

Future work which will be carried out in line with this research is a detailed study into transitional SNe Ia. A full modelling analysis of SN 2011iv and SN 2007on should be performed. Both of these SN are fast declining. Furthermore, SN 2011iv has early HST spectra, so information can be inferred about the metallicity of the progenitor system. Preliminary results from modelling SN 2011iv show that it is a low energy Chandrasekhar mass explosion. The abundance stratification analysis found that there was  $^{56}\text{Ni}$  locate further out in the ejecta. The high central density (due to the low energy explosion) and the location of  $^{56}\text{Ni}$  in ejecta cause the light curve to be bright but fast. These results are also inline with modern 1D delayed detonation models (Höfllich private communication).

Preliminary results form modelling SN 2007on show that a standard 1D model cannot work. The outer layer of SN 2007on can be modelled with a normal W7 density profile, but the inner layers show a possible two component system, as found in the double peak nebular lines.

A full analysis into SN 2011iv and SN 2007on will demonstrate the diversity of SNe Ia, and show the importance of transitional SNe Ia. The fact that both exploded in the same galaxy shows that the standard LC fitting method may not always be reliable. If one wants to improve the accuracy of SNe Ia as cosmological distance indicators the reason for their diversity must be understood in more detail.

# Appendix

Table 6.1: The SNe used in the luminosity distribution study. The values have been corrected for MW extinction but not host galaxy extinction.

name	$m_B$	$\Delta m_{15}B$	$m_V$	$\Delta m_{15}V$	Dist (Mpc)	host type	$E(B-V)_{host}$	$(B - V)_{Bmax}$
SN1998de	$17.385 \pm 0.021$	$1.93 \pm 0.11$	$16.728 \pm 0.009$	$1.17 \pm 0.03$	$66.3 \pm 4.6$	S-F		$0.60 \pm 0.03$
SN1998dh	$14.116 \pm 0.004$	$0.77 \pm 0.01$	$14.084 \pm 0.005$	$0.33 \pm 0.01$	$37.5 \pm 2.6$	S-F	$0.00 \pm 0.004$	$-0.0 \pm 0.01$
SN1998dm	$14.738 \pm 0.017$	$0.90 \pm 0.03$	$14.431 \pm 0.006$	$0.55 \pm 0.01$	$26.2 \pm 1.8$	S-F	$0.36 \pm 0.005$	$0.24 \pm 0.05$
SN1998ef	$14.925 \pm 0.006$	$1.12 \pm 0.02$	$14.936 \pm 0.009$	$0.62 \pm 0.02$	$71.4 \pm 5.0$	S-F	$0.0 \pm 0.004$	$-0.0 \pm 0.01$
SN1998es	$13.818 \pm 0.021$	$0.92 \pm 0.03$	$13.767 \pm 0.009$	$0.54 \pm 0.01$	$42.0 \pm 2.9$	passive	$0.14 \pm 0.005$	$0.03 \pm 0.03$
SN1999aa	$14.749 \pm 0.009$	$0.88 \pm 0.04$	$14.807 \pm 0.017$	$0.43 \pm 0.08$	$62.7 \pm 4.4$	S-F	$0.0 \pm 0.006$	$-0.0 \pm 0.01$
SN1999ac	$14.224 \pm 0.006$	$0.90 \pm 0.01$	$14.109 \pm 0.005$	$0.58 \pm 0.01$	$46.7 \pm 3.3$	S-F		$0.05 \pm 0.01$
SN1999cl	$14.935 \pm 0.008$	$1.15 \pm 0.02$	$13.786 \pm 0.012$	$0.65 \pm 0.03$	$14.0 \pm 1.0$	S-F		$1.14 \pm 0.02$
SN1999cp	$13.903 \pm 0.006$	$1.10 \pm 0.02$	$13.923 \pm 0.005$	$0.71 \pm 0.01$	$44.1 \pm 3.1$	S-F	$0.09 \pm 0.007$	$-0.0 \pm 0.01$
SN1999da	$16.630 \pm 0.018$	$1.77 \pm 0.05$	$16.055 \pm 0.007$	$1.15 \pm 0.04$	$57.6 \pm 4.0$	passive	$0.0 \pm 0.017$	$0.44 \pm 0.02$
SN1999dk	$14.857 \pm 0.021$	$1.08 \pm 0.05$	$14.784 \pm 0.007$	$0.67 \pm 0.02$	$59.6 \pm 4.2$	S-F		$0.05 \pm 0.07$
SN1999dq	$14.419 \pm 0.005$	$0.96 \pm 0.01$	$14.339 \pm 0.004$	$0.57 \pm 0.00$	$57.0 \pm 4.0$	S-F	$0.11 \pm 0.006$	$0.08 \pm 0.01$
SN1999ej	$15.415 \pm 0.007$	$1.31 \pm 0.04$	$15.433 \pm 0.006$	$0.77 \pm 0.03$	$55.3 \pm 3.9$	S-F	$0.00 \pm 0.005$	$-0.0 \pm 0.01$
SN1999gp	$15.992 \pm 0.018$	$0.89 \pm 0.07$	$15.955 \pm 0.006$	$0.52 \pm 0.02$	$107. \pm 7.5$	S-F	$0.0 \pm 0.005$	$0.00 \pm 0.08$
SN2000cn	$16.610 \pm 0.013$	$1.55 \pm 0.04$	$16.480 \pm 0.010$	$0.95 \pm 0.02$	$102. \pm 7.2$	S-F	$0.0 \pm 0.006$	$0.08 \pm 0.02$

SN2000cu	$15.966 \pm 0.024$	$1.47 \pm 0.06$	$15.972 \pm 0.013$	$0.76 \pm 0.06$	$88.9 \pm 6.2$	S-F		$-0.0 \pm 0.02$
SN2000cw	$16.744 \pm 0.117$	$1.24 \pm 0.18$	$16.756 \pm 0.039$	$0.61 \pm 0.06$	$122. \pm 8.5$	S-F		$-0.0 \pm 0.03$
SN2000cx	$13.313 \pm 0.004$	$0.69 \pm 0.01$	$13.261 \pm 0.007$	$0.40 \pm 0.01$	$32.1 \pm 2.2$	S-F	$0.0 \pm 0.009$	$0.04 \pm 0.03$
SN2000dk	$15.448 \pm 0.012$	$1.17 \pm 0.05$	$15.427 \pm 0.008$	$0.75 \pm 0.02$	$70.2 \pm 4.9$	passive	$0.0 \pm 0.005$	$-0.0 \pm 0.03$
SN2000dm	$14.962 \pm 0.014$	$1.67 \pm 0.03$	$15.062 \pm 0.008$	$0.85 \pm 0.02$	$68.5 \pm 4.8$	S-F	$0.0 \pm 0.003$	$-0.0 \pm 0.01$
SN2000dn	$16.633 \pm 0.029$	$1.11 \pm 0.07$	$16.674 \pm 0.027$	$0.64 \pm 0.06$	$130. \pm 9.2$	S-F	$0.00 \pm 0.008$	$-0.0 \pm 0.05$
SN2000dr	$16.190 \pm 0.017$	$1.31 \pm 0.12$	$15.959 \pm 0.008$	$0.82 \pm 0.03$	$75.5 \pm 5.3$	S-F		$0.12 \pm 0.02$
SN2000fa	$15.904 \pm 0.017$	$1.01 \pm 0.03$	$15.867 \pm 0.011$	$0.57 \pm 0.02$	$88.7 \pm 6.2$	S-F	$0.06 \pm 0.004$	$0.06 \pm 0.02$
SN2001ay	$16.733 \pm 0.013$	$0.69 \pm 0.06$	$16.720 \pm 0.010$	$0.57 \pm 0.03$	$132. \pm 9.3$	S-F	$0.10 \pm 0.004$	$0.15 \pm 0.03$
SN2001bf	$14.787 \pm 0.009$	$0.74 \pm 0.02$	$14.795 \pm 0.005$	$0.42 \pm 0.02$	$70.3 \pm 4.9$	S-F	$0.03 \pm 0.008$	$-0.0 \pm 0.01$
SN2001br	$16.291 \pm 0.015$	$1.43 \pm 0.07$	$16.190 \pm 0.011$	$0.70 \pm 0.07$	$90.3 \pm 6.4$	S-F	$0.07 \pm 0.004$	$0.10 \pm 0.03$
SN2001cj	$15.846 \pm 0.009$	$0.92 \pm 0.04$	$15.963 \pm 0.010$	$0.53 \pm 0.03$	$107. \pm 7.5$	S-F		$-0.1 \pm 0.02$
SN2001ck	$16.769 \pm 0.020$	$1.11 \pm 0.08$	$16.788 \pm 0.015$	$0.65 \pm 0.06$	$150. \pm 10.5$	S-F		$-0.0 \pm 0.06$
SN2001cp	$15.705 \pm 0.011$	$0.88 \pm 0.03$	$15.732 \pm 0.008$	$0.55 \pm 0.02$	$100. \pm 7.0$	S-F	$0.05 \pm 0.005$	$-0.0 \pm 0.05$
SN2001da	$15.531 \pm 0.007$	$1.15 \pm 0.03$	$15.354 \pm 0.004$	$0.59 \pm 0.02$	$69.6 \pm 4.9$	S-F	$0.25 \pm 0.005$	$0.15 \pm 0.01$
SN2001dl	$16.880 \pm 0.017$	$0.94 \pm 0.06$	$16.594 \pm 0.010$	$0.60 \pm 0.02$	$87.0 \pm 6.1$	S-F		$0.28 \pm 0.04$
SN2001eh	$16.684 \pm 0.007$	$0.68 \pm 0.05$	$16.718 \pm 0.005$	$0.36 \pm 0.02$	$149. \pm 10.5$	S-F	$0.0 \pm 0.006$	$-0.0 \pm 0.02$

SN2001E	$16.830 \pm 0.025$	$1.32 \pm 0.12$	$16.302 \pm 0.015$	$0.73 \pm 0.06$	$87.5 \pm 6.1$	S-F		$0.51 \pm 0.06$
SN2001en	$15.123 \pm 0.007$	$1.07 \pm 0.02$	$15.080 \pm 0.007$	$0.67 \pm 0.02$	$63.9 \pm 4.5$	S-F		$0.01 \pm 0.01$
SN2001ep	$15.057 \pm 0.005$	$0.86 \pm 0.02$	$15.047 \pm 0.004$	$0.36 \pm 0.01$	$53.1 \pm 3.8$	S-F	$0.0 \pm 0.005$	$-0.0 \pm 0.01$
SN2001fh	$14.317 \pm 0.029$	$0.91 \pm 0.05$	$14.428 \pm 0.018$	$0.52 \pm 0.04$	$56.1 \pm 4.0$	S-F	$0.0 \pm 0.004$	$-0.1 \pm 0.03$
SN2002bo	$14.067 \pm 0.007$	$1.04 \pm 0.01$	$13.612 \pm 0.004$	$0.62 \pm 0.01$	$22.6 \pm 1.6$	S-F	$0.48 \pm 0.006$	$0.42 \pm 0.01$
SN2002cd	$15.782 \pm 0.013$	$0.86 \pm 0.05$	$15.116 \pm 0.007$	$0.54 \pm 0.02$	$46.4 \pm 3.3$	S-F	$0.56 \pm 0.007$	$0.63 \pm 0.03$
SN2002cf	$16.648 \pm 0.026$	$1.83 \pm 0.08$	$16.312 \pm 0.032$	$0.85 \pm 0.04$	$72.1 \pm 5.1$	passive		$0.20 \pm 0.03$
SN2002cs	$15.342 \pm 0.006$	$0.50 \pm 0.03$	$15.365 \pm 0.005$	$0.24 \pm 0.02$	$69.9 \pm 4.9$	passive	$0.0 \pm 0.011$	$-0.0 \pm 0.01$
SN2002cu	$16.225 \pm 0.006$	$1.28 \pm 0.03$	$16.151 \pm 0.005$	$0.76 \pm 0.01$	$101. \pm 7.1$	passive	$0.0 \pm 0.007$	$0.04 \pm 0.01$
SN2002de	$16.705 \pm 0.009$	$1.00 \pm 0.04$	$16.641 \pm 0.006$	$0.56 \pm 0.03$	$122. \pm 8.6$	S-F	$0.03 \pm 0.006$	$0.06 \pm 0.01$
SN2002dj	$13.954 \pm 0.010$	$1.00 \pm 0.02$	$13.864 \pm 0.007$	$0.59 \pm 0.01$	$38.4 \pm 2.7$	passive	$0.13 \pm 0.004$	$0.04 \pm 0.02$
SN2002dl	$16.002 \pm 0.007$	$1.38 \pm 0.03$	$15.761 \pm 0.007$	$0.93 \pm 0.02$	$67.8 \pm 4.7$	S-F	$0.0 \pm 0.008$	$0.21 \pm 0.01$
SN2002dp	$14.521 \pm 0.005$	$0.81 \pm 0.02$	$14.514 \pm 0.003$	$0.53 \pm 0.01$	$48.0 \pm 3.4$	S-F	$0.04 \pm 0.006$	$-0.0 \pm 0.01$
SN2002eb	$15.994 \pm 0.005$	$1.00 \pm 0.02$	$16.055 \pm 0.006$	$0.63 \pm 0.01$	$113. \pm 7.9$	S-F		$-0.0 \pm 0.01$
SN2002ef	$16.732 \pm 0.009$	$0.94 \pm 0.10$	$16.415 \pm 0.007$	$0.51 \pm 0.07$	$97.3 \pm 6.8$	S-F	$0.33 \pm 0.004$	$0.31 \pm 0.02$
SN2002el	$16.143 \pm 0.016$	$1.31 \pm 0.03$	$16.209 \pm 0.012$	$0.75 \pm 0.03$	$119. \pm 8.4$	S-F		$0.02 \pm 0.02$
SN2002er	$14.179 \pm 0.006$	$1.35 \pm 0.02$	$14.028 \pm 0.005$	$0.80 \pm 0.01$	$42.4 \pm 3.0$	S-F	$0.09 \pm 0.004$	$0.07 \pm 0.01$

SN2002fk	13.418± 0.004	0.70± 0.01	13.492±0.004	0.42±0.01	28.3±2.0	S-F	0.0±0.010	-0.1±0.01
SN2002ha	14.690± 0.004	1.38± 0.02	14.751±0.006	0.88±0.02	61.1±4.3	S-F	0.0±0.005	-0.1±0.01
SN2002he	16.461± 0.012	0.90± 0.03	16.389±0.012	0.65±0.02	103.±7.2	passive	0.0±0.005	0.03±0.03
SN2003cg	15.851± 0.010	1.02± 0.09	14.620±0.007	0.66±0.03	19.9±1.4	S-F	1.25±0.003	1.20±0.01
SN2003fa	16.659± 0.007	0.83± 0.01	16.703±0.009	0.54±0.01	171.±12.0	S-F	0.0±0.006	-0.0±0.02
SN2003gn	17.393± 0.019	1.20± 0.04	17.361±0.012	0.68±0.03	140.±9.9	S-F	0.14±0.008	0.02±0.03
SN2003gt	15.081± 0.005	0.89± 0.02	15.023±0.005	0.53±0.01	67.9±4.8	S-F		0.02±0.01
SN2003he	16.259± 0.007	0.91± 0.04	16.233±0.005	0.49±0.03	103.±7.2	S-F		-0.0±0.01
SN2003W	15.937± 0.005	1.09± 0.03	15.759±0.013	0.63±0.03	87.6±6.1	S-F		0.12±0.01
SN2003Y	17.802± 0.020	1.67± 0.07	16.962±0.010	1.07±0.03	73.0±5.1	passive	0.08±0.017	0.71±0.04
SN2004as	16.977± 0.012	1.23± 0.08	16.900±0.016	0.64±0.04	134.±9.4	S-F	0.08±0.005	0.03±0.02
SN2004at	15.708± 0.013	1.08± 0.03	15.824±0.007	0.65±0.02	99.5±7.0	S-F	0.0±0.004	-0.1±0.01
SN2004br	15.497± 0.005	0.76± 0.04	15.518±0.009	0.54±0.03	93.9±6.6	passive		-0.0±0.02
SN2004bv	14.022± 0.011	0.66± 0.03	13.902±0.008	0.43±0.01	47.4±3.3	S-F		0.09±0.03
SN2004bw	15.850± 0.010	1.23± 0.03	15.905±0.280	0.72±0.08	96.6±6.8	S-F		-0.0±0.02
SN2004dt	15.415± 0.005	0.85± 0.01	15.342±0.006	0.49±0.01	78.5±5.5	S-F		0.01±0.01
SN2004ef	16.899± 0.009	1.33± 0.06	16.791±0.011	0.71±0.02	126.±8.9	S-F	0.09±0.004	0.06±0.01

SN2004eo	$15.135 \pm 0.008$	$1.23 \pm 0.03$	$15.095 \pm 0.005$	$0.67 \pm 0.02$	$68.1 \pm 4.8$	S-F	$0.0 \pm 0.004$	$-0.0 \pm 0.01$
SN2004fz	$14.923 \pm 0.007$	$1.27 \pm 0.02$	$14.987 \pm 0.006$	$0.70 \pm 0.01$	$69.3 \pm 4.9$	S-F	$0.0 \pm 0.005$	$-0.1 \pm 0.01$
SN2005bc	$16.311 \pm 0.048$	$1.18 \pm 0.09$	$15.903 \pm 0.028$	$0.70 \pm 0.04$	$58.3 \pm 4.1$	S-F	$0.51 \pm 0.005$	$0.48 \pm 0.05$
SN2005cc	$16.690 \pm 0.016$	$2.19 \pm 0.10$	$16.262 \pm 0.011$	$0.86 \pm 0.05$	$38.9 \pm 2.7$	S-F		$0.41 \pm 0.02$
SN2005cf	$13.524 \pm 0.004$	$0.82 \pm 0.01$	$13.388 \pm 0.004$	$0.52 \pm 0.00$	$30.9 \pm 2.2$	S-F	$0.01 \pm 0.008$	$0.09 \pm 0.01$
SN2005de	$15.517 \pm 0.006$	$1.02 \pm 0.01$	$15.400 \pm 0.005$	$0.60 \pm 0.01$	$69.0 \pm 4.9$	S-F		$0.09 \pm 0.01$
SN2005dm	$18.424 \pm 0.045$	$1.71 \pm 0.18$	$17.228 \pm 0.01$	$1.32 \pm 0.03$	$67.0 \pm 4.7$	S-F		$1.13 \pm 0.06$
SN2005el	$14.983 \pm 0.005$	$0.98 \pm 0.03$	$15.041 \pm 0.005$	$0.63 \pm 0.02$	$60.4 \pm 4.2$	S-F	$0.0 \pm 0.003$	$-0.0 \pm 0.01$
SN2005eq	$16.263 \pm 0.007$	$0.81 \pm 0.03$	$16.242 \pm 0.008$	$0.51 \pm 0.02$	$116. \pm 8.1$	S-F	$0.12 \pm 0.008$	$0.01 \pm 0.01$
SN2005na	$15.999 \pm 0.013$	$1.29 \pm 0.06$	$15.97 \pm 0.01$	$0.52 \pm 0.03$	$108. \pm 7.6$	S-F	$0.0 \pm 0.005$	$-0.0 \pm 0.02$
SN2006cp	$15.905 \pm 0.017$	$1.14 \pm 0.07$	$15.845 \pm 0.017$	$0.58 \pm 0.03$	$99.3 \pm 7.0$	S-F	$0.11 \pm 0.005$	$0.05 \pm 0.02$
SN2006dm	$16.036 \pm 0.015$	$1.44 \pm 0.06$	$16.038 \pm 0.013$	$0.84 \pm 0.02$	$89.3 \pm 6.3$	S-F		$-0.0 \pm 0.03$
SN2006ef	$15.564 \pm 0.013$	$1.21 \pm 0.04$	$15.543 \pm 0.008$	$0.67 \pm 0.03$	$71.3 \pm 5.0$	passive		$0.00 \pm 0.01$
SN2006em	$18.357 \pm 0.01$	$1.43 \pm 0.05$	$17.388 \pm 0.01$	$1.07 \pm 0.03$	$77.5 \pm 5.4$	passive		$0.90 \pm 0.04$
SN2006en	$16.843 \pm 0.029$	$1.16 \pm 0.07$	$16.820 \pm 0.01$	$1.0 \pm 0.03$	$130. \pm 9.1$	S-F		$0.10 \pm 0.05$
SN2006eu	$17.445 \pm 0.039$	$1.25 \pm 0.17$	$16.954 \pm 0.024$	$0.65 \pm 0.05$	$100. \pm 7.0$	passive		$0.49 \pm 0.07$
SN2006gr	$17.007 \pm 0.028$	$0.85 \pm 0.05$	$16.896 \pm 0.016$	$0.55 \pm 0.02$	$141. \pm 9.9$	S-F	$0.06 \pm 0.005$	$0.14 \pm 0.05$

SN2006le	$14.888 \pm 0.016$	$0.94 \pm 0.03$	$14.955 \pm 0.009$	$0.60 \pm 0.01$	$72.4 \pm 5.1$	S-F	$0.0 \pm 0.004$	$-0.0 \pm 0.02$
SN2006lf	$14.262 \pm 0.047$	$1.15 \pm 0.15$	$14.200 \pm 0.019$	$0.81 \pm 0.03$	$54.2 \pm 3.8$	S-F	$0.01 \pm 0.003$	$0.00 \pm 0.03$
SN2007af	$13.191 \pm 0.006$	$1.11 \pm 0.02$	$13.135 \pm 0.005$	$0.68 \pm 0.02$	$27.6 \pm 1.9$	S-F	$0.10 \pm 0.004$	$0.01 \pm 0.01$
SN2007au	$16.596 \pm 0.024$	$1.70 \pm 0.07$	$16.408 \pm 0.01$	$0.82 \pm 0.03$	$86.1 \pm 6.0$	passive	$0.0 \pm 0.006$	$0.13 \pm 0.04$
SN2007bc	$15.846 \pm 0.014$	$1.31 \pm 0.04$	$15.914 \pm 0.009$	$0.68 \pm 0.02$	$92.3 \pm 6.5$	S-F	$0.0 \pm 0.007$	$-0.0 \pm 0.01$
SN2007co	$16.512 \pm 0.008$	$1.04 \pm 0.04$	$16.488 \pm 0.006$	$0.56 \pm 0.02$	$116. \pm 8.2$	passive	$0.10 \pm 0.005$	$0.00 \pm 0.02$
SN2007qe	$16.048 \pm 0.014$	$1.05 \pm 0.04$	$16.002 \pm 0.010$	$0.56 \pm 0.01$	$81.1 \pm 5.7$	passive	$0.02 \pm 0.004$	$0.06 \pm 0.02$
SN2008ar	$16.300 \pm 0.015$	$1.02 \pm 0.07$	$16.321 \pm 0.020$	$0.53 \pm 0.03$	$115. \pm 8.1$	S-F	$0.10 \pm 0.008$	$-0.0 \pm 0.04$
SN2008ec	$15.597 \pm 0.007$	$1.29 \pm 0.03$	$15.509 \pm 0.005$	$0.59 \pm 0.01$	$67.0 \pm 4.7$	S-F		$-0.0 \pm 0.02$
SN2002cr	$14.276 \pm 0.005$	$1.03 \pm 0.02$	$14.205 \pm 0.005$	$0.66 \pm 0.01$	$44.1 \pm 3.1$	S-F	$0.02 \pm 0.008$	$0.04 \pm 0.01$
SN2007ci	$15.903 \pm 0.020$	$1.78 \pm 0.04$	$15.900 \pm 0.018$	$0.91 \pm 0.04$	$81.9 \pm 5.7$	passive	$0.0 \pm 0.005$	$-0.0 \pm 0.06$
SN2007le	$13.871 \pm 0.031$	$1.06 \pm 0.07$	$13.583 \pm 0.024$	$0.62 \pm 0.04$	$28.1 \pm 2.0$	S-F	$0.22 \pm 0.005$	$0.23 \pm 0.02$
SN1999by	$13.567 \pm 0.005$	$1.84 \pm 0.01$	$13.098 \pm 0.004$	$1.18 \pm 0.00$	$12.2 \pm 0.86$	S-F	$0.0 \pm 0.017$	$0.38 \pm 0.01$
SN1997bp	$13.904 \pm 0.006$	$1.17 \pm 0.02$	$13.732 \pm 0.005$	$0.70 \pm 0.01$	$36.5 \pm 2.6$	S-F		$0.10 \pm 0.01$
SN1997dg	$16.856 \pm 0.017$	$1.31 \pm 0.12$	$16.845 \pm 0.016$	$0.57 \pm 0.04$	$137. \pm 9.7$	S-F		$0.00 \pm 0.02$
SN1997do	$14.367 \pm 0.191$	$0.85 \pm 0.17$	$14.34 \pm 0.028$	$0.00 \pm 0.03$	$44.3 \pm 3.1$	S-F	$0.0 \pm 0.005$	$-0.0 \pm 0.01$
SN1997E	$15.117 \pm 0.008$	$1.51 \pm 0.03$	$15.090 \pm 0.006$	$0.87 \pm 0.01$	$58.3 \pm 4.1$	passive	$0.00 \pm 0.005$	$0.00 \pm 0.01$

SN1998ab	$16.297 \pm 0.053$	$1.60 \pm 0.08$	$16.28 \pm 0.006$	$2.97 \pm 0.00$	$118. \pm 8.3$	S-F	$0.15 \pm 0.006$	$0.15 \pm 0.02$
SN1998V	$15.125 \pm 0.013$	$1.86 \pm 0.02$	$15.123 \pm 0.007$	$0.81 \pm 0.03$	$78.7 \pm 5.5$	S-F	$0.03 \pm 0.003$	$0.02 \pm 0.01$
SN1994ae	$13.109 \pm 0.144$	$0.85 \pm 0.11$	$12.992 \pm 0.143$	$0.63 \pm 0.09$	$23.3 \pm 1.6$	S-F	$0.16 \pm 0.004$	$0.07 \pm 0.03$
SN1994S	$14.785 \pm 0.123$	$0.98 \pm 0.10$	$14.798 \pm 0.038$	$0.66 \pm 0.08$	$70.0 \pm 4.9$	S-F	$0.07 \pm 0.004$	$-0.0 \pm 0.05$
SN1995ac	$17.162 \pm 0.021$	$0.57 \pm 0.06$	$17.163 \pm 0.018$	$0.46 \pm 0.04$	$204. \pm 14.3$	S-F	$0.0 \pm 0.008$	$-0.0 \pm 0.05$
SN1995ak	$16.047 \pm 0.01$	$1.73 \pm 0.05$	$15.957 \pm 0.054$	$0.95 \pm 0.08$	$90.4 \pm 6.3$	S-F		$0.01 \pm 0.07$
SN1995al	$13.328 \pm 0.040$	$0.79 \pm 0.12$	$13.215 \pm 0.024$	$0.65 \pm 0.06$	$26.5 \pm 1.9$	S-F	$0.11 \pm 0.004$	$0.09 \pm 0.05$
SN1995bd	$15.494 \pm 0.016$	$0.86 \pm 0.02$	$15.133 \pm 0.012$	$0.69 \pm 0.02$	$58.8 \pm 5.4$	S-F	$0.41 \pm 0.008$	$0.37 \pm 0.03$
SN1995D	$13.245 \pm 0.025$	$0.99 \pm 0.09$	$13.269 \pm 0.021$	$0.62 \pm 0.05$	$30.9 \pm 2.2$	S-F	$0.04 \pm 0.006$	$-0.0 \pm 0.05$
SN1995E	$16.724 \pm 0.034$	$1.09 \pm 0.14$	$16.023 \pm 0.027$	$0.62 \pm 0.09$	$50.9 \pm 3.6$	S-F	$0.79 \pm 0.003$	$0.69 \pm 0.06$
SN1996bo	$15.897 \pm 0.012$	$1.19 \pm 0.04$	$15.556 \pm 0.007$	$0.69 \pm 0.01$	$68.7 \pm 4.8$	S-F	$0.29 \pm 0.004$	$0.29 \pm 0.02$
SN1996X	$13.028 \pm 0.023$	$1.28 \pm 0.06$	$13.027 \pm 0.014$	$0.69 \pm 0.04$	$26.1 \pm 1.8$	passive	$0.00 \pm 0.003$	$-0.0 \pm 0.05$
SN1986G	$12.073 \pm 0.010$	$1.65 \pm 0.02$	$11.155 \pm 0.010$	$0.98 \pm 0.01$	$4.28 \pm 0.31$	passive		$0.78 \pm 0.04$
SN1990N	$12.683 \pm 0.049$	$1.03 \pm 0.08$	$12.657 \pm 0.062$	$0.62 \pm 0.09$	$13.9 \pm 1.0$	S-F		$0.02 \pm 0.02$
SN1991bg	$14.628 \pm 0.01$	$1.93 \pm 0.05$	$13.844 \pm 0.040$	$1.40 \pm 0.06$	$14.0 \pm 1.0$	passive	$0.08 \pm 0.014$	$0.70 \pm 0.10$
SN1991T	$11.619 \pm 0.111$	$0.88 \pm 0.11$	$11.453 \pm 0.160$	$0.58 \pm 0.08$	$13.5 \pm 0.9$	S-F	$0.17 \pm 0.007$	$0.15 \pm 0.02$
SN1998aq	$12.313 \pm 0.241$	$1.01 \pm 0.23$	$12.423 \pm 0.004$	$0.65 \pm 0.00$	$21.8 \pm 1.5$	S-F	$0.0 \pm 0.005$	$-0.1 \pm 0.03$

SN1999ee	$14.855 \pm 0.005$	$0.90 \pm 0.01$	$14.568 \pm 0.362$	$0.62 \pm 0.08$	$48.8 \pm 3.4$	S-F	$0.29 \pm 0.008$	$0.24 \pm 0.02$
SN2000E	$12.984 \pm 0.009$	$0.89 \pm 0.01$	$12.782 \pm 0.006$	$0.65 \pm 0.01$	$24.3 \pm 1.7$	S-F		$0.01 \pm 0.00$
SN2001bt	$15.251 \pm 0.010$	$1.27 \pm 0.03$	$15.056 \pm 0.006$	$0.71 \pm 0.01$	$64.7 \pm 4.5$	S-F		$0.15 \pm 0.04$
SN2001cz	$15.074 \pm 0.008$	$0.92 \pm 0.03$	$14.951 \pm 0.005$	$0.64 \pm 0.01$	$59.5 \pm 4.2$	S-F		$0.12 \pm 0.01$
SN2001el	$12.748 \pm 0.006$	$1.15 \pm 0.02$	$12.688 \pm 0.003$	$0.62 \pm 0.00$	$14.7 \pm 1.0$	S-F		$0.04 \pm 0.01$
SN2003du	$13.507 \pm 0.011$	$0.92 \pm 0.01$	$13.583 \pm 0.117$	$0.59 \pm 0.11$	$33.2 \pm 2.3$	S-F	$0.0 \pm 0.005$	$-0.2 \pm 0.04$
SN2001fe	$14.991 \pm 0.207$	$1.39 \pm 0.28$	$14.911 \pm 0.118$	$0.71 \pm 0.05$	$60.6 \pm 4.2$	S-F	$0.04 \pm 0.007$	$0.05 \pm 0.04$
SN2002hu	$16.616 \pm 0.045$	$0.89 \pm 0.19$	$16.720 \pm 0.011$	$0.56 \pm 0.03$	$120. \pm 8.4$	S-F	$0.12 \pm 0.012$	$-0.0 \pm 0.03$
SN2003kf	$13.490 \pm 0.112$	$0.93 \pm 0.15$	$13.405 \pm 0.021$	$0.69 \pm 0.12$	$30.6 \pm 2.1$	S-F	$0.16 \pm 0.004$	$0.10 \pm 0.05$
SN2005hc	$17.381 \pm 0.316$	$0.89 \pm 0.21$	$17.453 \pm 0.158$	$0.62 \pm 0.03$	$184. \pm 13.0$	passive	$0.0 \pm 0.005$	$-0.1 \pm 0.05$
SN2005hk	$15.822 \pm 0.374$	$1.57 \pm 0.46$	$15.701 \pm 0.067$	$0.82 \pm 0.18$	$52.3 \pm 3.7$	S-F		$0.02 \pm 0.02$
SN2005iq	$16.803 \pm 0.392$	$1.09 \pm 0.02$	$16.921 \pm 0.030$	$0.73 \pm 0.09$	$138. \pm 9.7$	S-F	$0.0 \pm 0.003$	$-0.1 \pm 0.10$
SN2005kc	$15.660 \pm 0.01$	$1.45 \pm 0.05$	$15.375 \pm 0.144$	$0.87 \pm 0.09$	$62.8 \pm 4.4$	S-F	$0.33 \pm 0.004$	$0.28 \pm 0.05$
SN2005lz	$17.659 \pm 0.01$	$0.57 \pm 0.05$	$17.571 \pm 0.01$	$0.34 \pm 0.03$	$178. \pm 12.5$	S-F	$0.19 \pm 0.008$	$0.05 \pm 0.04$
SN2005mc	$17.262 \pm 0.055$	$1.78 \pm 0.22$	$17.066 \pm 0.019$	$1.08 \pm 0.06$	$106. \pm 7.4$	S-F	$0.11 \pm 0.006$	$0.17 \pm 0.04$
SN2005ms	$16.191 \pm 0.01$	$0.66 \pm 0.05$	$16.210 \pm 0.300$	$0.57 \pm 0.42$	$106. \pm 7.5$	S-F		$0.01 \pm 0.03$
SN2005mz	$16.541 \pm 0.179$	$1.75 \pm 0.11$	$16.216 \pm 0.229$	$1.27 \pm 0.01$	$70.9 \pm 5.0$	S-F	$0.0 \pm 0.013$	$0.32 \pm 0.09$

SN2006S	$16.833 \pm 0.203$	$0.87 \pm 0.21$	$16.806 \pm 0.156$	$0.59 \pm 0.04$	$138. \pm 9.7$	S-F	$0.16 \pm 0.006$	$0.08 \pm 0.04$
SN2006ac	$16.242 \pm 0.467$	$1.20 \pm 0.21$	$16.096 \pm 0.210$	$0.71 \pm 0.02$	$102. \pm 7.2$	S-F	$0.20 \pm 0.005$	$0.13 \pm 0.05$
SN2006ax	$15.026 \pm 0.01$	$1.05 \pm 0.05$	$15.099 \pm 0.069$	$0.65 \pm 0.04$	$76.3 \pm 5.3$	S-F	$0.02 \pm 0.005$	$-0.0 \pm 0.03$
SN2006az	$16.484 \pm 0.01$	$1.25 \pm 0.05$	$16.570 \pm 0.075$	$0.72 \pm 0.04$	$132. \pm 9.3$	S-F	$0.0 \pm 0.006$	$-0.1 \pm 0.05$
SN2006bt	$16.973 \pm 0.185$	$0.99 \pm 0.01$	$16.853 \pm 0.019$	$0.58 \pm 0.03$	$140. \pm 9.9$	S-F	$0.09 \pm 0.005$	$0.15 \pm 0.04$
SN2006cc	$17.868 \pm 0.01$	$0.91 \pm 0.05$	$17.506 \pm 0.119$	$0.69 \pm 0.04$	$140. \pm 9.8$	S-F	$0.12 \pm 0.010$	$0.39 \pm 0.05$
SN2006cm	$18.049 \pm 0.01$	$1.04 \pm 0.05$	$17.055 \pm 0.041$	$0.72 \pm 0.01$	$69.6 \pm 4.9$	S-F	$0.95 \pm 0.008$	$1.00 \pm$
SN2006qo	$16.859 \pm 0.01$	$1.03 \pm 0.05$	$16.687 \pm 0.105$	$0.59 \pm 0.07$	$126. \pm 8.9$	S-F		$0.20 \pm$
SN2006sr	$16.206 \pm 0.239$	$1.74 \pm 0.26$	$16.20 \pm 0.017$	$0.0 \pm 0.03$	$97.5 \pm 6.8$	S-F	$0.04 \pm 0.004$	$0.04 \pm 0.05$
SN2007F	$15.890 \pm 0.01$	$0.88 \pm 0.05$	$15.920 \pm 0.099$	$0.61 \pm 0.09$	$103. \pm 7.2$	S-F	$0.00 \pm 0.004$	$-0.0 \pm$
SN2007S	$15.843 \pm 0.01$	$0.86 \pm 0.05$	$15.436 \pm 0.102$	$0.63 \pm 0.06$	$62.5 \pm 4.4$	S-F	$0.43 \pm 0.007$	$0.38 \pm$
SN2007ca	$15.988 \pm 0.01$	$0.86 \pm 0.05$	$15.700 \pm 0.060$	$0.71 \pm 0.09$	$65.1 \pm 4.6$	S-F	$0.37 \pm 0.005$	$0.31 \pm$
SN2008bf	$15.767 \pm 0.01$	$1.00 \pm 0.05$	$15.729 \pm 0.094$	$0.63 \pm 0.05$	$106. \pm 7.4$	passive	$0.06 \pm 0.006$	$0.08 \pm 0.05$
SN2007kk	$16.948 \pm 0.016$	$0.79 \pm 0.12$	$16.874 \pm 0.012$	$0.70 \pm 0.04$	$165. \pm 11.6$	S-F	$0.0 \pm 0.004$	$0.00 \pm$
SN2008Z	$16.505 \pm 0.020$	$0.62 \pm 0.02$	$16.202 \pm 0.011$	$0.65 \pm 0.01$	$90.7 \pm 6.4$	passive	$0.03 \pm 0.008$	$0.12 \pm 0.03$
SN2008cm	$15.688 \pm 0.044$	$1.35 \pm 0.22$	$15.778 \pm 0.209$	$0.86 \pm 0.08$	$45.2 \pm 3.2$	S-F		$-0.1 \pm$
SN2008gb	$17.098 \pm 0.024$	$1.23 \pm 0.17$	$16.961 \pm 0.027$	$0.63 \pm 0.06$	$149. \pm 10.5$	S-F		$0.07 \pm 0.11$

SN2008gl	$16.826 \pm 0.014$	$0.97 \pm 0.06$	$16.737 \pm 0.012$	$0.81 \pm 0.02$	$136. \pm 9.6$	passive	$0.0 \pm 0.003$	$-0.0 \pm$
SN2008hm	$15.636 \pm 0.150$	$1.20 \pm 0.18$	$15.609 \pm 0.016$	$0.61 \pm 0.03$	$79.7 \pm 5.6$	S-F		$-0.0 \pm 0.10$
SN2008hv	$14.878 \pm 0.226$	$1.18 \pm 0.10$	$14.796 \pm 0.090$	$0.78 \pm 0.07$	$55.8 \pm 3.9$	passive	$0.11 \pm 0.003$	$0.07 \pm$
SN2009Y	$14.672 \pm 0.054$	$1.79 \pm 0.15$	$14.723 \pm 0.008$	$0.92 \pm 0.01$	$41.1 \pm 2.9$	S-F	$0.0 \pm 0.006$	$-0.0 \pm$
SN2009al	$16.288 \pm 0.021$	$0.99 \pm 0.04$	$16.105 \pm 0.015$	$0.53 \pm 0.02$	$97.6 \pm 6.8$	passive		$0.08 \pm 0.05$
SN2009an	$14.487 \pm 0.133$	$1.40 \pm 0.25$	$14.418 \pm 0.007$	$0.79 \pm 0.01$	$43.8 \pm 3.1$	S-F		$0.04 \pm 0.05$
SN2009dc	$15.079 \pm 0.074$	$0.67 \pm 0.13$	$15.041 \pm 0.006$	$0.32 \pm 0.01$	$96.1 \pm 6.7$	passive		$-0.0 \pm 0.04$
SN2009ig	$13.466 \pm 0.284$	$0.89 \pm 0.10$	$13.364 \pm 0.01$	$0.59 \pm 0.03$	$34.7 \pm 2.4$	S-F		$0.09 \pm$
SN2009jr	$16.364 \pm 0.017$	$0.91 \pm 0.08$	$15.859 \pm 0.011$	$0.67 \pm 0.03$	$71.7 \pm 5.0$	S-F		$0.46 \pm$
SN2009kq	$14.521 \pm 0.019$	$1.12 \pm 0.20$	$14.480 \pm 0.006$	$0.67 \pm 0.01$	$51.8 \pm 3.6$	passive		$0.01 \pm 0.02$
SN2009na	$15.818 \pm 0.014$	$0.98 \pm 0.03$	$15.773 \pm 0.077$	$0.75 \pm 0.08$	$92.8 \pm 6.5$	S-F		$0.01 \pm 0.05$
SN2010Y	$14.997 \pm 0.052$	$1.78 \pm 0.14$	$14.969 \pm 0.008$	$0.92 \pm 0.01$	$49.6 \pm 3.5$	passive		$-0.0 \pm$
SN2010ag	$16.704 \pm 0.031$	$0.99 \pm 0.16$	$16.551 \pm 0.012$	$0.67 \pm 0.05$	$145. \pm 10.2$	S-F		$0.07 \pm 0.09$
SN2010ai	$16.088 \pm 0.217$	$1.31 \pm 0.34$	$16.019 \pm 0.009$	$0.77 \pm 0.01$	$83.5 \pm 5.9$	passive		$-0.0 \pm$

Table 6.2: The photometry of SN 2014J. The errors on the magnitudes do not include the error on the standard star.

MJD	$g$	$r$	$i$
56684.1	11.67 $\pm$ 0.001	10.44 $\pm$ 0.001	10.26 $\pm$ 0.001
56685.1	11.59 $\pm$ 0.001	10.37 $\pm$ 0.001	10.21 $\pm$ 0.001
56685.9	11.52 $\pm$ 0.004	10.34 $\pm$ 0.002	10.21 $\pm$ 0.002
56688.9	11.43 $\pm$ 0.001	10.20 $\pm$ 0.001	10.20 $\pm$ 0.001
56689.9	11.41 $\pm$ 0.001	10.19 $\pm$ 0.001	10.25 $\pm$ 0.001
56692.0	11.43 $\pm$ 0.001	10.16 $\pm$ 0.001	-
56692.9	11.43 $\pm$ 0.001	10.18 $\pm$ 0.001	10.34 $\pm$ 0.001
56693.8	11.46 $\pm$ 0.001	10.19 $\pm$ 0.001	10.38 $\pm$ 0.001
56694.9	11.47 $\pm$ 0.001	10.25 $\pm$ 0.001	10.42 $\pm$ 0.001
56695.8	11.50 $\pm$ 0.001	10.27 $\pm$ 0.001	10.46 $\pm$ 0.001
56696.8	11.52 $\pm$ 0.001	10.31 $\pm$ 0.001	-
56697.9	11.56 $\pm$ 0.001	10.40 $\pm$ 0.001	10.61 $\pm$ 0.001
56698.8	11.60 $\pm$ 0.001	-	-
56699.8	11.65 $\pm$ 0.001	10.47 $\pm$ 0.001	
56700.8	11.69 $\pm$ 0.001	10.57 $\pm$ 0.001	10.74 $\pm$ 0.001
56701.8	11.75 $\pm$ 0.002	-	-
56709.8	12.29 $\pm$ 0.002	10.91 $\pm$ 0.001	10.89 $\pm$ 0.002
56710.8	12.31 $\pm$ 0.002	-	-
56712.1	12.46 $\pm$ 0.003	10.94 $\pm$ 0.003	10.84 $\pm$ 0.002
56712.8	12.50 $\pm$ 0.002	-	-
56713.8	12.55 $\pm$ 0.002	10.91 $\pm$ 0.001	10.72 $\pm$ 0.001
56714.8	12.67 $\pm$ 0.002	10.93 $\pm$ 0.001	10.76 $\pm$ 0.001
56715.8	12.72 $\pm$ 0.004	11.01 $\pm$ 0.002	10.72 $\pm$ 0.002
56716.8	12.81 $\pm$ 0.004	-	10.68 $\pm$ 0.002
56717.8	12.90 $\pm$ 0.004	-	-
56718.8	12.95 $\pm$ 0.004	11.08 $\pm$ 0.001	10.69 $\pm$ 0.002
56719.8	13.03 $\pm$ 0.012	11.12 $\pm$ 0.002	10.72 $\pm$ 0.002
56720.8	13.10 $\pm$ 0.005	11.13 $\pm$ 0.002	10.66 $\pm$ 0.002

# References

- Altavilla, G., Stehle, M., Ruiz-Lapuente, P., et al. 2007, *A&A*, 475, 585
- Amanullah, R., Goobar, A., Johansson, J., et al. 2014, *ApJ*, 788, L21
- Anderson, J. P., James, P. A., Förster, F., et al. 2015, *MNRAS*, 448, 732
- Anupama, G. C., Sahu, D. K., Deng, J., et al. 2005, *ApJ*, 631, L125
- Ashall, C., Mazzali, P., Bersier, D., et al. 2014, *MNRAS*, 445, 4427
- Ashall, C., Mazzali, P., Sasdelli, M., & Prentice, S. J. 2016, *MNRAS*, 460, 3529
- Ashall, C., Mazzali, P. A., Pian, E., & James, P. A. 2016, *MNRAS*,
- Arnett, W. D., Truran, J. W., & Woosley, S. E. 1971, *ApJ*, 165, 87
- Arnett, W. D. 1982, *ApJ*, 253, 785
- Axelrod T. S., 1980, PhD thesis, California Univ., Santa Cruz.
- Baade, W., & Minkowski, R. 1954, *ApJ*, 119, 215
- Barnsley, R. M., Smith, R. J., & Steele, I. A. 2012, *A.N.*, 333, 101
- Benetti, S., Cappellaro, E., Mazzali, P. A., et al. 2005, *ApJ*, 623, 1011
- Bessell, M. S. 1990, *PASP*, 102, 1181

- Bikmaev, I. F., Chugai, N. N., Sunyaev, R. A., et al. 2015, *Astronomy Letters*, 41, 785
- Bland, J., Taylor, K., & Atherton, P. D. 1987, *MNRAS*, 228, 595
- Blinnikov, S. I., & Khokhlov, A. M. 1986, *Soviet Astronomy Letters*, 12, 131
- Blinnikov, S. I., & Khokhlov, A. M. 1987, *Soviet Astronomy Letters*, 13, 364
- Brandt, T. D., Tojeiro, R., Aubourg, É., et al. 2010, *AJ*, 140, 804
- Brown, P. J., Smitka, M. T., Wang, L., et al. 2015, *ApJ*, 805, 74
- Burns, C. R., Stritzinger, M., Phillips, M. M., et al. 2014, *ApJ*, 789, 32
- Cappellaro, E., Mazzali, P. A., Benetti, S., et al. 1997, *A&A*, 328, 203
- Cardelli, J. A., Clayton, G. C., & Mathis, J. S. 1989, *ApJ*, 345, 245
- Carroll B. W., Ostlie D. A., 2007, Pearson Education, Inc.
- Childress, M., Aldering, G., Antilogus, P., et al. 2013, *ApJ*, 770, 108
- Chotard, N., Gangler, E., Aldering, G., et al. 2011, *A&A*, 529, L4
- Colgate, S. A., & McKee, C. 1969, *ApJ*, 157, 623
- Conley, A., Sullivan, M., Hsiao, E. Y., et al. 2008, *ApJ*, 681, 482-498
- Cristiani, S., Cappellaro, E., Turatto, M., et al. 1992, *A&A*, 259, 63
- Deng, J., Kawabata, K. S., Ohshima, Y., et al. 2004, *ApJ*, 605, L37
- Dilday, B., Howell, D. A., Cenko, S. B., et al. 2012, *Science*, 337, 942
- Disney, M. J., & Wallace, P. T. 1982, *QJRAS*, 23, 485
- Dong, S., Katz, B., Kushnir, D., & Prieto, J. L. 2015, *MNRAS*, 454, L61

- Elias-Rosa, N., Benetti, S., Cappellaro, E., et al. 2006, *MNRAS*, 369, 1880
- Ferrarese, L., Mould, J. R., Stetson, P. B., et al. 2007, *ApJ*, 654, 186
- Filippenko, A. V. 1997, *ARA&A*, 35, 309
- Fink, M., Hillebrandt, W., & Röpke, F. K. 2007, *A&A*, 476, 1133
- Fisher, A., Branch, D., Hatano, K., & Baron, E. 1999, *MNRAS*, 304, 67
- Fitzpatrick, E. L., & Massa, D. 1999, *ApJ*, 525, 1011
- Folatelli, G., Phillips, M. M., Burns, C. R., et al. 2010, *AJ*, 139, 120
- Foley, R. J., Kromer, M., Howie Marion, G., et al. 2012, *ApJ*, 753, L5
- Foley, R. J., Fox, O. D., McCully, C., et al. 2014, *MNRAS*, 443, 2887
- Foley, R. J., Pan, Y.-C., Brown, P., et al. 2016, *MNRAS*, 461, 1308
- Fossey, S. J., Cooke, B., Pollack, G., Wilde, M., & Wright, T. 2014, *CBET*, 3792, 1
- Frogel, J. A., Gregory, B., Kawara, K., et al. 1987, *ApJ*, 315, L129
- Fukugita, M., Shimasaku, K., & Ichikawa, T. 1995, *PASP*, 107, 945
- Ganeshalingam, M., Li, W., Filippenko, A. V., et al. 2010, *ApJS*, 190, 418
- Ganeshalingam, M., Li, W., & Filippenko, A. V. 2011, *MNRAS*, 416, 2607
- Goobar, A., Johansson, J., Amanullah, R., et al. 2014, *ApJ*, 784, L12
- Graham, M. L., Valenti, S., Fulton, B. J., et al. 2015, *ApJ*, 801, 136
- Guy, J., Sullivan, M., Conley, A., et al. 2010, *A&A*, 523, A7
- Hachinger, S., Mazzali, P. A., & Benetti, S. 2006, *MNRAS*, 370, 299

- Hachinger, S., Mazzali, P. A., Taubenberger, S. 2009, MNRAS, 399, 1238
- Hachinger, S., Mazzali, P. A., Taubenberger, S., et al. 2012, MNRAS, 427, 2057
- Hamuy, M., Phillips, M. M., Maza, J., et al. 1995, AJ, 109, 1
- Hamuy, M., Phillips, M. M., Suntzeff, N. B., et al. 1996, AJ, 112, 2408
- Hamuy, M., Phillips, M. M., Suntzeff, N. B., et al. 2003, , 424, 651
- Hicken, M., Challis, P., Jha, S., et al. 2009, ApJ, 700, 331
- Hicken, M., Challis, P., Kirshner, R. P., et al. 2012, ApJS, 200, 12
- Hillebrandt, W., & Niemeyer, J. C. 2000, ARA&A, 38, 191
- Hoeflich, P., Khokhlov, A. M., & Wheeler, J. C. 1995, ApJ, 444, 831
- Höflich, P., Gerardy, C. L., Fesen, R. A., & Sakai, S. 2002, ApJ, 568, 791
- Høg, E., Fabricius, C., Makarov, V. V., et al. 2000, A&A, 355, L27
- Howell, D. A. 2001, ApJ, 554, L193
- Howell, D. A., Sullivan, M., Nugent, P. E., et al. 2006, , 443, 308
- Hsiao, E. Y., Conley, A., Howell, D. A., et al. 2007, ApJ, 663, 1187
- Hsiao, E. Y., Burns, C. R., Contreras, C., et al. 2015, A&A, 578, A9
- Hutton, S., Ferreras, I., Wu, K., et al. 2014, MNRAS, 440, 150
- Iben, I., Jr., & Tutukov, A. V. 1984, ApJS, 54, 335
- Iwamoto, K., Brachwitz, F., Nomoto, K., et al. 1999, ApJS, 125, 439
- Ivezic, Z. 2014, American Astronomical Society Meeting Abstracts #223, 223, 317.03

- Jack, D., Mittag, M., Schröder, K.-P., et al. 2015, MNRAS, 451, 4104
- Kasen D., 2016, P-Cygni Profile, <http://supernova.lbl.gov/dnkasen/>
- Kasen, D., Branch, D., Baron, E., & Jeffery, D. 2002, ApJ, 565, 380
- Katz, B., & Dong, S. 2012, arXiv:1211.4584
- Kasliwal, M. M., Kulkarni, S. R., Gal-Yam, A., et al. 2012, ApJ, 755, 161
- Kasliwal, M. 2015, Boutiques & Experiments, Caltech
- Kelly, P. L., Fox, O. D., Filippenko, A. V., et al. 2014, ApJ, 790, 3
- Kessler, R., Becker, A. C., Cinabro, D., et al. 2009, ApJS, 185, 32
- Krisciunas, K., Suntzeff, N. B., Candia, P., et al. 2003, AJ, 125, 166
- Krisciunas, K., Phillips, M. M., Suntzeff, N. B., et al. 2004, AJ, 127, 1664
- Krisciunas, K., Suntzeff, N. B., Phillips, M. M., et al. 2004, AJ, 128, 3034
- Kromer, M., Ohlmann, S. T., Pakmor, R., et al. 2015, MNRAS, 450, 3045
- Leaman, J., Li, W., Chornock, R., & Filippenko, A. V. 2011, MNRAS, 412, 1419
- Leloudas, G., Stritzinger, M. D., Sollerman, J., et al. 2009, A&A, 505, 265
- Lentz, E. J., Baron, E., Branch, D., Hauschildt, P. H. 2000, ApJ, 530, 966
- Li, W., Filippenko, A. V., Chornock, R., et al. 2003, PASP, 115, 453
- Li, W., Leaman, J., Chornock, R., et al. 2011, VizieR Online Data Catalog, 741,
- Lira, P., Suntzeff, N. B., Phillips, M. M., et al. 1998, AJ, 115, 234
- Livne, E., & Arnett, D. 1995, ApJ, 452, 62

- Lucy, L. B. 1999, *A&A*, 345, 211
- Maguire, K., Sullivan, M., Thomas, R. C., et al. 2011, *MNRAS*, 418, 747
- Maguire, K., Sullivan, M., Ellis, R. S., et al. 2012, *MNRAS*, 426, 2359
- Maguire, K., Sullivan, M., Pan, Y.-C., et al. 2014, *MNRAS*, 444, 3258
- Maguire, K., Taubenberger, S., Sullivan, M. 2016, *MNRAS*, 457, 3254
- Mandel, K. S., Foley, R. J., & Kirshner, R. P. 2014, *ApJ*, 797, 75
- Maoz, D., Sharon, K., & Gal-Yam, A. 2010, *ApJ*, 722, 1879
- Marion, G. H., Sand, D. J., Hsiao, E. Y., et al. 2015, *ApJ*, 798, 39
- Mazzali, P. A., & Lucy, L. B. 1993, *A&A*, 279, 447
- Mazzali, P. A., Lucy, L. B., Danziger, I. J., et al. 1993, *A&A*, 269, 423
- Mazzali, P. A., Danziger, I. J., & Turatto, M. 1995, *A&A*, 297, 509
- Mazzali, P. A., Cappellaro, E., Danziger, I. 1998, *ApJ*, 499, L49
- Mazzali, P. A. 2000, *A&A*, 363, 705
- Mazzali, P. A., Nomoto, K., Cappellaro, E., et al. 2001, *ApJ*, 547, 988
- Mazzali, P. A., Benetti, S., Altavilla, G., et al. 2005, *ApJ*, 623, L37
- Mazzali, P. A., Röpke, F. K., Benetti, S., & Hillebrandt, W. 2007, *Science*, 315, 825
- Mazzali, P. A., Foley, R. J., Deng, J., et al. 2007, *ApJ*, 661, 892
- Mazzali, P. A., Sauer, D. N. 2008, *MNRAS*, 386, 1897
- Mazzali, P. A., Maurer, I., Stritzinger, M., et al. 2011, *MNRAS*, 416, 881

- Mazzali, P. A., & Hachinger, S. 2012, MNRAS, 424, 2926
- Mazzali, P. A., Sullivan, M., Hachinger, S., et al. 2014, MNRAS, 439, 1959
- Mazzali, P. A., Sullivan, M., Filippenko, A. V., et al. 2015, MNRAS, 450, 2631
- Mihalas D., 1978, Stellar atmospheres 2nd edition
- Mould, J. R., Huchra, J. P., Freedman, W. L., et al. 2000, ApJ, 529, 786
- Maoz, D., Mannucci, F., & Nelemans, G. 2014, ARA&A, 52, 107
- Munari, U., Henden, A., Belligoli, R., et al. 2013, , 20, 30
- Muratov, A. L., & Gnedin, O. Y. 2010, ApJ, 718, 1266
- Nomoto, K. 1982, ApJ, 257, 780
- Nomoto, K., & Kondo, Y. 1991, ApJ, 367, L19
- Nomoto, K., Thielemann, F.-K., & Yokoi, K. 1984, ApJ, 286, 644
- Nomoto, K., Iwamoto, K., & Kishimoto, N. 1997, Science, 276, 1378
- Nugent, P., Phillips, M. 1995, ApJ, 455, L147
- Oke, J. B., & Sandage, A. 1968, ApJ, 154, 21
- Pan, Y.-C., Sullivan, M., Maguire, K., et al. 2015, MNRAS, 446, 354
- Pan, Y.-C., Foley, R. J., Kromer, M., et al. 2015, MNRAS, 452, 4307
- Pastorello, A., Mazzali, P. A., Pignata, G., et al. 2007, MNRAS, 377, 1531
- Pauldrach, A. W. A., Duschinger, M., Mazzali, P. A., et al. 1996, A&A, 312, 525
- Pereira, R., Thomas, R. C., Aldering, G., et al. 2013, A&A, 554, A27

- Perlmutter, S., Aldering, G., Goldhaber, G., et al. 1999, *ApJ*, 517, 565
- Phillips, M. M. 1993, *ApJ*, 413, L105
- Phillips, M. M., Phillips, A. C., Heathcote, S. R., et al. 1987, *PASP*, 99, 592
- Phillips, M. M., Lira, P., Suntzeff, N. B., et al. 1999, *AJ*, 118, 1766
- Porter, A. L., Leising, M. D., Milne, P., et al. 2015, American Astronomical Society Meeting Abstracts, 225, 450.04
- Rau, A., Kulkarni, S. R., Law, N. M., et al. 2009, *PASP*, 121, 1334
- Rest, A., Scolnic, D., Foley, R. J., et al. 2014, *ApJ*, 795, 44
- Richter, O.-G., & Huchtmeier, W. K. 1984, *A&A*, 132, 253
- Riess, A. G., Press, W. H., & Kirshner, R. P. 1996, *ApJ*, 473, 88
- Riess, A. G., Filippenko, A. V., Challis, P., et al. 1998, *AJ*, 116, 1009
- Riess, A. G., Kirshner, R. P., Schmidt, B. P., et al. 1999, *AJ*, 117, 707
- Riess, A. G., Li, W., Stetson, P. B., et al. 2005, *BAAS*, 37, 180.10
- Rigault, M., Copin, Y., Aldering, G., et al. 2013, *A&A*, 560, A66
- Röpke, F. K., Hillebrandt, W., Schmidt, W., et al. 2007, *ApJ*, 668, 1132
- Rosswog, S., Kasen, D., Guillochon, J., & Ramirez-Ruiz, E. 2009, *ApJ*, 705, L128
- Ruiter, A. J., Belczynski, K., & Fryer, C. 2009, *ApJ*, 699, 2026
- Ruiter, A. J., Belczynski, K., Benacquista, M. 2010, *ApJ*, 717, 1006
- Sahu, D. K., Tanaka, M., Anupama, G. C., et al. 2008, *ApJ*, 680, 580-592

- Sasdelli, M., Mazzali, P. A., Pian, E., et al. 2014, *MNRAS*, 445, 711
- Sasdelli, M., Ishida, E. E. O., Hillebrandt, W., et al. 2016, *MNRAS*, 460, 373
- Sauer, D. N., Mazzali, P. A., Blondin, S., et al. 2008, *MNRAS*, 391, 1605
- Schlafly, E. F., & Finkbeiner, D. P. 2011, *ApJ*, 737, 103
- Schmidt, W., Ciaraldi-Schoolmann, F., Niemeyer, J. C., Röpke, F. K., & Hillebrandt, W. 2010, *ApJ*, 710, 1683
- Shigeyama, T., Nomoto, K., Yamaoka, H., & Thielemann, F.-K. 1992, *ApJ*, 386, L13
- Silverman, J. M., Nugent, P. E., Gal-Yam, A., et al. 2013, *ApJS*, 207, 3
- Silverman, J. M., Vinkó, J., Marion, G. H., et al. 2015, *MNRAS*, 451, 1973
- Sim, S. A., Röpke, F. K., Hillebrandt, W., et al. 2010, *ApJ*, 714, L52
- Soria, R., Mould, J. R., Watson, A. M., et al. 1996, *ApJ*, 465, 79
- Stehle, M., Mazzali, P. A., Benetti, S., & Hillebrandt, W. 2005, *MNRAS*, 360, 1231
- Srivastav, S., Ninan, J. P., Kumar, B., et al. 2016, *MNRAS*, 457, 1000
- Stritzinger, M., & Leibundgut, B. 2005, *A&A*, 431, 423
- Sullivan, M., Le Borgne, D., Pritchett, C. J., et al. 2006, *ApJ*, 648, 868
- Sullivan, M., Conley, A., Howell, D. A., et al. 2010, *MNRAS*, 406, 782
- Tanaka, M., Mazzali, P. A., Maeda, K., & Nomoto, K. 2006, *ApJ*, 645, 470
- Taubenberger, S., Hachinger, S., Pignata, G., et al. 2008, *MNRAS*, 385, 75
- Telesco, C. M., Höflich, P., Li, D., et al. 2015, *ApJ*, 798, 93

- Tripp, R. 1998, *A&A*, 331, 815
- Tsvetkov, D. Y., Metlov, V. G., Shugarov, S. Y., Tarasova, T. N. 2014, *CAOSP*, 44, 67
- Tubbs, A. D. 1980, *ApJ*, 241, 969
- Turatto, M. 2003, *Supernovae and Gamma-Ray Bursters*, 598, 21
- Valentini, G., Di Carlo, E., Massi, F., et al. 2003, *ApJ*, 595, 779
- Vallely, P., Moreno-Raya, M. E., Baron, E., et al. 2016, *MNRAS*, 460, 1614
- Wang, X., Wang, L., Filippenko, A. V., Zhang, T., & Zhao, X. 2013, *Science*, 340, 170
- Woosley, S. E., & Weaver, T. A. 1986, *ARA&A*, 24, 205
- Woosley, S. E., Arnett, W. D., & Clayton, D. D. 1973, *ApJS*, 26, 231
- Woosley, S. E., Kasen, D., Blinnikov, S., & Sorokina, E. 2007, *ApJ*, 662, 487
- Woudt, P. A., Steeghs, D., Karovska, M., et al. 2009, *ApJ*, 706, 738
- Yamanaka, M., Kawabata, K. S., Kinugasa, K., et al. 2009, *ApJ*, 707, L118
- Yamanaka, M., Maeda, K., Kawabata, M., et al. 2014, *ApJ*, 782, L35
- Yasuda, N., & Fukugita, M. 2010, *AJ*, 139, 39
- Yoon, S.-C., & Langer, N. 2005, *A&A*, 435, 967
- Zheng, W., Shivvers, I., Filippenko, A. V., et al. 2014, *ApJ*, 783, L24
- De Vaucouleurs, G. 1980, *ApJ*, 240, L93